Naval Research Laboratory

Washington, DC 20375-5320

Experimental Observations at Very Low Grazing Angles of High Range Resolution Microwave Backscatter from the Sea

FRED L. POSNER

Radar Analysis Branch
Radar Division

December 31, 1998

19990413 052

DTIC QUALITY INSPECTED 2

REPORT DOCUMENTATION PAGE

Public reporting burden for this collection of information is estimated to average 1 hour per response, including the time for reviewing instructions, searching existing data sources, gathering and maintaining the data needed, and completing and reviewing the collection of information. Send comments regarding this burden estimate or any other aspect of this collection of information, including suggestions for reducing this burden, to Washington Headquarters Services, Directorate for Information Operations and Reports, 1215 Jefferson Davis Highway, Suite 1204, Arlington, VA 22202-4302, and to the Office of Management and Budget. Paperwork Reduction Project (0704-0188), Washington, DC 20503.

1. AGENCY USE ONLY (Leave Blank)	2. REPORT DATE December 31, 1998	3. REPORT TYPE AND DATES COVERED	
4. TITLE AND SUBTITLE Experimental Observations at Very Low Grazing Angles of High Range Resolution Microwave Backscatter from the Sea			**5. FUNDING NUMBERS** PE - 61153N
6. AUTHOR(S) Fred L. Posner			
7. PERFORMING ORGANIZATION NAME(S) AND ADDRESS(ES) Naval Research Laboratory Washington, DC 20375-5320			**8. PERFORMING ORGANIZATION REPORT NUMBER** NRL/MR/5310--98-8326
9. SPONSORING/MONITORING AGENCY NAME(S) AND ADDRESS(ES) Office of Naval Research 800 N. Quincy Street Arlington, VA 22217-5660			**10. SPONSORING/MONITORING AGENCY REPORT NUMBER**
11. SUPPLEMENTARY NOTES			
12a. DISTRIBUTION/AVAILABILITY STATEMENT Approved for public release; distribution unlimited.			**12b. DISTRIBUTION CODE** A

13. ABSTRACT (Maximum 200 words)

X-band (9.5-10.0 GHz) backscatter at near grazing incidence (0.2 degrees) from the sea off the coast of Kauai, Hawaii, was measured with a radar characterized by a high spatial resolution in range (0.3 meters) and a high temporal resolution (2000 Hz PRF). Extensive amounts (over 1200 seconds per measurement) of vertically and horizontally polarized sea clutter data were taken with upwind and crosswind transmit geometries. The clutter was statistically and phenomenologically analyzed over time scales varying from long (200 seconds), to intermediate (5 seconds), to short (50 milliseconds), and over range swaths varying from full (160 meters), to partial (30 meters), to a single range cell (0.3 meters). Each type of clutter exhibited the characteristic spiky behavior which has come to be expected from microwave sea backscatter observed at low grazing angles and high range resolutions, while showing, between themselves, marked transmit geometry and polarization dependent contrasts, with the horizontally polarized clutter, measured with an upwind transmit geometry, being especially notable for its frequently occurring, significant high frequency spectral content. The extent of the high frequency spectral content appears to increase with the overall magnitude of a spatially and temporally extended spiking event, and the distribution of radar cross sections appears to vary between extended spiking events of the same clutter type.

14. SUBJECT TERMS			15. NUMBER OF PAGES
Sea backscatter Sea clutter	Sea spikes Low grazing angle	High resolution Microwave	56
			16. PRICE CODE

17. SECURITY CLASSIFICATION OF REPORT	18. SECURITY CLASSIFICATION OF THIS PAGE	19. SECURITY CLASSIFICATION OF ABSTRACT	20. LIMITATION OF ABSTRACT
UNCLASSIFIED	UNCLASSIFIED	UNCLASSIFIED	UL

Contents

Experimental Observations at Very Low Grazing Angles of High Range Resolution Microwave Backscatter from the Sea

1 Introduction

The performance of high resolution radars in the detection and tracking of targets with low radar cross sections, such as submarine periscopes, may be seriously affected by the strong, targetlike returns from the sea, often referred to as sea spikes, that can occur at low grazing angles. The performance of lower resolution radars, such as those used in sea skimming missiles, in the detection and tracking of relatively low cross section ship targets, may be similarly affected by the spiky sea backscatter frequently encountered at low grazing angles. In both of these cases, the backscatter from the sea is the clutter whose presence can seriously interfere with the radar's primary objective with regard to the intended target. Thus, an understanding of sea clutter at low grazing angles and high resolutions plays a critical role in considerations of modern naval radar performance.

The objective of the analyses[1] documented in this report is to add to this understanding by studying characteristic, contrasting, and illustrative sea clutter taken from an extensive data base which contains multiple transmit geometries and polarizations. It will be seen that the richly complex behavior of sea clutter at low grazing angles and high range resolutions is strongly dependent upon transmit geometry and polarization, as well as upon the scale of observation, both spatially and temporally.

The plan of this report is as follows. In Section 2, there will be brief descriptions of the sea backscatter data collection and the radar system used for it. In Section 3, analyses of data over long time scales (on the order of 200 seconds) and over the full range swath (156 meters) will be presented. In Section 4, analyses of data over intermediate time scales (on the order of 5 seconds) and over partial range swaths (on the order of 30 meters) will be presented. In Section 5, analyses of data over intermediate time scales and over single range cells (0.3 meters) will be presented. In Section 6, analyses of data over short time scales (on the order of 50 milliseconds) and over single range cells will be presented. In Section 7, the results of these analyses will be discussed in relation to other recent research into high resolution, low grazing angle, sea backscatter. In Section 8, there will be a brief conclusion and summary. A highly abridged version of this report, presenting some of this material, has been published in the Proceedings of the 1998 IEEE Radar Conference. (See Posner [Posn 98a].) A somewhat less abridged version of this report, presenting a larger portion of this material, has been submitted to the IEEE Transactions on Geoscience and Remote Sensing. (See Posner [Posn 98b].)

Manuscript approved November 18, 1998.

Table 1: Radar Descriptors

Operating Frequency	X-band (9.5–10.0 GHz)
Peak Power	500 KW
Pulse Length	500 ns compressed to 2.5 ns
Range Resolution	0.3 m
Signal Processing	synchronous demodulation for I and Q channels with 8 bit analog-to-digital conversion at 500 MHz
Pulse Repetition Frequency	2000 Hz
Data Collection Extent	156 m range swath consisting of 512 individual range cells
Data Collection Mode	spotlight (searchlight) due to fixed antenna pointing
Antenna Beamwidths	2.4° in azimuth and 4.0° in elevation
Polarization	either vertical transmit, vertical receive (VV) or horizontal transmit, horizontal receive (HH)

2 Experimental Measurements

Between August and December of 1994, the Naval Research Laboratory (NRL), in conjunction with the Naval Air Warfare Center, China Lake (NAWC/CL), the Johns Hopkins University Applied Physics Laboratory (JHU/APL), and Texas Instruments (TI), carried out extensive sea clutter measurements from various sites in Kauai, Hawaii, as part of the Advanced Radar Periscope Detection and Discrimination (ARPDD) program, which was sponsored by the Office of Naval Research (ONR). It should be noted that these high PRF sea clutter measurements were incidental to the main concerns of the ARPDD program, and that the analyses of such data are essentially studies of opportunity.

The system used to gather the data was NRL's Advanced Profile Testbed Radar, an enhanced version of the APS-137 radar. The radar operated at X-band (9.5–10.0 GHz) with a peak transmitted power of 500 kilowatts. The transmitted pulse length of 500 nanoseconds, when compressed to 2.5 nanoseconds, yielded data with 0.3 meter range resolution. The data processing consisted of synchronous demodulation with 8 bit analog-to-digital conversion at 500 MHz for both I and Q channels. The pulse repetition frequency (PRF) for these clutter measurements was 2000 Hz. The data collection swath for this mode was 156 meters in extent, with the data from each pulse filling 512 adjacent, individual 0.3 meter range cells.

The high PRF data collected in this mode is referred to as spotlight or searchlight because the position of the antenna was fixed. The antenna beamwidth was 2.4 degrees in azimuth and 4.0 degrees in elevation. The polarization was vertical transmit, vertical receive (VV) or horizontal transmit, horizontal receive (HH). To go from one polarization to another required a feedhorn change, and as a result of this, individual data collection runs, which were typically between 1200 and 1500 seconds in duration, consist of data of only one polarization. An itemized description of the measurement radar appears in Table 1.

With the clutter data from this collection, it is not possible to compare the radar returns from the same sea spike event in the two different polarizations. With regard to the polarization dependence of high resolution, low grazing angle, sea backscatter, the best that

Table 2: Data Descriptors, Part 1

Data Tag	Start Time	Transmit/Receive Polarization	Radar Height	Radar Range	Grazing Angle
94110807	2200 GMT	vertical/vertical	23 m	5.74 km	0.23°
94110809	2355 GMT	vertical/vertical	23 m	6.48 km	0.20°
94110816	0413 GMT	horizontal/horizontal	23 m	6.11 km	0.22°
94110818	0507 GMT	horizontal/horizontal	23 m	6.30 km	0.21°

can be done with the available data, insofar as this report is concerned, is to examine sea spike events from the same day and the same transmit geometry, and trust, to some degree, that the physical phenomena that produce typical and characteristic backscatter for the VV data collection run are much the same as the physical phenomena that produce typical and characteristic backscatter for the HH data collection run.

There are three major descriptors of the measured backscatter data. The first of these data descriptors is grazing angle, which is determined by the radar height and the radar range. These clutter measurements were taken at the Lihue Airport site, where the antenna was 23 meters above mean sea level, and the center of the 156 meter range swath varied between 5.74 and 6.48 kilometers downrange. Thus, for these data runs, the grazing angle varied between of 0.23 and 0.20 degrees. At this point, one should note for future reference that the azimuthal beamwidth of 2.4 degrees leads to a footprint that varies between 240 meters wide, at a range of 5.74 kilometers, and 270 meters wide, at a range of 6.48 kilometers.

The second major descriptor of the measured backscatter data is transmit geometry, which is determined by the radar bearing and the wind direction. Two different transmit geometries, upwind (UP) and crosswind (CR), were available at the Lihue Airport site, which faces east into the prevailing trade winds. The average wind speed at this site is in excess of 6 meters per second, and sea states of 3 or higher would be expected here. In fact, on the day when the backscatter measurements presented in this report were made, 8 November 1994, the measured wind speeds were on the order of 9 meters per second and the measured significant wave heights (average height of the one-third highest waves) were on the order of 3 meters.

Finally, the third major descriptor of the measured data is polarization, which is either vertical transmit, vertical receive (VV) or horizontal transmit, horizontal receive (HH). Sea backscatter measurements, characterized by a specific grazing angle, transmit geometry, and polarization, were made in data collection runs that typically lasted over 1200 seconds, for which period of time the wind speed and the significant wave height would be determined. The above characterization of the measured sea backscatter data is summarized in Tables 2 and 3. In these tables, the 8 digit data tag consists of the year, the month, and the day when the measurement was made, followed by the number of the data collection run from which the specific examples of data were taken for subsequent analysis.

The vertically polarized, upwind transmit geometry (VV/UP) run (94110807) was taken between 12:00 noon and 12:26 PM local time. The vertically polarized, crosswind

Table 3: Data Descriptors, Part 2

Data Tag	Radar Bearing	Wind Direction	Transmit Geometry	Wind Speed	Significant Wave Height
94110807	086°	075°	upwind	9.0 m/s	2.9 m
94110809	158°	073°	crosswind	9.6 m/s	3.0 m
94110816	078°	—	upwind	—	—
94110818	037°	—	crosswind	—	—

transmit geometry (VV/CR) run (94110809), which required an adjustment of pointing angle for the antenna, was taken between 1:55 PM and 2:17 PM local time. The horizontally polarized, upwind transmit geometry (HH/UP) run (94110816), which required a feedhorn change and a pointing angle adjustment for the antenna, was taken between 6:13 PM and 6:36 PM local time. Finally, the horizontally polarized, crosswind transmit geometry (HH/CR) run (94110818), which required an adjustment of pointing angle for the antenna, was taken between 7:07 PM and 7:29 PM local time. Although all of these measurements were made the same day, the runs with the same polarization but different transmit geometries (VV/UP and VV/CR; HH/UP and HH/CR) were separated in time by only 1 or 2 hours, whereas the runs with the same transmit geometry but different polarizations (VV/UP and HH/UP; VV/CR and HH/CR) were separated in time by 5 or 6 hours.

The reader will note that neither the wind direction, nor the wind speed, nor the significant wave height, were measured for either of the HH data collection runs. The reason was that the APL instrumentation ship for environmental measurements had gone home after a very long and demanding day of being buffeted by nontrivial seas, leaving the NRL radar operators to decide, based on the winds at the radar site itself, rather than those actually out at sea, where best to point the radar antenna to achieve either an UP or CR transmit geometry. (See Kerr [Kerr 97].)

For the VV/UP run, the bearing of the radar was 86 degrees, while the wind direction (true) was 75 degrees, an alignment appropriate for an UP transmit geometry. For the HH/UP run, the bearing of the radar was 78 degrees, which is very close to that for the VV/UP run. If, during the HH/UP run, the unmeasured wind direction was also close to that during the VV/UP run, which occurred 6 hours earlier, then, once again, the alignment would be appropriate for an UP transmit geometry. In the next section, it will be seen that examples of clutter data taken from both the VV/UP and HH/UP runs, when analyzed, exhibit exactly the behavior that would be expected from data measured with an UP transmit geometry.

For the VV/CR run, after a clockwise rotation for the antenna of 72 degrees from what it had been during the VV/UP run, the bearing of the radar was 158 degrees. During the VV/CR run, the wind direction (true) was 73 degrees, almost identical to what had been measured during the VV/UP run 2 hours earlier. Thus, for the VV/CR run, the alignment was, apparently, appropriate for a CR transmit geometry. For the HH/CR run, after a counterclockwise rotation for the antenna of 41 degrees from what it had been during the HH/UP run, the bearing of the radar was 37 degrees. If, during the HH/CR run, the

unmeasured wind direction was also close to that during the HH/UP run, which occurred 1 hour earlier, then, however, the alignment was not, apparently, appropriate for a CR transmit geometry. In the next section, it will be seen, somewhat surprisingly, that it is the example of clutter data taken from the HH/CR run, which, when analyzed, exhibits exactly the behavior that would be expected from data measured with a CR transmit geometry, while, somewhat unexpectedly, it is the example of clutter data taken from the VV/CR run, which, when analyzed, exhibits behavior more appropriate to data measured with an UP rather than a CR transmit geometry. The explanation for this mystery is not immediately obvious.

During the VV/UP run, the measured wind speed was 9.0 meters per second and the measured significant wave height was 2.9 meters. During the VV/CR run, the measured wind speed was 9.6 meters per second and the measured significant wave height was 3.0 meters. While certainly not an exact measurement, it was frequently observed in Kauai that wind speeds and wave heights would be somewhat diminished late in the afternoon and early in the evening, compared to midday and early in the afternoon.

Those measurements of wind speed that are available can be used in conjunction with standard theoretical models for fully-developed deep water waves, which is a reasonable characterization of the seas off the windward coast of Kauai. These models predict a wave period of 6.5 seconds and a wavelength of 66 meters, for a wind speed of 9.0 meters per second, and a wave period of 7.0 seconds and a wavelength of 76 meters, for a wind speed of 9.6 meters per second. These models also predict, for a wind speed of 9.0 meters per second, a phase speed of 10 meters per second and a group speed of 5 meters per second, and for a wind speed of 9.6 meters per second, a phase speed of 11 meters per second and a group speed of 5.5 meters per second. In these models, the group speed for fully-developed deep water waves is half the phase speed. (See Mart [Mart 97].)

3   Long Time Scales and Full Range Swaths

In this section, we will consider examples of backscatter data whose extents in time are on the order of 200 seconds and whose extents in range are over the full range swath of 156 meters. The first four images, contained in the first two figures, present calibrated radar cross section (RCS), in deciBels above a square meter (dBsm), as a function of time, in seconds, along the horizontal axis, and of range, in meters, along the vertical axis. These are also known as range-time intensity (RTI) plots. A horizontal cut, at a fixed value of the range, gives the evolution over time of the clutter. A vertical cut, at a fixed value of the time, gives the variation over range of the clutter. Occasionally, at a specific time and over all ranges, electronic interference will produce a thin vertical line that is visibly present in the data, an example of which phenomenon appears just before the 80 second mark in the top image in Figure 1.

The clutter data presented in these four images have been temporally averaged by noncoherently integrating 200 pulses at a time. The use of noncoherent integration, which in this case effectively reduces, or spoils, the full temporal resolution from 2000 Hz down to 10 Hz, is a common technique for smoothing the grainy, speckled quality of radar images. (See Posner [Posn 93].) The resulting smoothness of these images is one of the reasons why

the effort was made to obtain lower temporal resolution data when there was high PRF data originally available. (The other reason will be discussed in the second half of this section.) Each of these four images consists of 2048 noncoherently integrated, effectively 10 Hz, pulses. The data from each of these pulses extends over 512 range cells.

Figure 1 consists of RTI plots of RCS for upwind transmit geometry (UP) sea clutter occurring over long time scales and full range swaths. Within Figure 1, the data in the top image is vertically polarized (VV) and the data in the bottom image is horizontally polarized (HH). Figure 2 consists of RTI plots of RCS for crosswind transmit geometry (CR) sea clutter occurring over long time scales and full range swaths. Within Figure 2, the data in the top image is VV and the data in the bottom image is HH. The dynamic range of the data as presented, covering 40 dB and extending from -35 dBsm to $+5$ dBsm, is the same for all four images.

The first and most obvious observation to make is that these computer-generated images of microwave reflectivity, with their pattern of alternating greater and lesser radar returns, look like waves rolling in from the sea. It appears physically reasonable to infer that it is the alternating crests and troughs of the incoming waves which give rise to the observed regularity in the radar returns. In addition, given the near grazing incidence of the measurements, there might very well be some shadowing effects contributing to the lowered reflectivity of certain regions in the images.

Examination of the clearly visible, regular patterns in these images for temporal frequencies, in the horizontal direction, and spatial frequencies, in the vertical direction, indicates wave periods on the order of 7 seconds and wavelengths on the order of 70 meters. These values are quite consistent with the purely theoretical predictions of wave periods and wavelengths for fully-developed deep water waves, based upon measured wind speeds, as discussed at the end of the previous section.

The VV/UP clutter, at the top of Figure 1, and the HH/UP clutter, at the bottom of Figure 1, at the largest scale, exhibit a conspicuously regular, wavelike pattern. One would expect this with an UP transmit geometry because the relatively wide cross-range footprint of the radar is aligned with the incoming waves, so that it alternately catches the more reflective crests and then the less reflective troughs associated with individual waves. On the other hand, the wide azimuthal beamwidth would tend to filter out those waves traveling perpendicular to the radar's line of sight, through the interfence of the returns from multiple independent scattering centers associated with the train of waves falling within the radar's footprint.

The speed of the basic, large-scale wave phenomena, simply determined from the observed slopes of individual streaks running from the tops to the bottoms of the RTI plots, which, for this purpose, were examined with expanded time scales, is on the order of 12 meters per second for both the VV/UP and the HH/UP clutter. It will be noted that this is roughly on the order of the predicted phase speeds for these sea conditions, as discussed in the previous section. Closer examination of the two different UP RTI plots in Figure 1 also reveals the presence of smaller-scale structure in the form of substreaks within the large-scale streaks. These substreaks, which only run from side to side of the larger streaks, have less steep slopes and hence, smaller speeds, speeds which are roughly on the order of the predicted group speeds for these sea conditions, also as discussed in the previous section. Much more detailed analysis of these smaller-scale wave phenomena will be presented in the
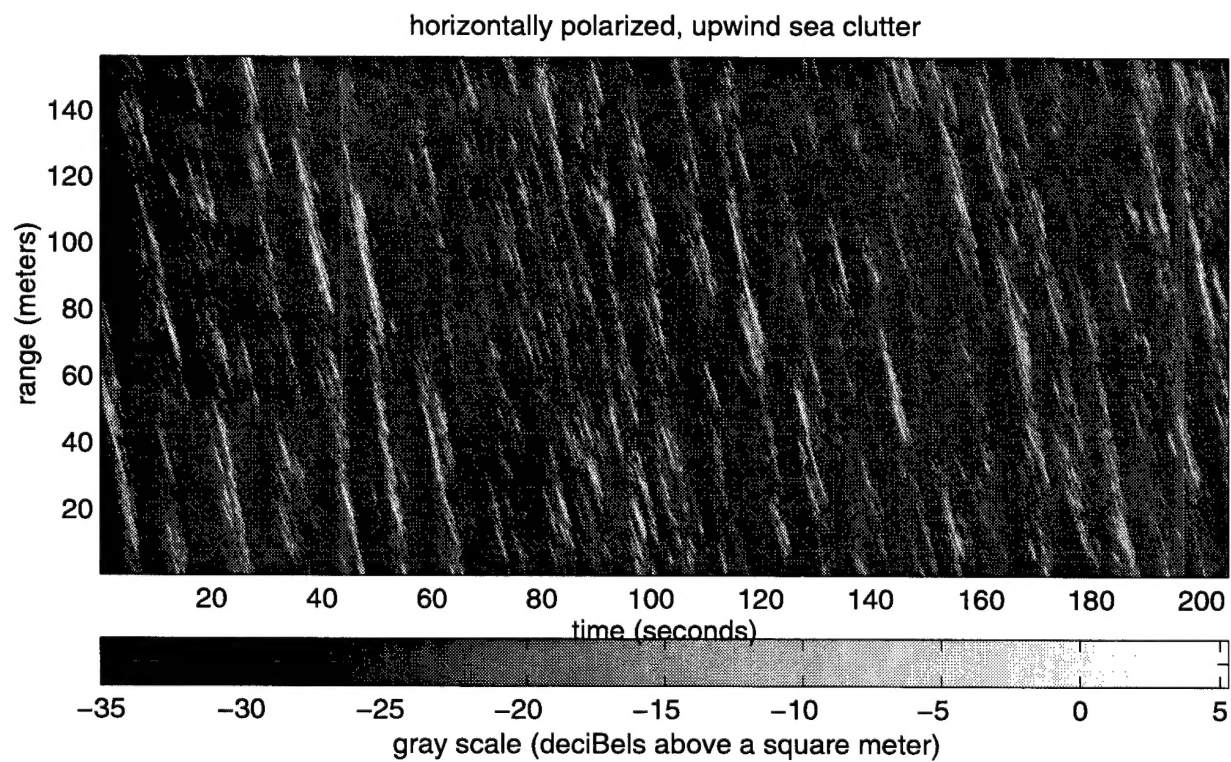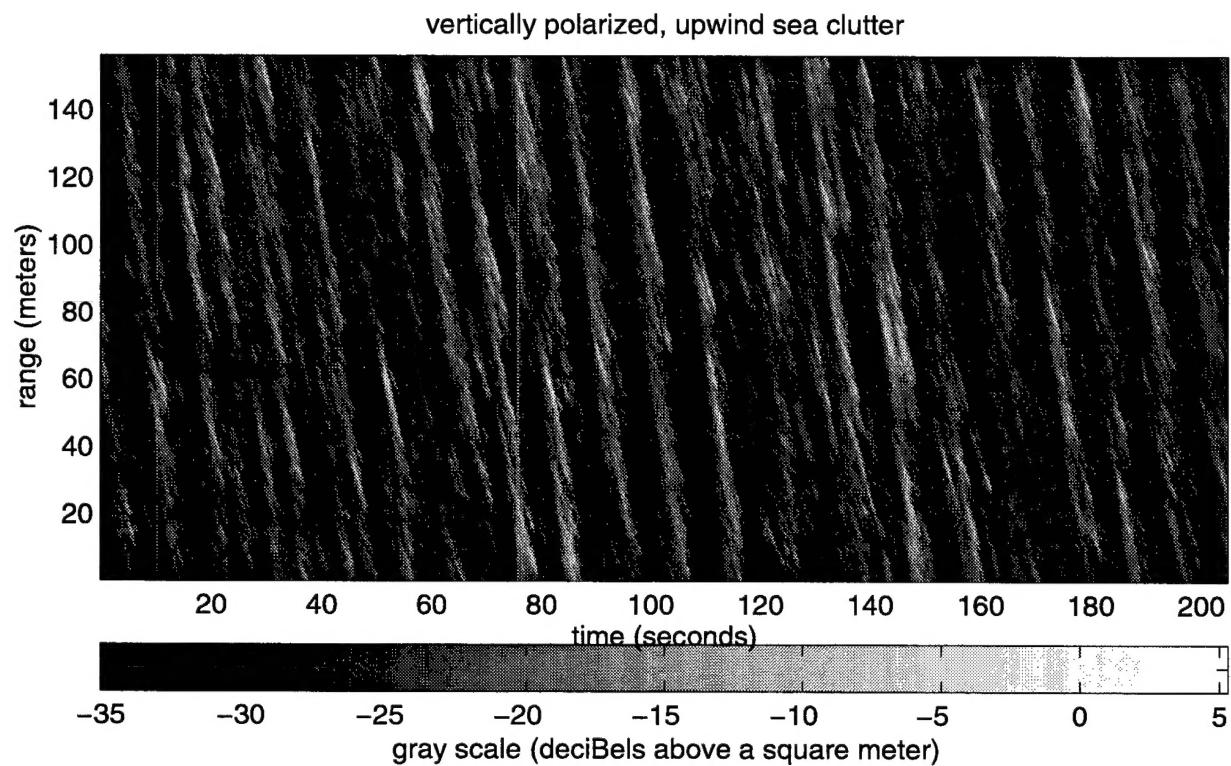
Figure 1: RTI plots of RCS, in dBsm, for VV (above) and HH (below), UP sea clutter, after noncoherent temporal averaging.
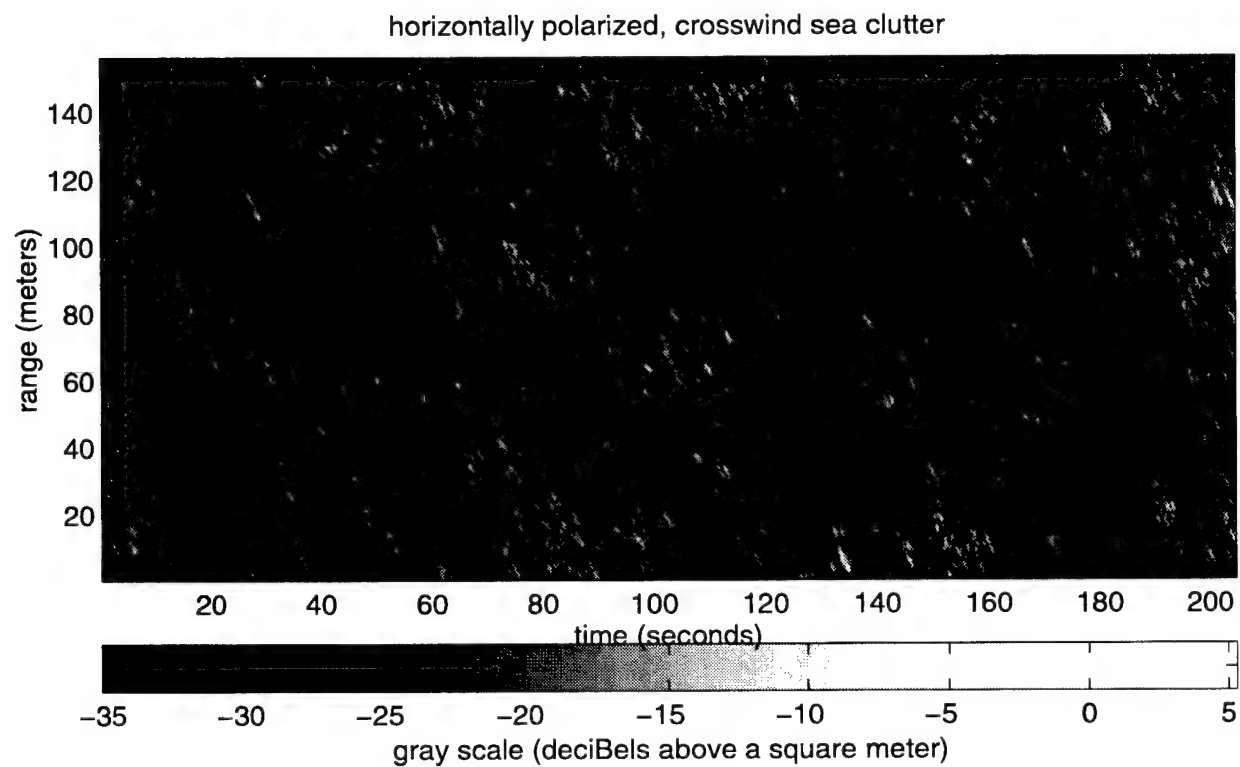
vertically polarized, crosswind sea clutter

gray scale (deciBels above a square meter)

horizontally polarized, crosswind sea clutter
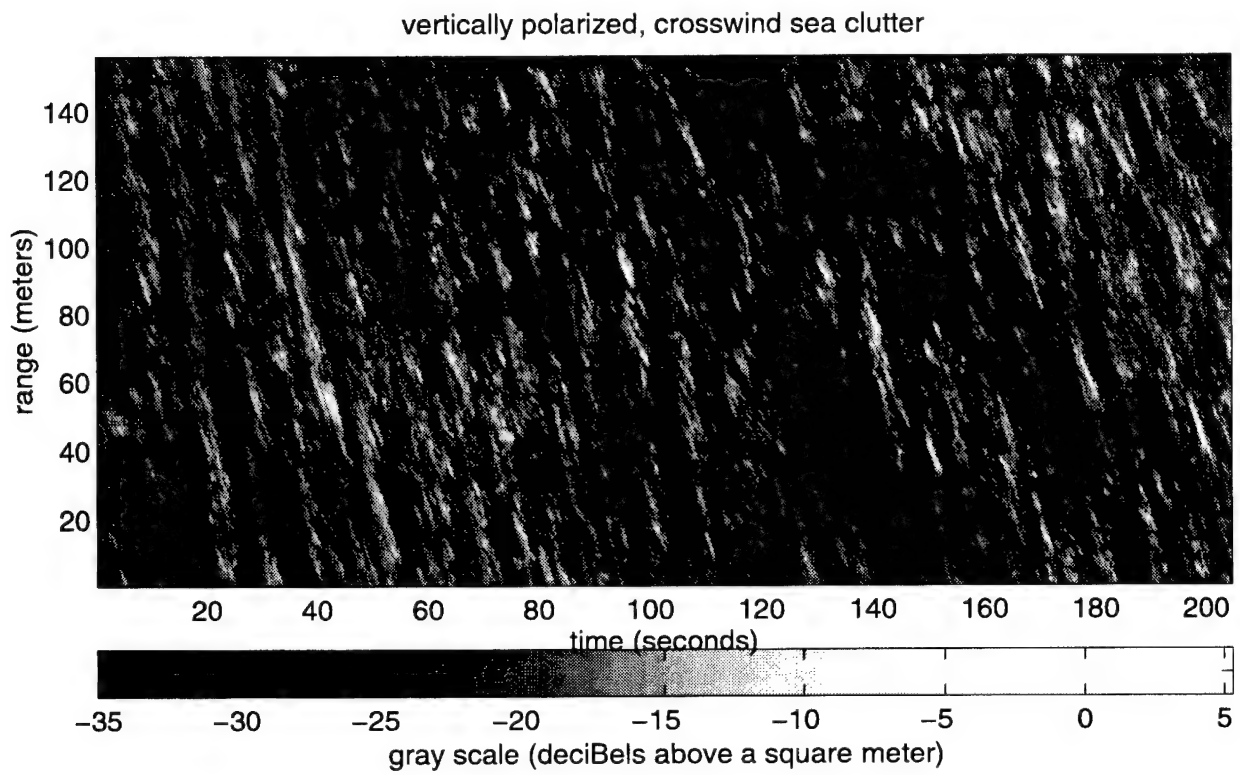
gray scale (deciBels above a square meter)

Figure 2: RTI plots of RCS, in dBsm, for VV (above) and HH (below), CR sea clutter, after noncoherent temporal averaging.

8

next section.

The HH/UP clutter, at the bottom of Figure 1, differs from the VV/UP clutter, at the top of Figure 1, by being sharper, spikier, and more intermittent, accompanied by visibly larger values of the RCS within the individual waves. This has been experimentally observed by a number of other researchers. (See, for example, Hansen and Cavaleri [Hans 82], for an older reference, Ward [Ward 90], and Werle [Werl 95], for a more recent reference.) The polarization dependent contrast between the two types of UP clutter would appear to follow from VV's sensitivity to a variety of surface features and HH's sensitivity to processes occurring at and just beneath the sea surface that are aligned with the wave front, and hence, perpendicular to the radar's line of sight.

The VV/CR clutter, at the top of Figure 2, differs from the VV/UP clutter by exhibiting a broadening, or smearing, of the regular, wavelike pattern, which is still very much in evidence, accompanied by a somewhat noticeable increase in the overall RCS. Both of these observations are somewhat unexpected, on the grounds of physical intuition and from experimental observations by other researchers. The freshening winds and increasing waves that were recorded during this particular data run must have contributed to the observed increase in RCS, but further explanation is still needed.

One would expect such a broadened, but still fairly regular, wavelike pattern from a transmit geometry that is no longer aligned parallel with the wind and incoming waves, but which is also not quite completely perpendicular to them. In the case of a transmit geometry that is only imperfectly CR, the relatively wide cross-range footprint of the radar, on the order of 270 meters for these measurement geometries, is no longer perfectly aligned with the incoming waves, and thus, with wavelengths on the order of 70 meters, will often include a mixture of crests and troughs. Furthermore, the observed increase in RCS is a less surprising result if it turns out that the actual transmit geometry was indeed only imperfectly CR.

As discussed above, when the wide cross-range footprint of the radar is aligned parallel with the incoming waves, in an UP transmit geometry, there is an enhancement of wavelike patterns traveling parallel to the radar's line of sight. When the wide cross-range footprint of the radar is aligned perpendicular to the incoming waves, in a CR transmit geometry, there is a suppression of wavelike patterns traveling parallel to the radar's line of sight. The fact that the VV/CR RTI has such a distinctly visible large-scale wavelike pattern mitigates against its being considered truely CR. Another piece of evidence that this data is only imperfectly crosswind, and has much in common with UP data, is that the speed of the basic, large-scale wave phenomena, once again simply determined from the observed slopes of individual streaks running from the top to the bottom of the RTI plot, is on the order of 12 meters per second, just as was observed for both the VV/UP and the HH/UP clutter.

The HH/CR clutter, at the bottom of Figure 2, differs from the HH/UP clutter by being significantly more intermittent, almost to the point of losing the regular, wavelike pattern present in the examples of the other types of clutter. There is also a significant decrease in average RCS compared with the HH/UP clutter, along with a conspicuous absence of regions with large RCS. In these two matters, the first being the faintness of any visible large-scale wavelike pattern, such as the streaks observed in the other examples, the second being the diminished levels of the RCS, this data is consistent with what would be expected from a measurement of sea clutter with a transmit geometry that is fully CR, thus making it unlike, in that fundamental respect, any of the other examples considered. With essentially

no large-scale structures in the HH/CR RTI, all that remains are the smaller-scale structures, much like the substreaks observed in the other examples. The slopes of these smaller-scale structures correspond to speeds only on the order of 5 meters per second, which is, once again, roughly on the order of the predicted group speeds for these sea conditions.

We will now examine the long time scale, full range swath, data sets in this section by taking the four previously discussed 512 by 2048 element arrays of RCS data, in square meters, as a function of range, in meters, and of time, in seconds, and perform a two-dimensional Fourier transform upon them. Before the Fourier transform, we subtract the global mean from each data set, thus removing the large peak that would otherwise appear at the origin in frequency space. After taking, for each of the elements in the resulting 512 by 2048 element arrays, the magnitude and squaring it, we then have, for all four types of clutter, a power spectral density (PSD) of the original RCS data. The PSD is a function of temporal frequency (ω), in inverse seconds (or Hz), and spatial frequency, or wavenumber (k), in inverse meters. These power spectral densities are sometimes referred to as ω–k plots or sea surface dispersion diagrams.

Sets of clutter data that are low pass filtered by having been noncoherently integrated 200 pulses-to-1 were used for these two-dimensional Fourier transforms because such data sets do not suffer from the significant aliasing problems that do, on the other hand, affect data sets that are low pass filtered by having been downsampled every 200 pulses. Because the low pass filtered RCS data have an effective temporal resolution of 10 Hz, the temporal frequency extent of these PSDs is from -5 Hz to $+5$ Hz. Because the RCS data have a range resolution of 0.3 meters, the spatial frequency extent of these PSDs is from -1.64 inverse meters to $+1.64$ inverse meters.

Figure 3 consists of three-dimensional views of normalized PSDs for UP sea clutter occurring over long time scales and full range swaths. Within Figure 3, the data in the top image is VV and the data in the bottom image is HH. Figure 4 consists of three-dimensional views of normalized PSDs for CR sea clutter occurring over long time scales and full range swaths. Within Figure 4, the data in the top image is VV and the data in the bottom image is HH.

For all four types of clutter, only the first quadrant of the normalized PSD is displayed, extending between 0 Hz and 1 Hz along the temporal frequency axis, and between 0 inverse meters and 0.2 inverse meters along the spatial frequency axis. This excerpted region of the first quadrant of two-dimensional frequency space includes all of the truly significant variations in the different PSDs, with relatively little spectral content occurring at temporal frequencies greater than 1 Hz and at spatial frequencies greater than 0.2 inverse meters. In the second quadrant, corresponding to negative temporal frequencies and positive spatial frequencies, there is very little significant spectral content whatsoever. Since all of the PSDs are symmetric under simultaneous inversion of the spatial and temporal axes, the third quadrant, corresponding to negative temporal and spatial frequencies, is the mirror image of the first, and the fourth quadrant, corresponding to positive temporal frequencies and negative spatial frequencies, is the mirror image of the second.

It should be noted that, for all four types of clutter, the entire PSD array was normalized by dividing each of its elements by the maximum value which occurred in the array. Although the peak value in a normalized PSD array is always one, the original peak value of the PSD, before the normalization, varied for the different types of clutter. The HH/UP
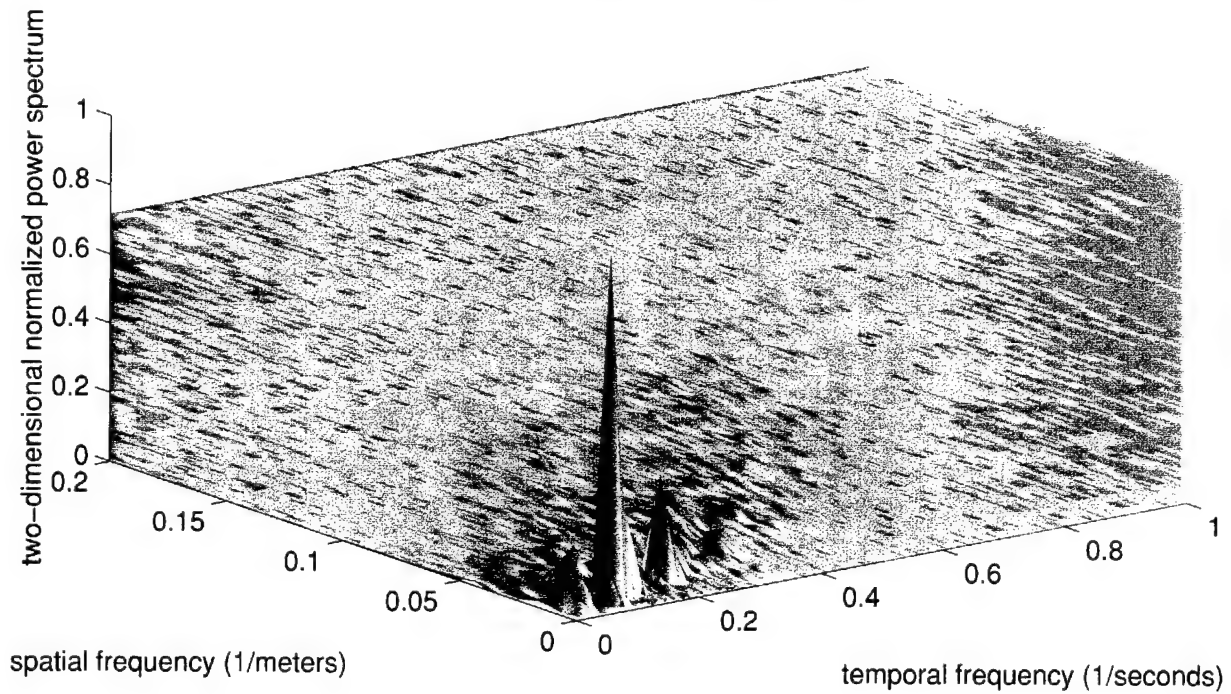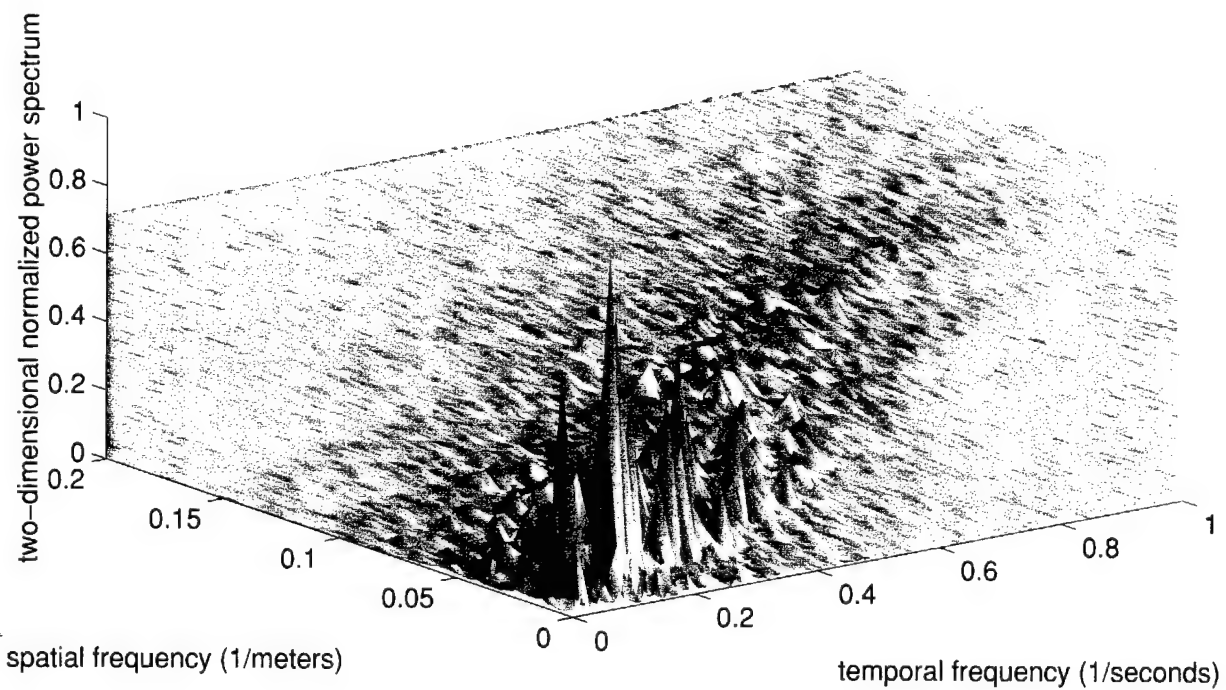
Figure 3: Normalized PSDs (three-dimensional views) for VV (above) and HH (below), UP sea clutter, after noncoherent temporal averaging.

11

vertically polarized, crosswind sea clutter

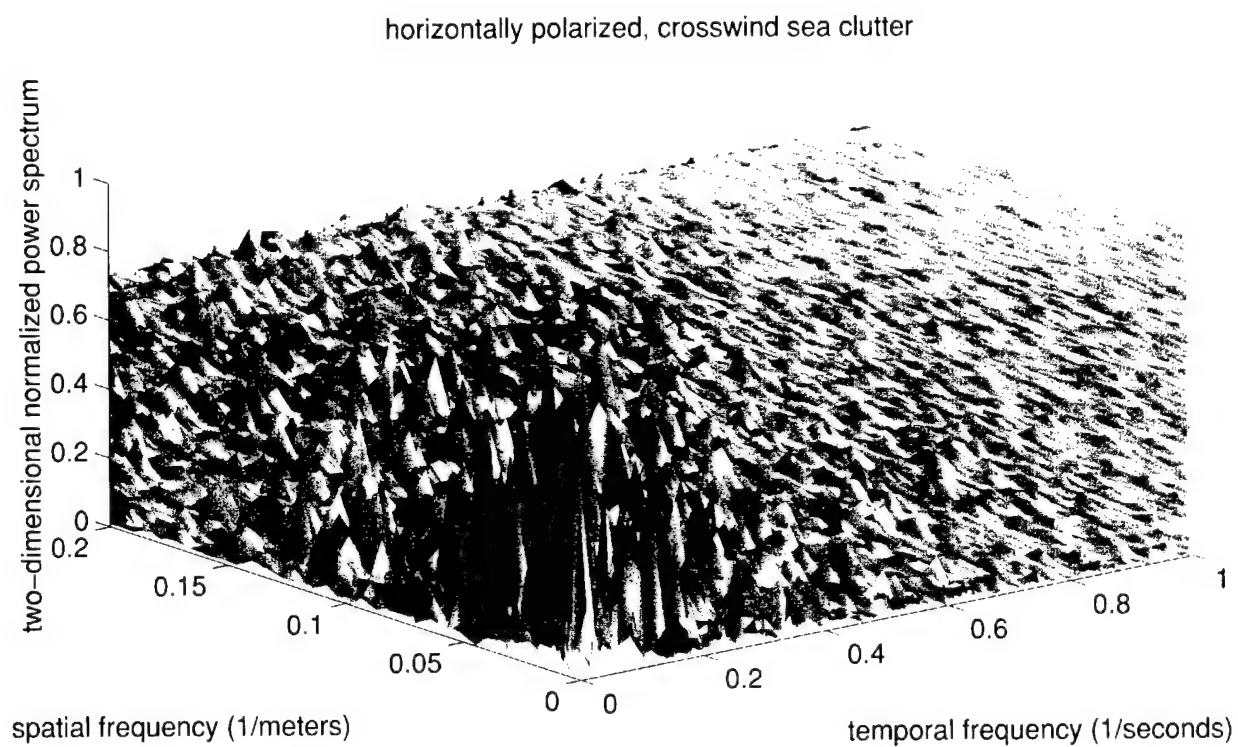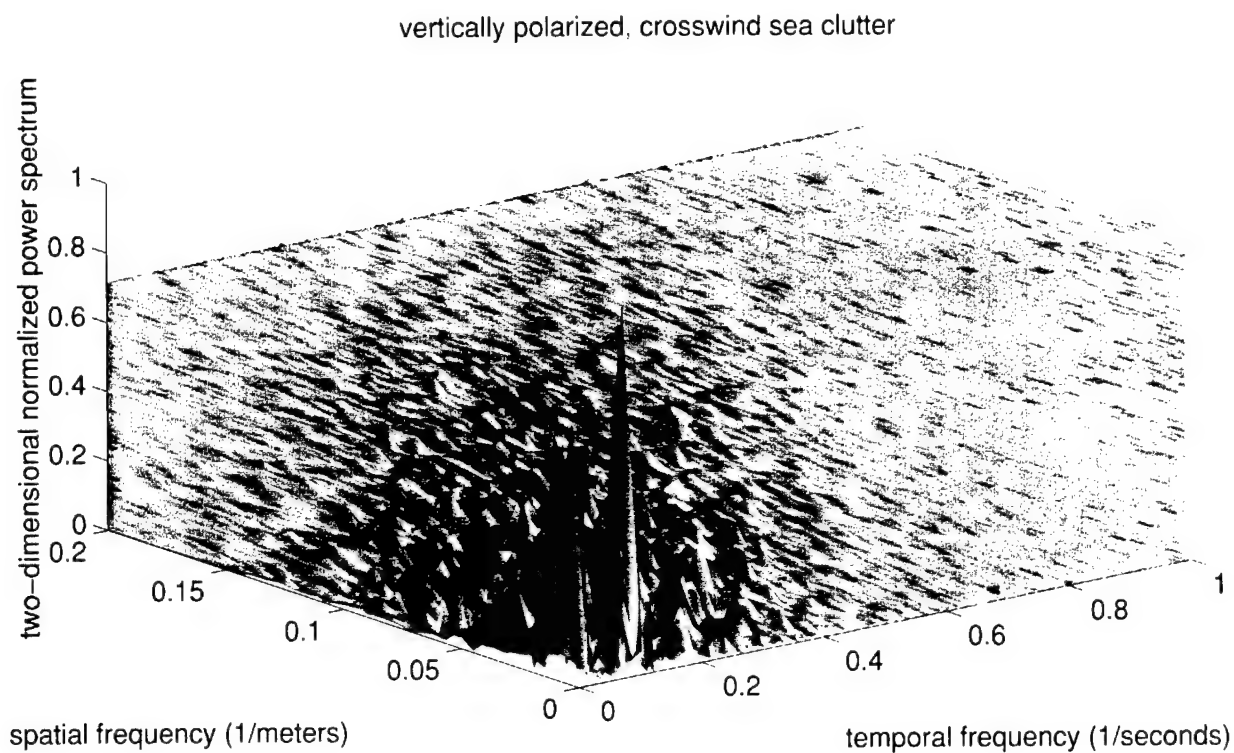horizontally polarized, crosswind sea clutter

Figure 4: Normalized PSDs (three-dimensional views) for VV (above) and HH (below), CR sea clutter, after noncoherent temporal averaging.

clutter had the largest peak; the VV/CR clutter had the second largest peak, 0.745 times as large as the HH/UP peak; the VV/UP clutter had the third largest peak, 0.577 times as large as the HH/UP peak; the HH/CR clutter had the smallest peak, 0.013 times as large as the HH/UP peak. That the VV/CR peak was second largest is somewhat anomalous, but can probably be explained by a combination of transmit misalignment, stronger winds, and increased wave heights, as discussed above. Otherwise, the relative magnitudes of the PSD peaks is consistent with what one would expect.

Two-dimensional renderings of three-dimensional data are never totally satisfactory, and the three-dimensional views of normalized PSDs in Figures 3 and 4 are perhaps better at conveying some of their qualitative, rather than their quantitative, features. Another way of looking at power spectra, one which complements the above three-dimensional approach, is to take the normalized PSD amplitudes, which vary between zero and one, and plot them in gray-scale variation as a two-dimensional function of spatial and temporal frequency.

Figure 5 consists of two-dimensional views of normalized PSDs for UP sea clutter occurring over long time scales and full range swaths. Within Figure 5, the data in the top image is VV and the data in the bottom image is HH. Figure 6 consists of two-dimensional views of normalized PSDs for CR sea clutter occurring over long time scales and full range swaths. Within Figure 6, the data in the top image is VV and the data in the bottom image is HH.

For all four types of clutter, only the central region of the PSD is displayed, between -1 Hz and $+1$ Hz along the temporal frequency axis, and between -0.2 inverse meters and $+0.2$ inverse meters along the spatial frequency axis. This corresponds to the three-dimensional views, where, within the first quadrant, the maximum temporal frequency was 1 Hz and the maximum spatial frequency was 0.2 inverse meters. Since now all four quadrants are displayed, it is possible to directly verify that all of the PSDs are symmetric under simultaneous inversion of the spatial and temporal axes. Note that in these plots, the normalized PSDs have been displayed on a logarithmic scale, where the maximum value is at 0 dB and where the data has been cut off at a minimum value of -20 dB. In other words, we are only displaying those frequency components whose amplitudes are at least one per cent of the amplitude of the peak frequency.

The maximum value of the PSD occurs for VV/UP at 0.103 Hz and 0.013 inverse meters, corresponding to a period of 9.7 seconds and a wavelength of 76.9 meters; and for HH/UP at 0.107 Hz and 0.013 inverse meters, corresponding to a period of 9.3 seconds and a wavelength of 76.9 meters. The locations of the spectral peaks of the two UP PSDs are very similar, which, upon examining the two UP RTIs in Figure 1, with their similar large-scale wave structures, is not a surprising result. A monochromatic wave corresponding to a particular spectral peak has a phase velocity given by the ratio of the peak's temporal frequency coordinate to the peak's spatial frequency coordinate. The phase velocity of the monochromatic wave associated with the VV/UP PSD peak is 7.9 meters per second, and for the HH/UP PSD peak it is 8.2 meters per second.

The maximum value of the PSD occurs for VV/CR at 0.147 Hz and 0.019 inverse meters, corresponding to a period of 6.8 seconds and a wavelength of 52.6 meters; and for HH/CR at 0.020 Hz and 0.019 inverse meters, corresponding to a period of 50 seconds and a wavelength of 52.6 meters. The location of the VV/CR spectral peak is somewhat higher, by a factor of about a half, in both temporal and spatial frequency, than the VV/UP peak, a
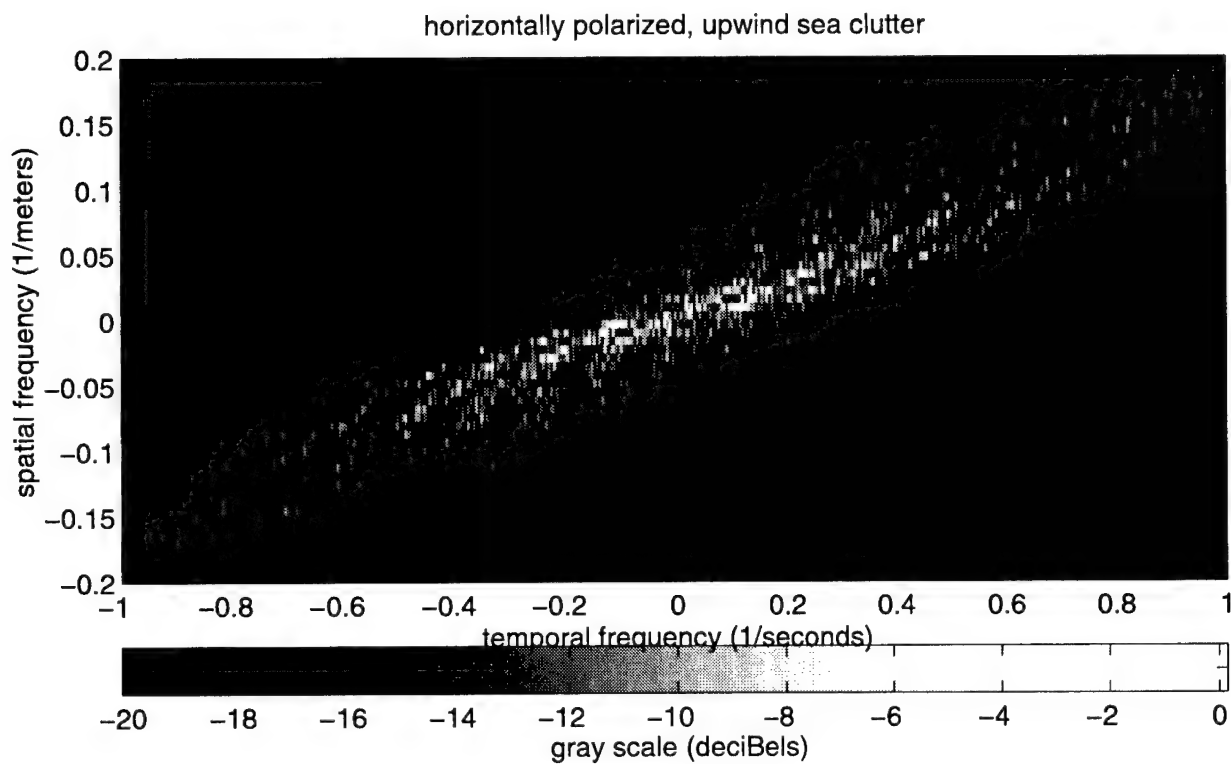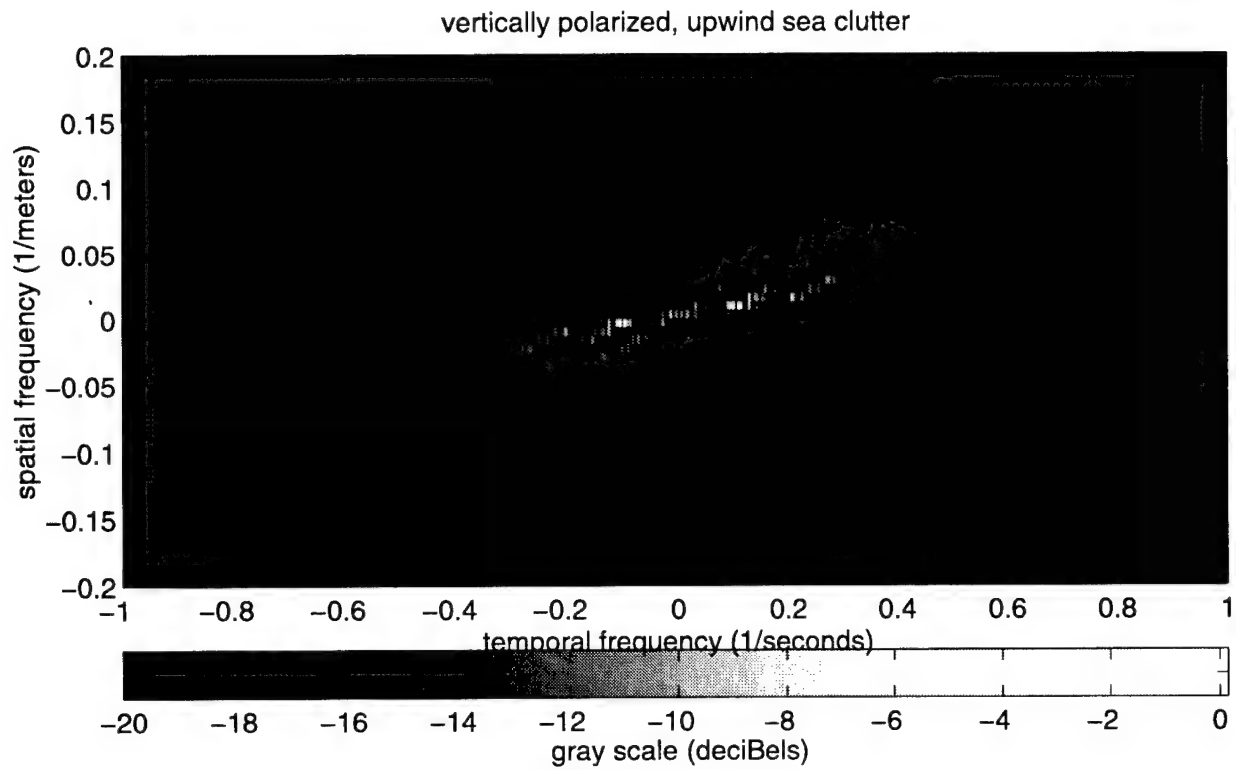
Figure 5: Normalized PSDs (two-dimensional views), in dB, for VV (above) and HH (below), UP sea clutter, after noncoherent temporal averaging.
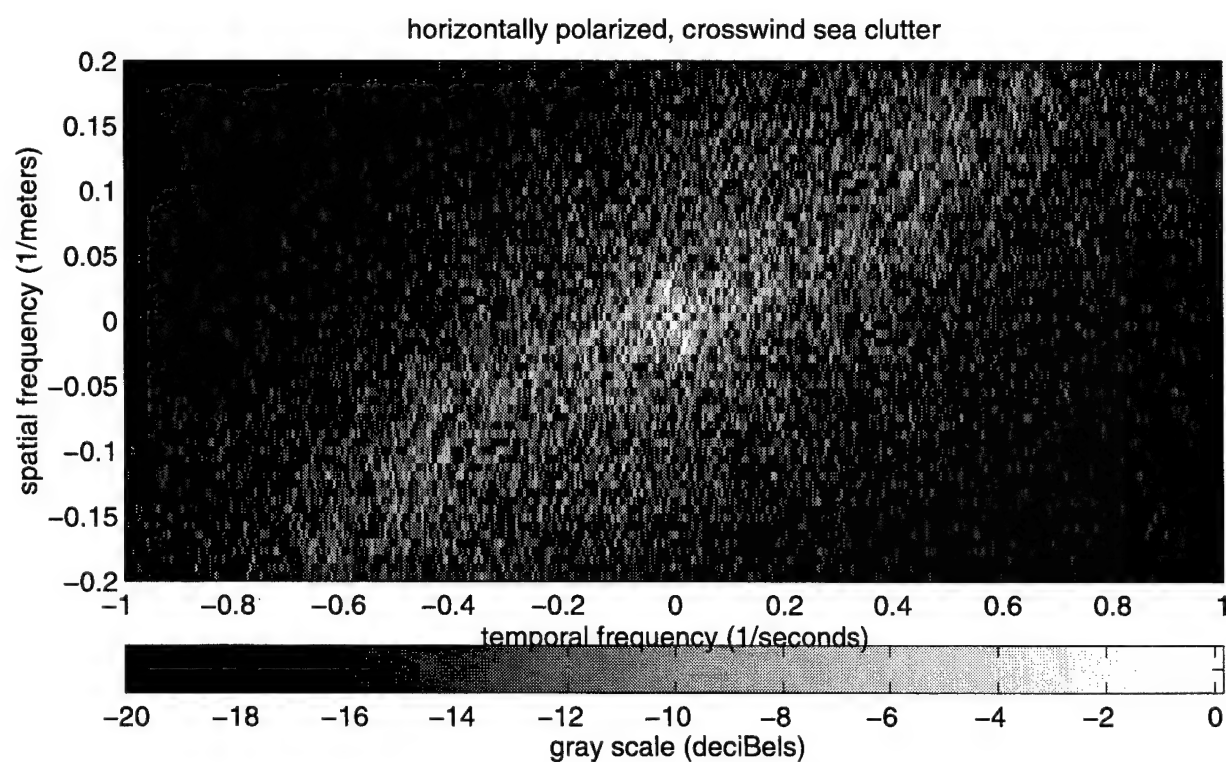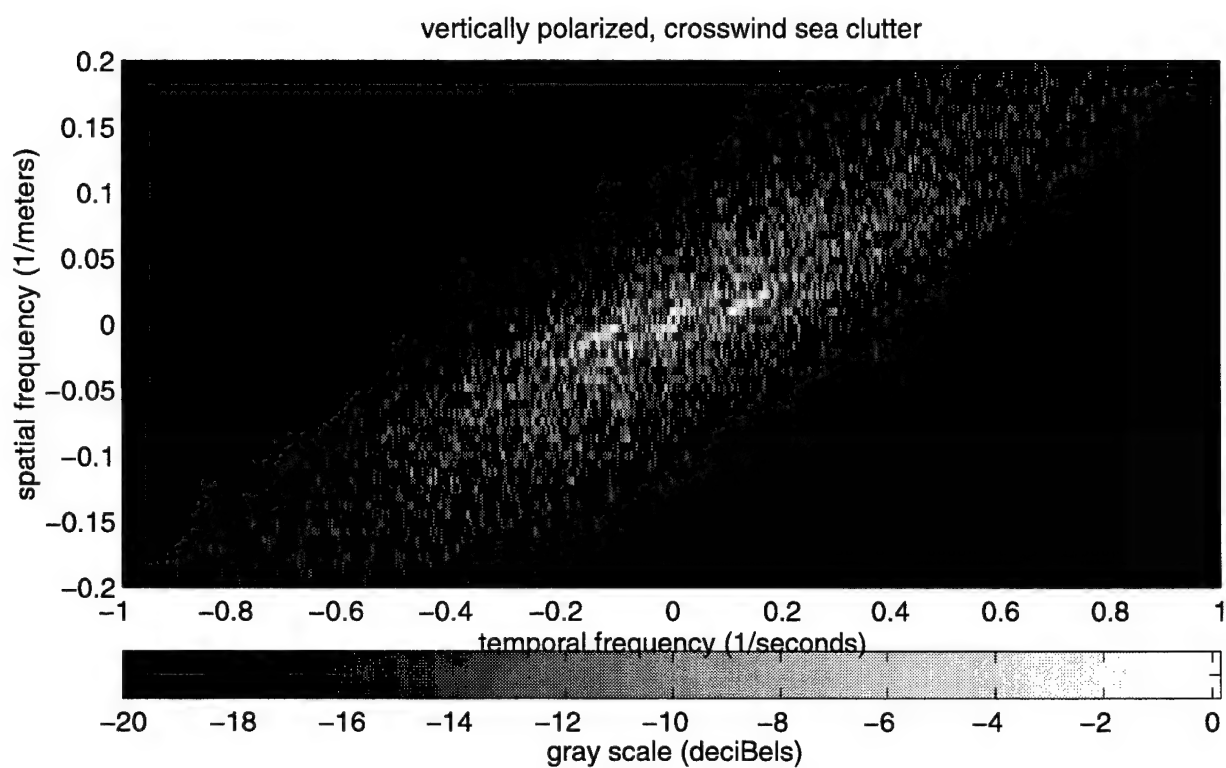
14

Figure 6: Normalized PSDs (two-dimensional views), in dB, for VV (above) and HH (below), CR sea clutter, after noncoherent temporal averaging.

result that is consistent with the broadened large-scale wave structure in the RTI at the top of Figure 2, and which is due to a measurement of VV clutter that is only imperfectly CR. The location of the HH/CR spectral peak, with its very small temporal frequency, is quite different from that of the other spectral peaks, a result that is consistent with the almost complete absence of large-scale wave structure in the RTI at the bottom of Figure 2, and which is indicative of a measurement of HH clutter that is CR. The phase velocity of the monochromatic wave associated with the VV/CR PSD peak is 7.7 meters per second, and for the HH/CR PSD peak it is 1.1 meters per second.

Each of the PSD plots is dominated by the presence of a characteristic spectral ridge, which reveals the inherent wave group structure. For the UP data, examination of the three-dimensional PSDs, in Figure 3, and the two-dimensional PSDs, in Figure 5, indicates that the spectral ridge extends further out from the origin, and is wider and more complexly structured, for the HH clutter than for the VV clutter. For the CR data, examination of the three-dimensional PSDs, in Figure 4, and the two-dimensional PSDs, in Figure 6, indicates that the spectral ridge is strong and compact for the VV clutter, and weak and diffuse for the HH clutter.

For the VV data, the spectral ridge extends further from the origin, and is wider, for CR clutter than for UP clutter. For the HH data, UP clutter has a very strong and well-defined spectral ridge, while CR clutter has a rather weak and ill-defined spectral ridge. For both polarizations, there is a counterclockwise rotation of the spectral ridge as one compares the UP PSD to the CR PSD. This rotation appears somewhat larger for the HH clutter than for the VV clutter. The VV/UP and HH/UP spectral ridges are more or less parallel, while the HH/CR spectral ridge appears to have swung past the VV/CR spectral ridge. An explanation for this may lie in the fact that, to change the transmit geometry from UP to CR, there was a clockwise rotation for the antenna of 72 degrees for VV, and a counterclockwise rotation for the antenna of 41 degrees for HH.

The group speed, which is defined as the derivative of the temporal frequency with respect to the spatial frequency, would be given by the inverse of the slope of the spectral ridge appearing in the two-dimensional PSD plot. The slopes of the two fairly well-defined UP spectral ridges, in Figure 5, are comparable, and give group speeds on the order of 5 meters per second for UP clutter, which are roughly on the order of the predicted group speeds for these sea conditions. The slopes of the two much less well-defined CR spectral ridges, in Figure 6, are reasonably comparable, and give group speeds on the order of 4 meters per second for CR clutter, which are also roughly on the order of the predicted group speeds for these sea conditions.

The two-dimensional PSDs, in Figures 5 and 6, with their single prominent spectral ridges, do indeed look the way one would expect the two-dimensional Fourier transforms of the RTI plots of RCS, in Figures 1 and 2, with their very regular large-scale wavelike structure, upon which is superimposed a smaller-scale structure, to look. When one examines some other sea clutter data, where the RTI plots of RCS display a more complicated, less obviously regular, wavelike structure, one then finds that the two-dimensional PSDs of such data contain a main spectral ridge along with some outlying secondary ridges. (See, for example, Eckert et al. [Ecke 94], Ochadlick et al. [Ocha 94], Siegal et al. [Sieg 94], Frasier and McIntosh [Fras 96], and Werle [Werl 95].) But then, it should not be surprising that there would be differences in the backscatter data, as evidenced in plots of intensities and

spectra, gathered from the windward shore of Kauai, when compared with backscatter data gathered from such contrasting locations as the Chesapeake Light Tower off Virginia Beach, Virginia, a pier near Duck, North Carolina, and from Loch Linnhe and the Sound of Sleat in Scotland.

4   Intermediate Time Scales and Partial Range Swaths

In this section, we will consider examples of backscatter data whose extents in time are on the order of 5 seconds, and whose extents in range are over partial range swaths on the order of 30 meters. The images in Figures 7 and 8 are RTI plots of RCS for four different UP sea clutter events occurring over intermediate time scales and partial range swaths. The polarization in Figure 7 is HH and the polarization in Figure 8 is VV. Within both Figures 7 and 8, the image at the top corresponds to events numbered one and the image at the bottom corresponds to events numbered two.

The dynamic range of the data as presented in the HH/UP plots, in Figure 7, covering 40 dB and extending from −35 dBsm to +5 dBsm, is the same as for the examples of long time scale and full range swath data discussed in the previous section. The dynamic range of the data as presented in the VV/UP plots, in Figure 8, also covers 40 dB, but with their smaller returns, a dynamic range extending from −40 dBsm to 0 dBsm resulted in clearer images.

It should be noted that, throughout this section, as well as for the rest of this report, all of the data to be presented and discussed will be at the full temporal resolution of 2000 Hz. Events numbered one consist of 10000 pulses and 128 range cells, which is a quarter of the entire range swath, while events numbered two consist of 8000 pulses and 100 range cells. To get to the scale of these events, we have zoomed by a factor of 40 or 50 in time, and by a factor of 4 or 5 in range, from the examples of long time scale and full range swath data discussed in the previous section. Finally, it should be remarked that the aspect ratios of events one and two are almost identical, and phenomena, such as breaking waves, whose radar returns give rise to RTI image structures with similar slopes in events one and two, can be inferred to have similar velocities.

The highly dynamic variability, both temporal and spatial, and the complex substructure of an extended event are clearly visible in these RTI plots. It could even be argued that to refer to what is going on in these examples of backscatter data in the singular, as an individual, albeit extended, event, is a somewhat misleading simplification. Examination of these images fully supports the observation from the previous section that HH/UP sea clutter is sharper, spikier, and more intermittent than VV/UP sea clutter.

Note, as examples, in HH/UP event one, at the top of Figure 7, the very large magnitude ridge whose (time, space) coordinates extend between (0 seconds, 24 meters) and (5 seconds, 0 meters); and in VV/UP event one, at the top of Figure 8, the large magnitude ridge whose (time, space) coordinates extend between (1.5 seconds, 21 meters) and (4 seconds, 9 meters). Both examples are indicative of microwave-reflective phenomena that propagate with a speed of 4.8 meters per second. By way of comparison, for a wind speed of 9 meters per second, the theoretically predicted group speed for fully-developed deep water waves is 5 meters per second, as was discussed in an earlier section. This lends

horizontally polarized, upwind sea clutter: event one
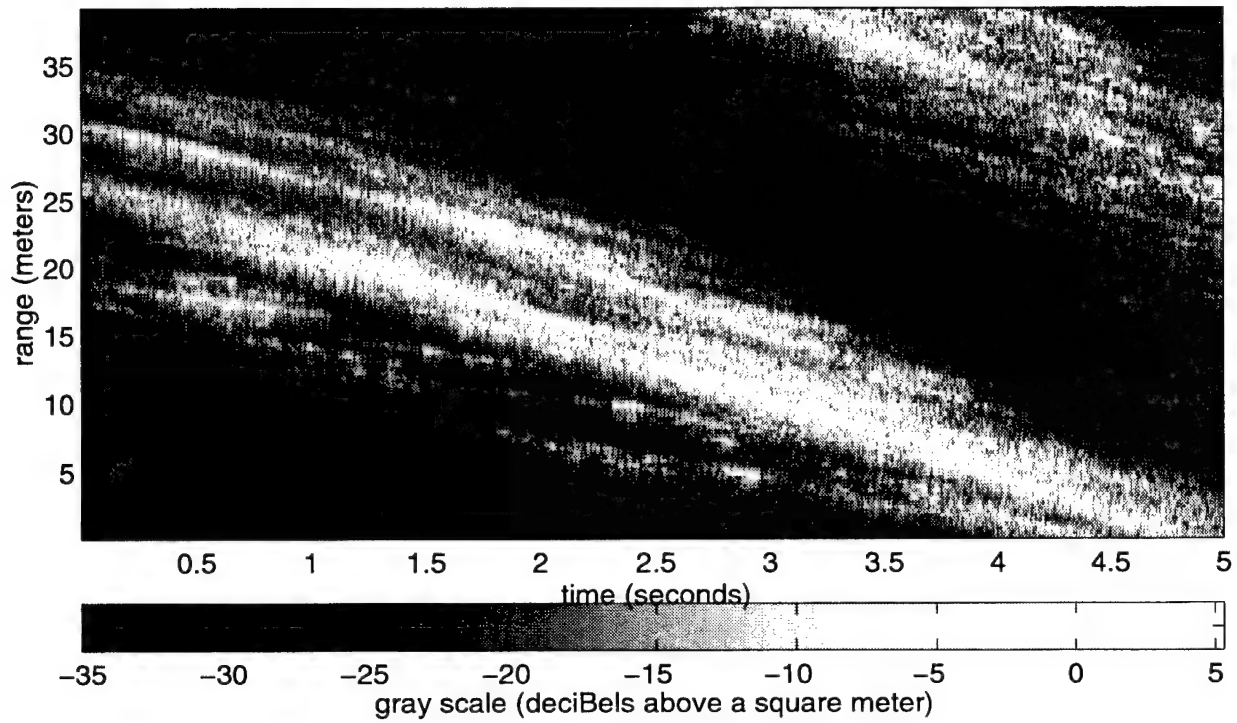
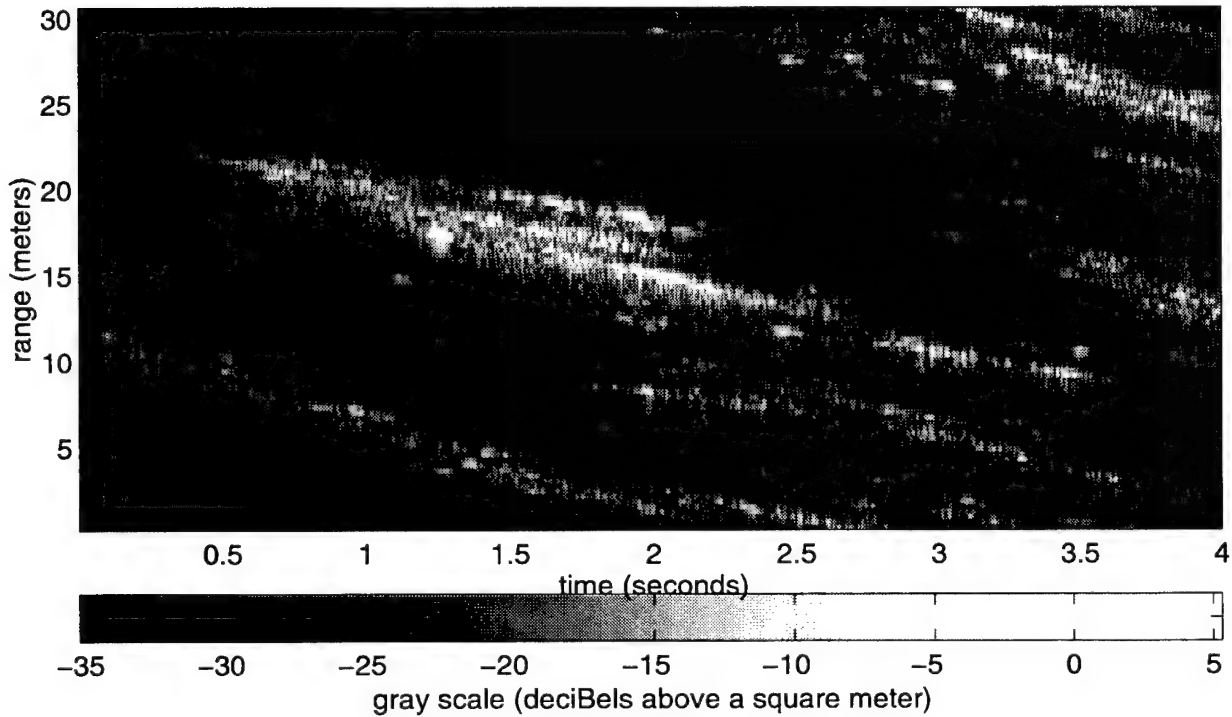horizontally polarized, upwind sea clutter: event two

Figure 7: RTI plots of RCS, in dBsm, of characteristic and contrasting events one (above) and two (below), illustrating HH/UP sea clutter.
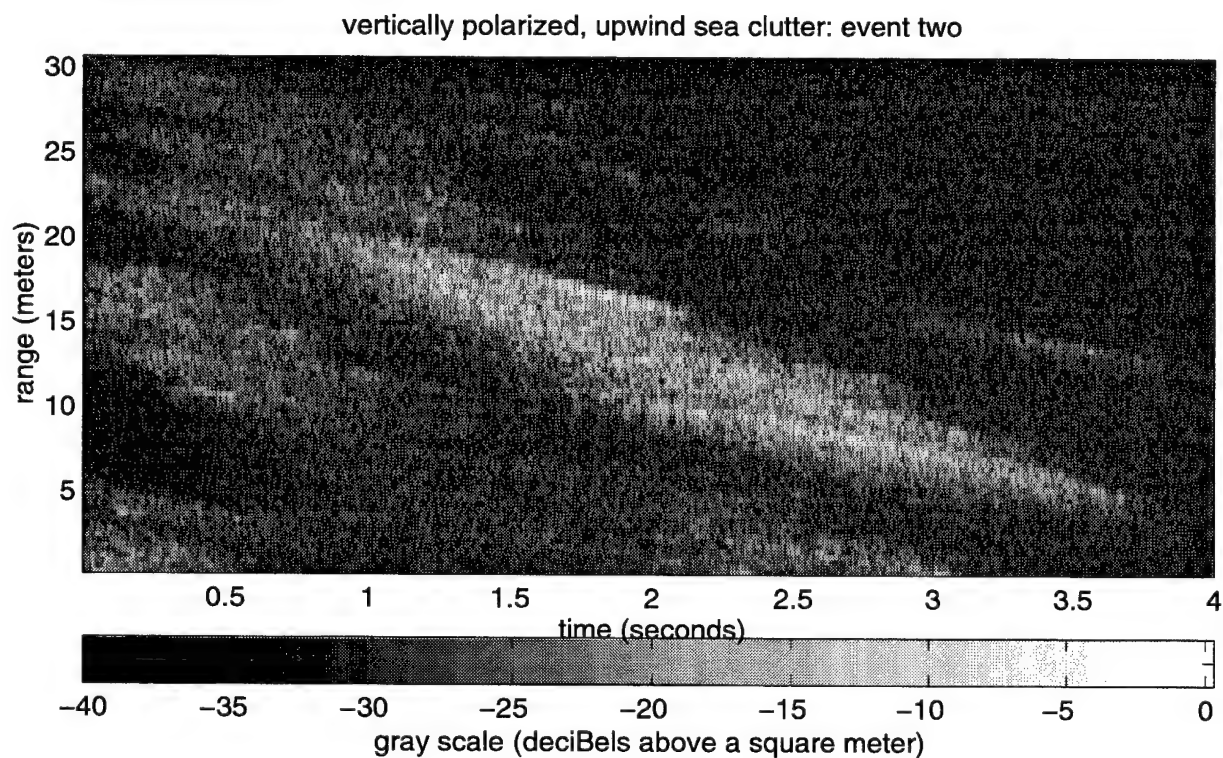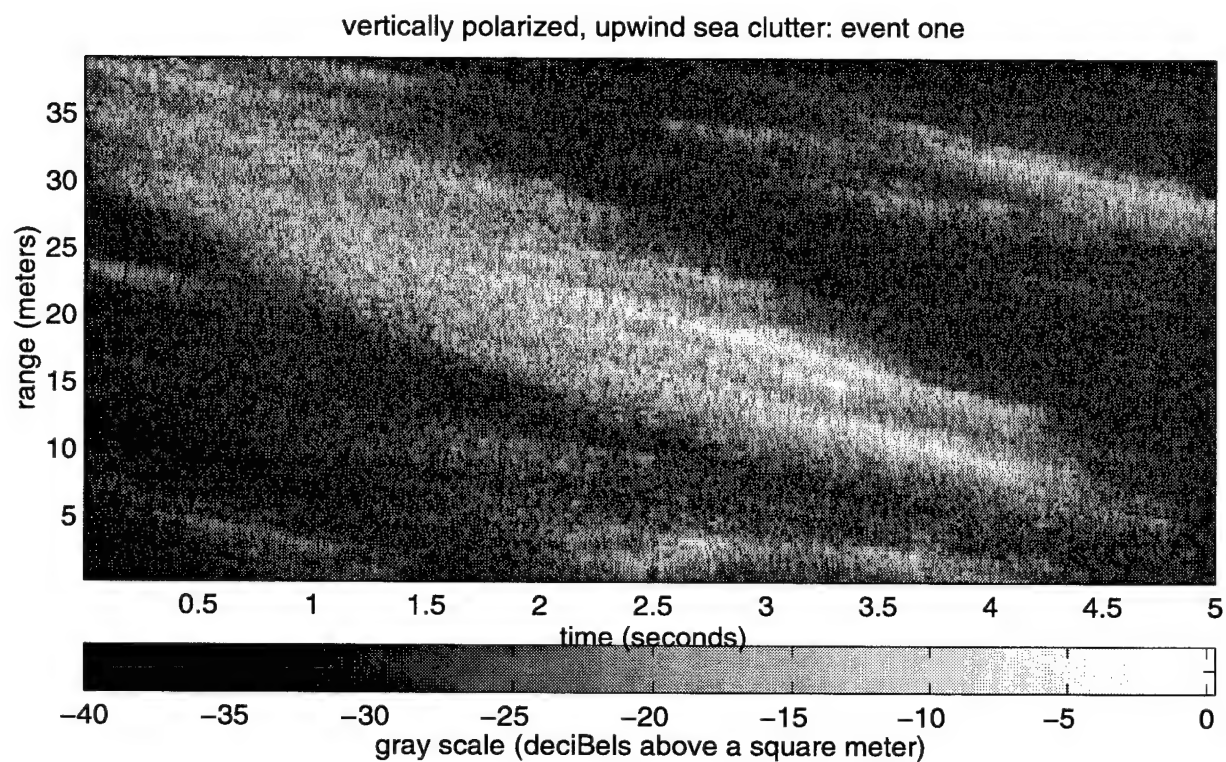
18

vertically polarized, upwind sea clutter: event one

vertically polarized, upwind sea clutter: event two

Figure 8: RTI plots of RCS, in dBsm, of characteristic and contrasting events one (above) and two (below), illustrating VV/UP sea clutter.

support to the claim that radar images pick out phenomena that propagate at group speeds. (See Werle [Werl 95].)

In Figure 9, at the top, there is a linear plot of the probability density function (PDF) of all of the data in HH/UP event one, and at the bottom, there is a similar plot for HH/UP event two. In both plots of Figure 9, the RCS amplitudes, plotted along the x-axis, extend from −20 dBsm to +5 dBsm, thus covering the 25 dBsm range over which one would expect to find that sea clutter data, within all of the data in HH/UP events one and two, which can be safely considered to be uncontaminated by various forms of noise. In Figure 10, at the top, there is a linear plot of the PDF of all of the data in VV/UP event one, and at the bottom, there is a similar plot for VV/UP event two. In both plots of Figure 10, the RCS amplitudes extend from −25 dBsm to 0 dBsm, which is the corresponding 25 dBsm range for that sea clutter data, within all of the data in VV/UP events one and two, which can be safely considered to be uncontaminated by various forms of noise. In all of these events, the data with smaller RCS amplitudes would tend to be increasingly dominated by various forms of noise, such as receiver noise and quantization noise, as will be discussed later in this section.

The PDFs were generated by first performing a frequency count of all of the data within the entire event, and then normalizing the resulting frequency count, or histogram, by the total number of data points. The bin width for the histogramming process was 0.1 dBsm. It should be noted that the PDF, plotted along the y-axis, is restricted to a maximum possible value of 0.0035 in both the upper and lower plots of Figure 9, and a maximum possible value of 0.006 in both the upper and lower plots of Figure 10. It is to be understood that the PDFs of these four different UP sea clutter events, occurring over intermediate time scales and partial range swaths, with their very specific selection and their deliberate constraint in amount of data, are not being used for purposes of rigorous statistical modeling, but rather to gain additional insight into the various phenomena taking place and to aid in the search for overall similarities, differences, and contrasts.

The double-humped peaks, which are very conspicuous at the high ends of the PDFs for HH/UP event one, at the top of Figure 9, and VV/UP event one, at the top of Figure 10, but which are very much harder to detect, at least on this scale, in the PDFs for HH/UP event two, at the bottom of Figure 9, and VV/UP event two, at the bottom of Figure 10, are the effects of clipping. The clipping of the largest returns, which do occur only relatively rarely, was the unavoidable consequence, with a radar of this somewhat limited dynamic range, of making the very reasonable decision that the radar operator needed to see some return on his scope some of the time, rather than no return most of the time. To implement this operational philosophy, the operator, towards the beginning of each of these spotlight data collection runs, would set the gain appropriately, and it would then remain fixed until the next run.

It is really only after the data has been gathered that the unfortunate effects of the clipping make themselves felt. If the analysis of the clutter requires data that has been uncorrupted by clipping, then there will be more problems investigating those events characterized by large radar returns that occur frequently. Such events are, no doubt, those of greatest interest, but analysis of events less affected by clipping can still be very informative. In practice, this means that data, from the HH/UP collection run from which HH/UP event one was taken, and whose RCS is on the order of 1.0 dBsm (1.26 sm) or above, is suspect,
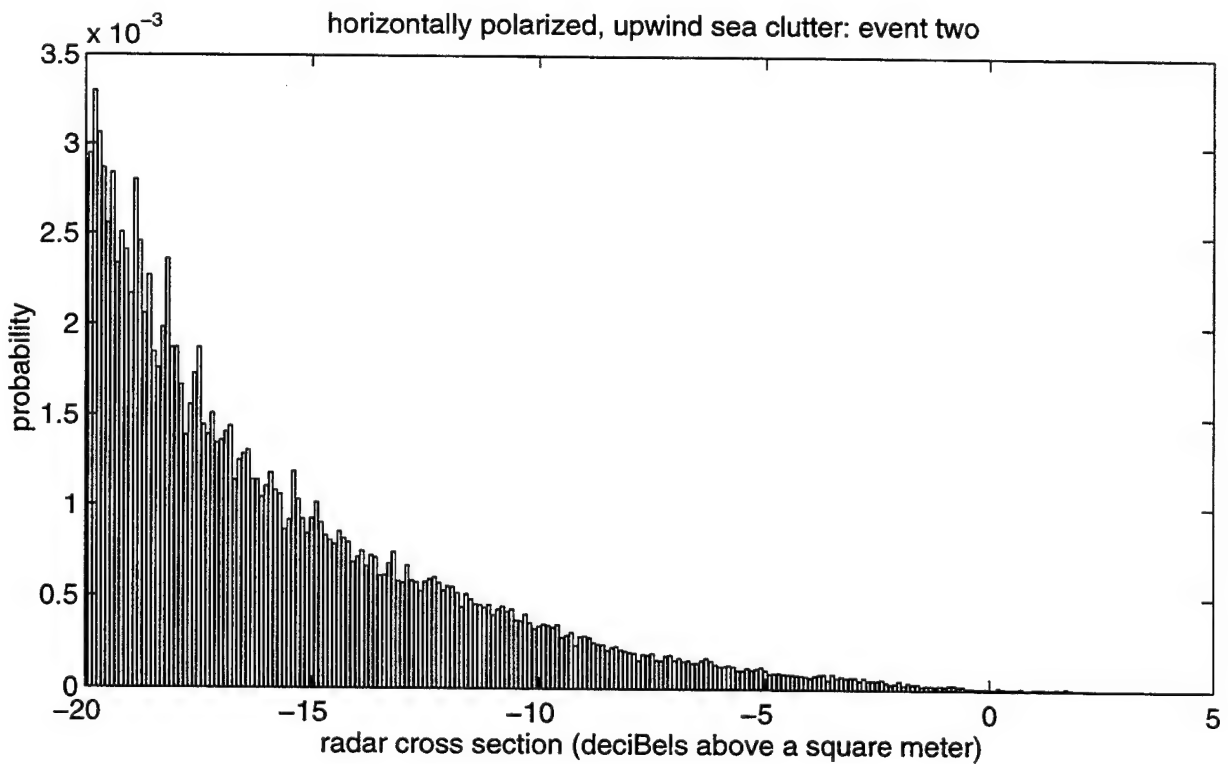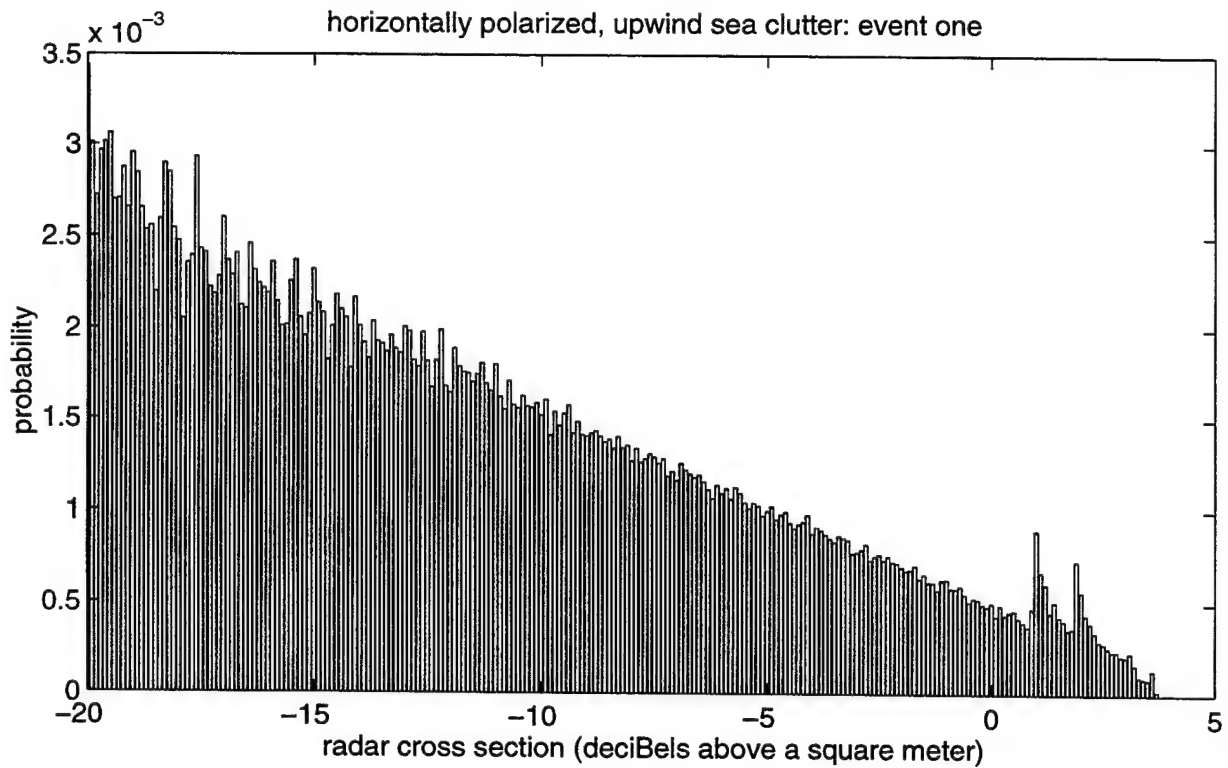
Figure 9: Truncated (larger magnitude returns) PDFs (linear plots) of all data within characteristic and contrasting events one (above) and two (below), illustrating HH/UP sea clutter.
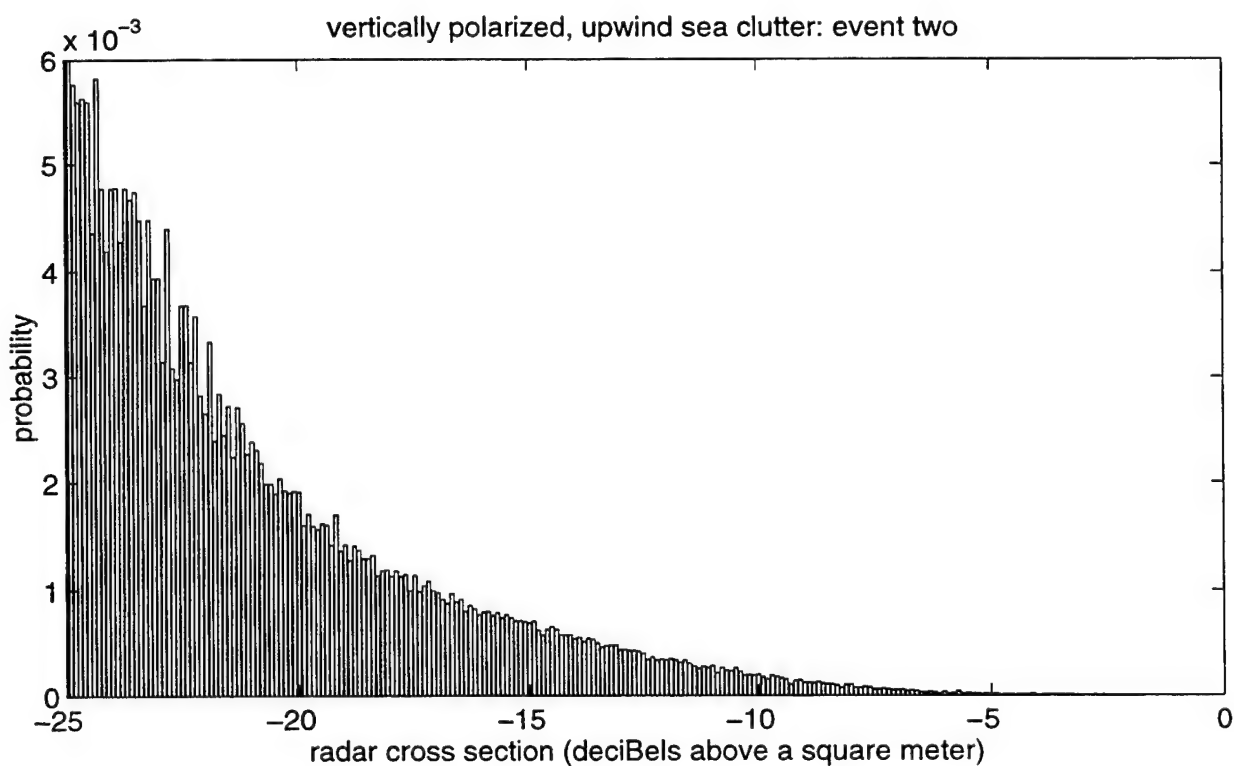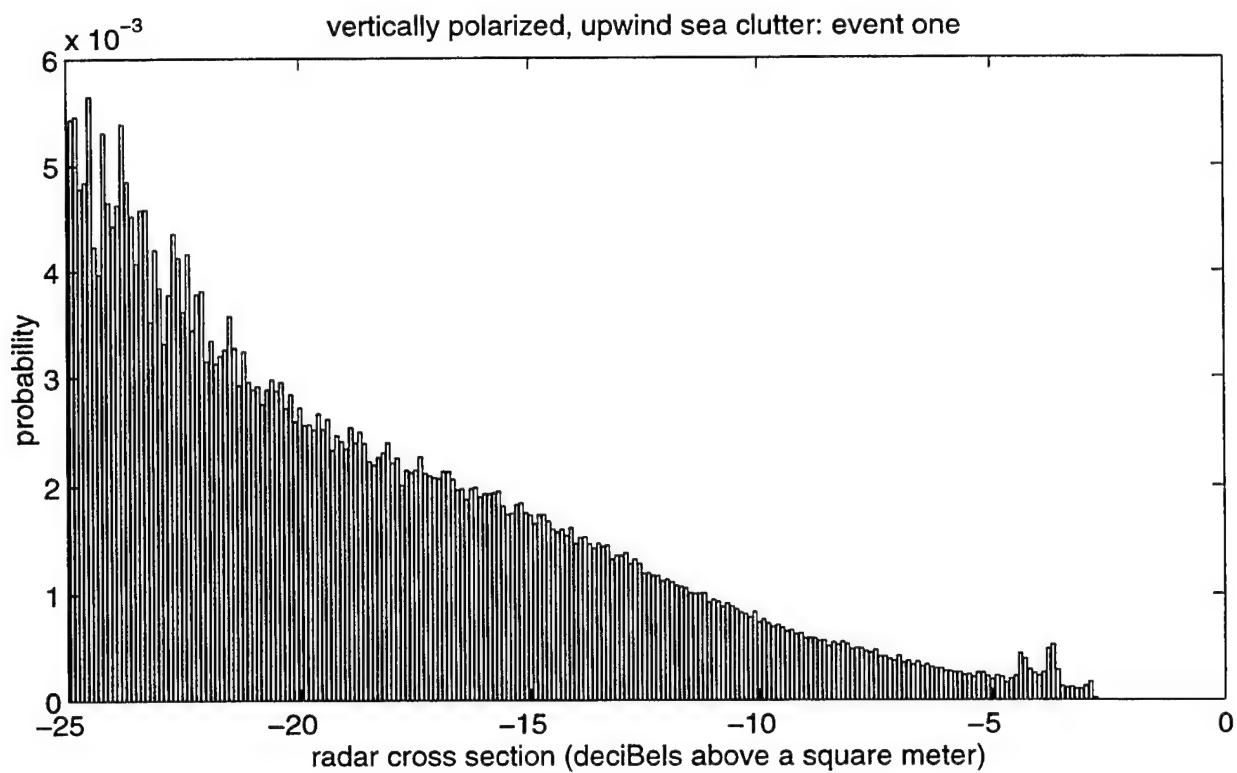
Figure 10: Truncated (larger magnitude returns) PDFs (linear plots) of all data within characteristic and contrasting events one (above) and two (below), illustrating VV/UP sea clutter.

22

and that data, from the VV/UP collection run from which VV/UP event one was taken, and whose RCS is on the order of −4.5 dBsm (0.35 sm) or above, is also suspect.

The falloff of the PDF with increasing RCS for all of the data in HH/UP event one is much more gradual, with a distinctly different shape, than it is for all of the data in HH/UP event two. Similarly, the falloff of the PDF with increasing RCS for all of the data in VV/UP event one is more gradual, with a different shape, than it is for all of the data in VV/UP event two. One infers from these comparisons that the two HH/UP events are not just the same event, differing only in some simple way, such as in average RCS, but are distinctly different events, differing between themselves in some complex manner. The same inference can be drawn with regard to the two VV/UP events and their relationship to each other. In fact, with regard to the functional dependence of the PDF upon RCS, the strongest similarities appear to between HH/UP event one and VV/UP event one, and between HH/UP event two and VV/UP event two.

At the top of Figure 11 is a Weibull plot of the cumulative distribution function (CDF) of the RCS data contained within the large magnitude parallelogram in HH/UP event one, whose far horizontal side extends in time between 0.25 seconds and 1.25 seconds, at a range of 22.9 meters, and whose near horizontal side extends in time between 1.5 seconds and 2.5 seconds, at a range of 15.5 meters. In addition, 50000 samples from a Rayleigh distribution with a parameter of 0.1 (−10 dB) were also plotted. This was done because the CDF of Weibull-distributed data will appear as a straight line on Weibull axes, and the Weibull distribution includes, as a special case, the Rayleigh distribution. (The utility of the Weibull distribution in the study of spiky sea clutter is illustrated in the references by Olin [Olin 82, Olin 84].) This statistically-generated Rayleigh CDF is useful as a visual reference and for comparison with the actual data, and will also be generated and plotted in the Weibull plots at the tops of Figures 12, 13, and 14.

At the bottom of Figure 11 is a Weibull plot of the CDF of the RCS data contained within the small magnitude rectangle in HH/UP event one, whose extent in time is between 0 seconds and 1 second, and whose extent in range is between 7.6 meters and 0.3 meters. In addition, 50000 samples from a Rayleigh distribution with a parameter of 0.01 (−20 dB) were also plotted. This statistically-generated Rayleigh CDF will also be generated and plotted in the Weibull plots at the bottoms of Figures 12, 13, and 14. It should be noted that, although the RCS amplitudes, plotted along the x-axis, cover four decades in both plots of Figure 11, they extend from −30 dBsm to +10 dBsm in the upper plot, and from −40 dBsm to 0 dBsm in the lower plot. This will also be the case for Figures 12, 13, and 14. Finally, the CDF percentiles, plotted along the y-axis, are identical in both the upper and lower plots of Figure 11, as they will be in Figures 12, 13, and 14.

At the top of Figure 12 is a Weibull plot of the CDF of the RCS data contained within the large magnitude parallelogram in HH/UP event two, whose far horizontal side extends in time between 0.75 seconds and 1.75 seconds, at a range of 18.9 meters, and whose near horizontal side extends in time between 1.7 seconds and 2.7 seconds, at a range of 13.1 meters. At the bottom of Figure 12 is a Weibull plot of the CDF of the RCS data contained within the small magnitude rectangle in HH/UP event two, whose extent in time is between 1 second and 2 seconds, and whose extent in range is between 30.5 meters and 24.7 meters.

At the top of Figure 13 is a Weibull plot of the CDF of the RCS data contained

within the large magnitude parallelogram in VV/UP event one, whose far horizontal side extends in time between 1.6 seconds and 2.6 seconds, at a range of 22.6 meters, and whose near horizontal side extends in time between 3.05 seconds and 4.05 seconds, at a range of 13.7 meters. At the bottom of Figure 13 is a Weibull plot of the CDF of the RCS data contained within the small magnitude rectangle in VV/UP event one, whose extent in time is between 0 seconds and 1 second, and whose extent in range is between 17.1 meters and 8.2 meters.

At the top of Figure 14 is a Weibull plot of the CDF of the RCS data contained within the large magnitude parallelogram in VV/UP event two, whose far horizontal side extends in time between 1.7 seconds and 2.95 seconds, at a range of 10.7 meters, and whose near horizontal side extends in time between 2.65 seconds and 3.9 seconds, at a range of 4.9 meters. At the bottom of Figure 14 is a Weibull plot of the CDF of the RCS data contained within the small magnitude rectangle in VV/UP event two, whose extent in time is between 2.75 seconds and 4 seconds, and whose extent in range is between 30.5 meters and 24.7 meters.

Once again, as was the case with the PDFs of the four different UP sea clutter events, occurring over intermediate time scales and partial range swaths, it is to be understood that the CDFs of these large magnitude parallelograms and these small magnitude rectangles, with their even more specific selection and their quite deliberate constraint in amount of data, all of which was necessary in order to focus upon either individual spiking events or noise-dominated data, are not being used for purposes of rigorous statistical modeling, but rather to gain additional insight into the various phenomena taking place and to aid in the search for overall similarities, differences, and contrasts.

The PDFs, in Figures 9 and 10, are of all the RCS data in four different UP sea clutter events occurring over intermediate time scales and partial range swaths. Examination of the RTI plots of these events, in Figures 7 and 8, reveal the presence of multiple, individual spiking events which need to be studied in isolation. By contrast with the PDFs, the upper CDFs, those at the tops of Figures 11, 12, 13, and 14, are of the deliberately selected RCS data contained in the large magnitude parallelograms that bound specific, individual spiking events. The temporal width of the parallelogram is the duration of the individual spiking event within a particular range cell. The fact that the bounding shape is a parallelogram, rather than a simple rectangle, attests to the fact that the microwave-reflective phenomenon is propagating inwards, towards the radar, at some finite speed.

Examination of the first two upper CDFs, those at the tops of Figures 11 and 12, reveals the following regarding the two HH/UP individual spiking events. The individual spiking event from HH/UP event one has more returns with larger RCS values, and the clipping is much more conspicuous. Neither of the HH/UP individual spiking events is Rayleigh-distributed. In the critical spiking range between −10 dBsm and 0 dBsm, the CDFs of these two individual spiking events subtly depart from being straight, and thus from being Weibull-distributed, and subtly differ between themselves, with the CDF from HH/UP event one being slightly convex upwards, and the CDF from HH/UP event two being slightly concave upwards.

Similarly, examination of the last two upper CDFs, those at the tops of Figures 13 and 14, reveals the following regarding the two VV/UP individual spiking events. The individual spiking event from VV/UP event one has more returns with larger RCS values,
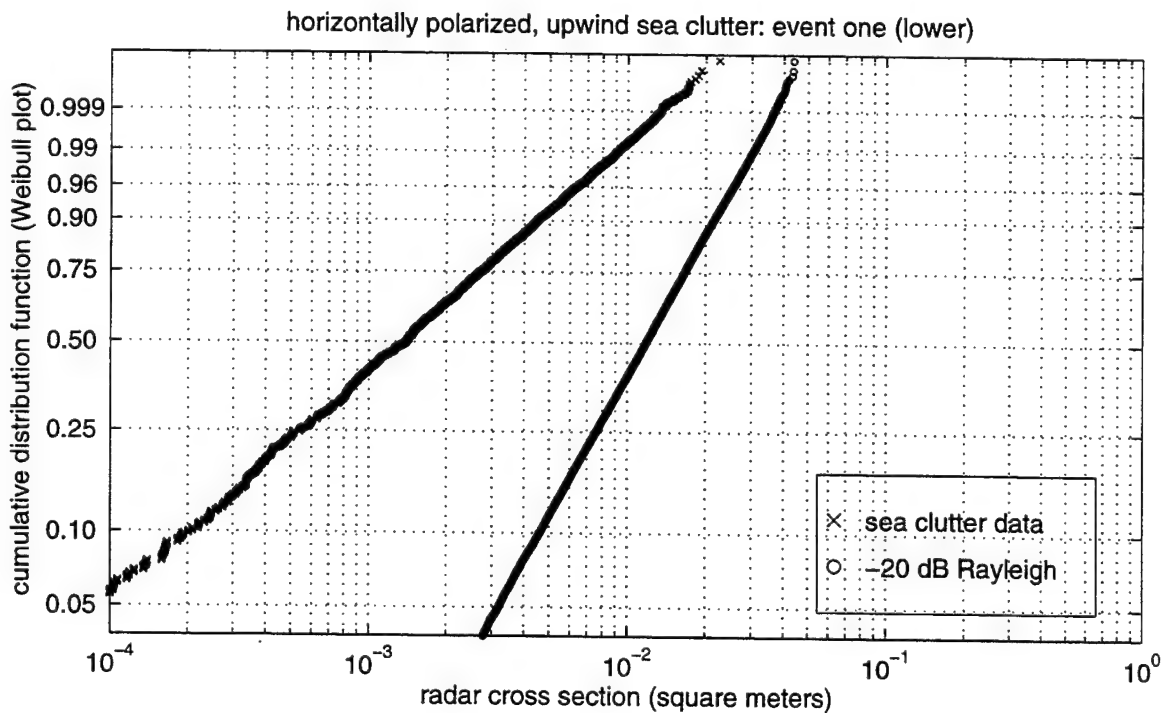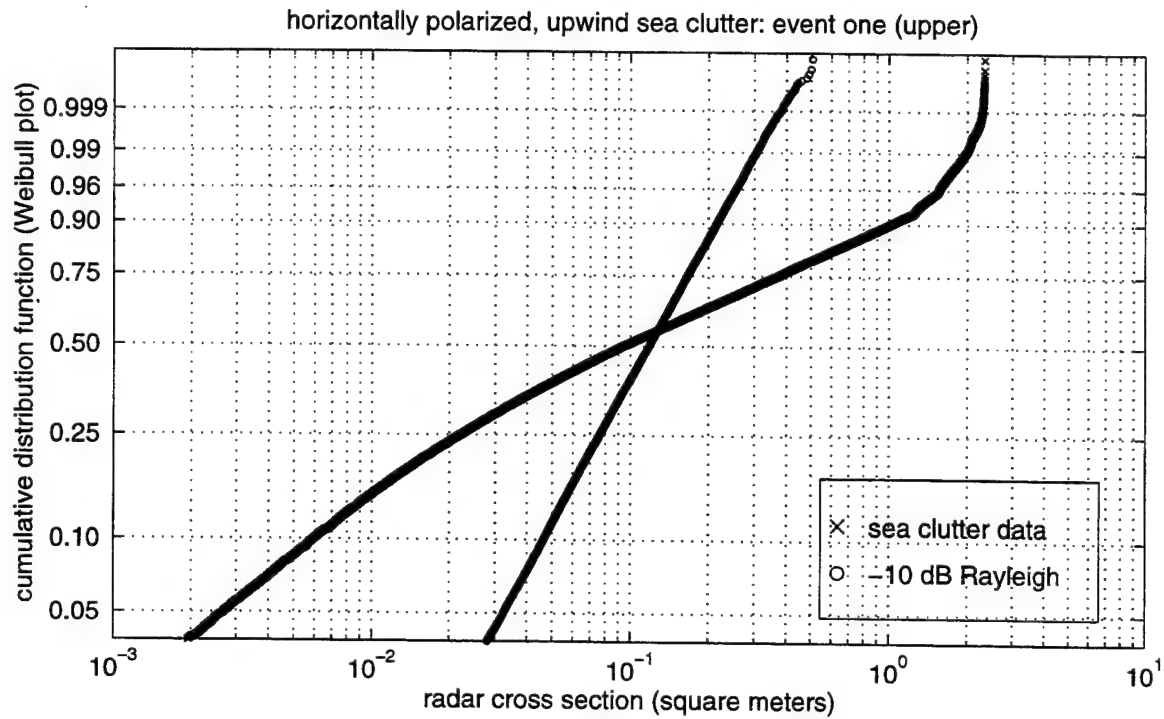
24

Figure 11: CDFs (Weibull plots) of the data within the large magnitude parallelogram (above) and the small magnitude rectangle (below), excerpted from event one, illustrating HH/UP sea clutter.
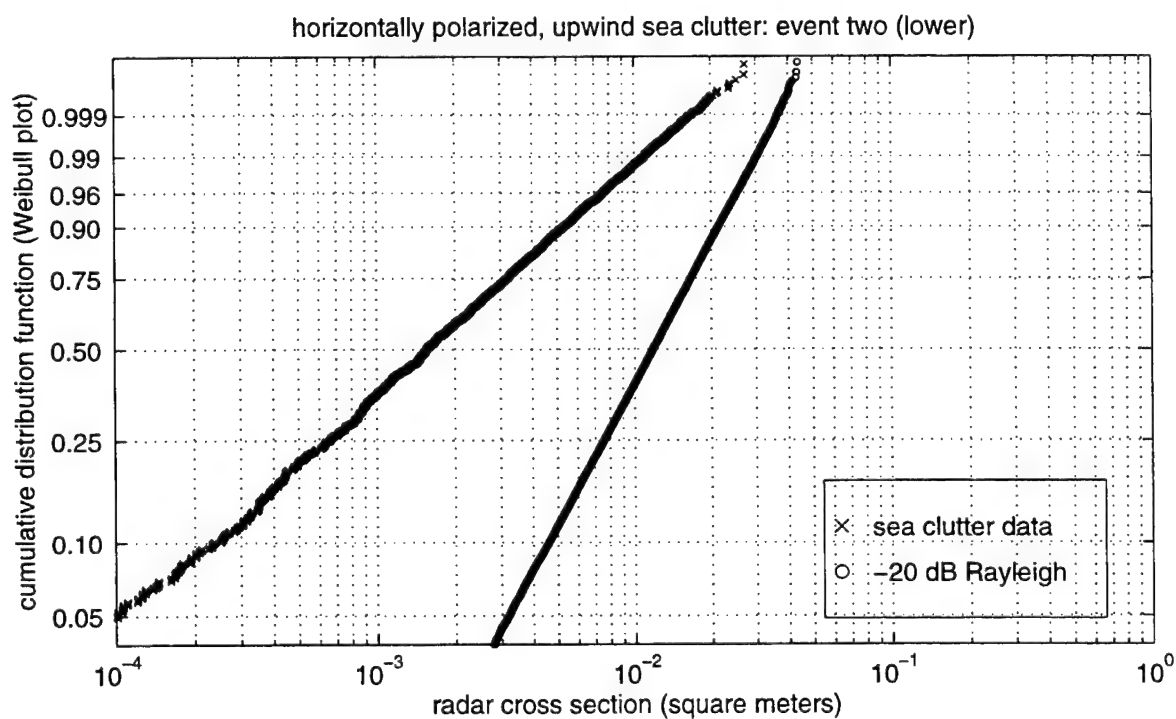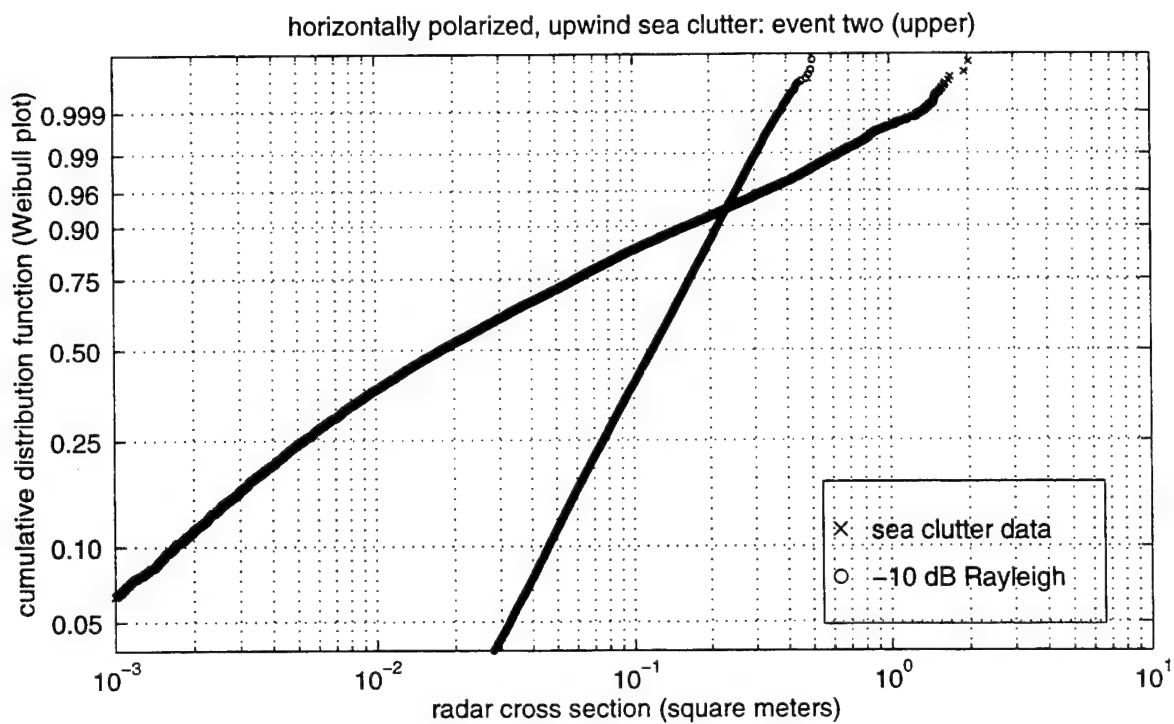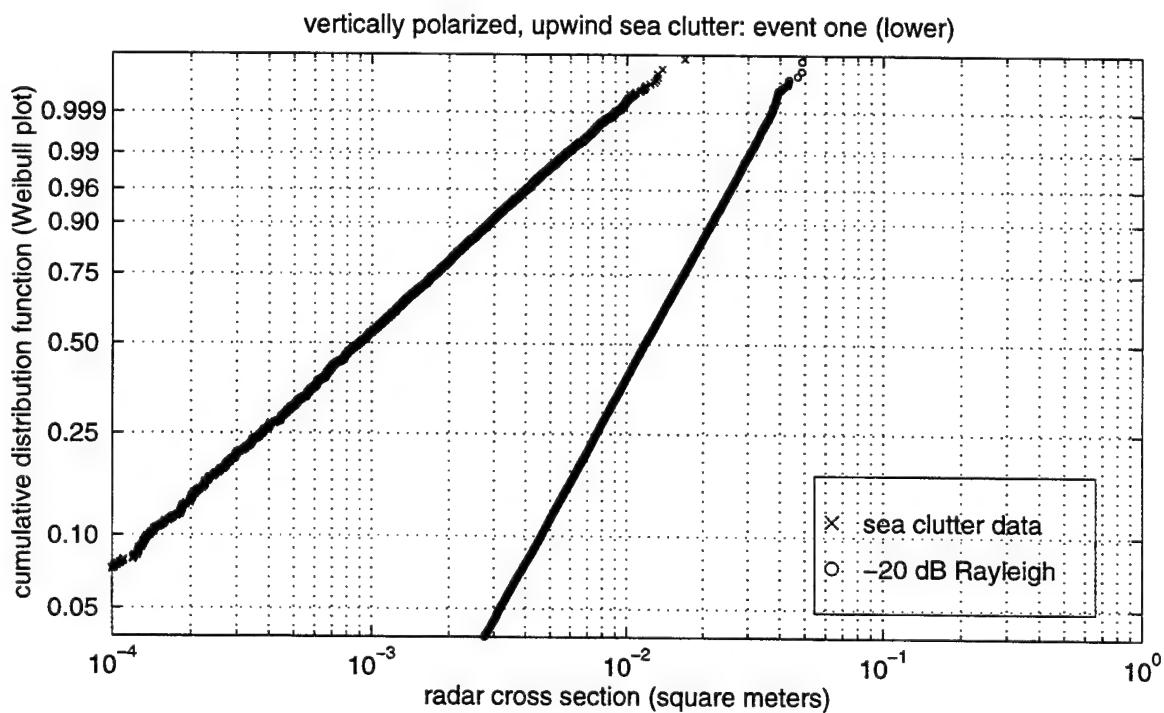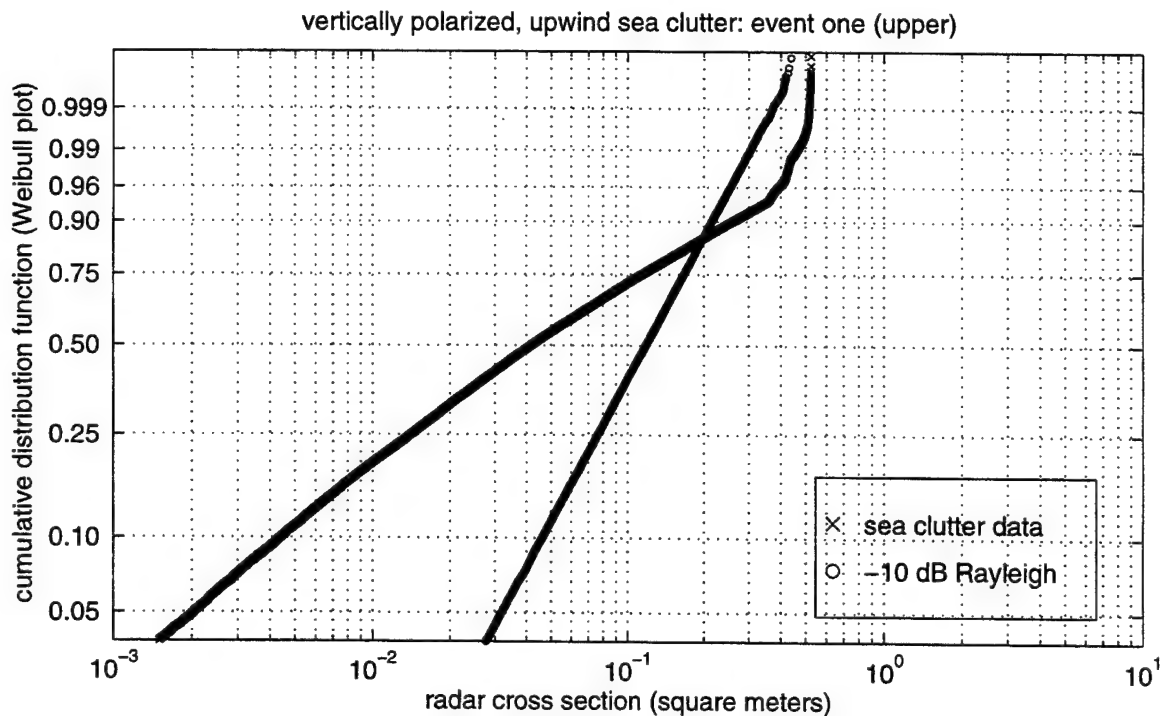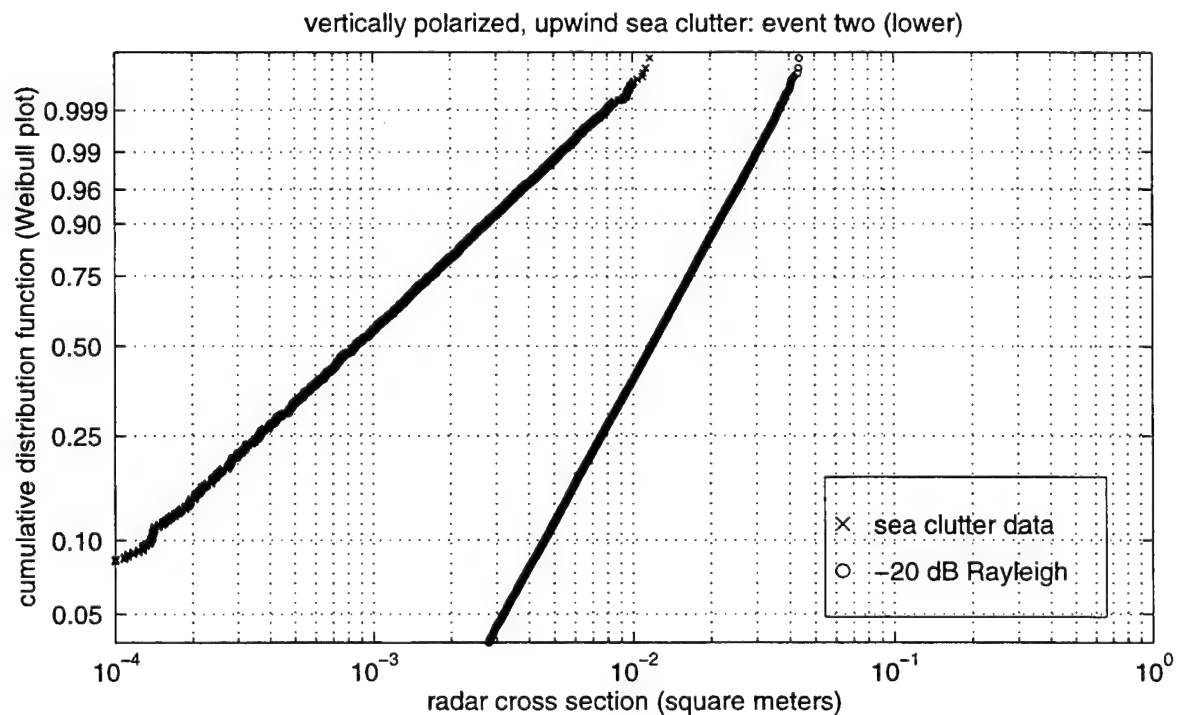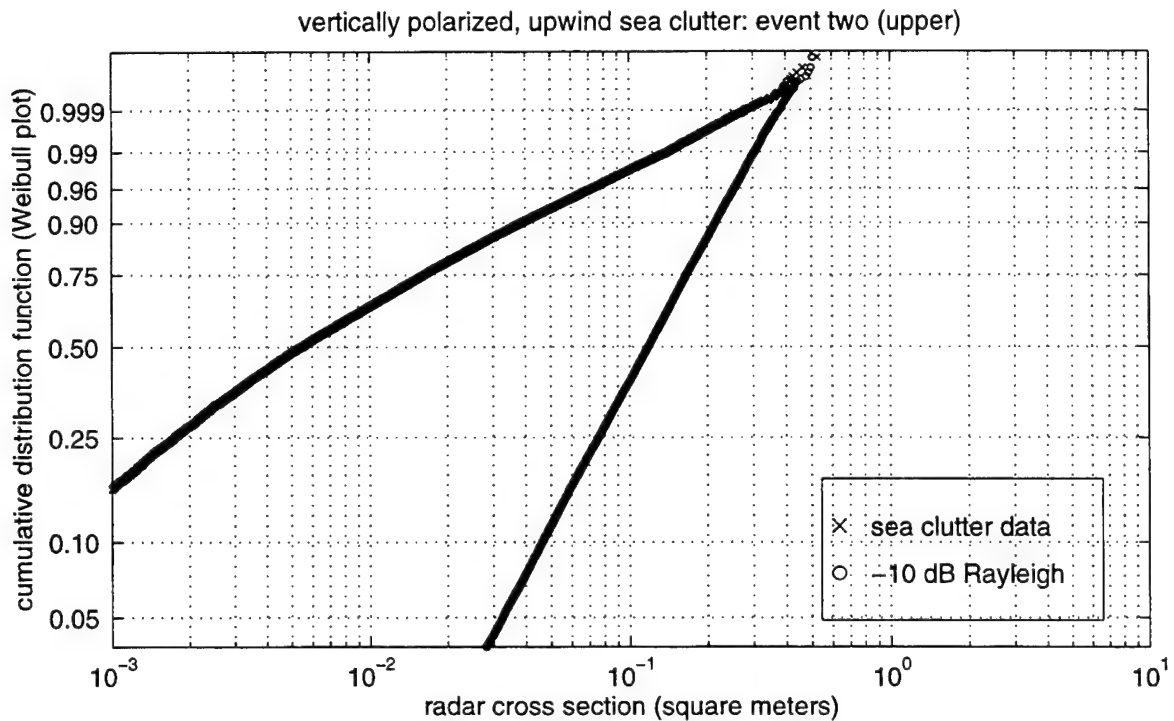
25

Figure 12: CDFs (Weibull plots) of the data within the large magnitude parallelogram (above) and the small magnitude rectangle (below), excerpted from event two, illustrating HH/UP sea clutter.

26

Figure 13: CDFs (Weibull plots) of the data within the large magnitude parallelogram (above) and the small magnitude rectangle (below), excerpted from event one, illustrating VV/UP sea clutter.

27

Figure 14: CDFs (Weibull plots) of the data within the large magnitude parallelogram (above) and the small magnitude rectangle (below), excerpted from event two, illustrating VV/UP sea clutter.

28

and the clipping is much more conspicuous. Neither of the VV/UP individual spiking events is Rayleigh-distributed. In the critical spiking range between -10 dBsm and 0 dBsm, which is somewhat truncated at the upper end by the lower onset of clipping, the CDFs of these two individual spiking events subtly depart from being straight, and thus from being Weibull-distributed, and subtly differ between themselves, with the CDF from VV/UP event one being slightly convex upwards, and the CDF from VV/UP event two being slightly concave upwards. Once again, there are strong similarities between the individual spiking events from HH/UP event one and VV/UP event one, and between the individual spiking events from HH/UP event two and VV/UP event two.

The lower CDFs, those at the bottoms of Figures 11, 12, 13, and 14, are of data contained in the small magnitude rectangles within the four different UP sea clutter events occurring over intermediate time scales and partial range swaths. These regions were deliberately selected to contain data with smaller RCS amplitudes and which one would expect to be dominated by various forms of noise, such as receiver noise and quantization noise. At very low grazing angles, one would certainly expect to find suitably shadowed regions of the sea surface from which the radar returns are dominated by noise. In fact, one way of estimating a reasonable figure for the effective noise floor of the radar is by taking the 50th percentile from these noise-dominated CDFs. During the particular data collection run from which the HH/UP examples were taken, the noise level was on the order of -28 dBsm. During the particular data collection run from which the VV/UP examples were taken, the noise level was on the order of -31 dBsm.

The CDFs of these regions, hypothesized to be noise-dominated, do indeed plot as straight lines, implying that the data within these regions are Weibull-distributed. However, they do not have quite the same slope as samples from a Rayleigh distribution, and it is a well-known fact that pure receiver noise is Rayleigh-distributed. (See Posner [Posn 93].) The explanation for the departure of these data from being Rayleigh-distributed is, at the same time, the explanation for the roughness that is noticeable at the lower left portions of all of these CDFs.

These roughnesses in the noise CDFs are due to the small biases that are left over in the data after the necessary precalibration processing. In practice, such biases can never be completely eliminated because the biases are not fixed, but rather vary during the course of the data collection. This, in turn, renders it necessary to estimate the biases for each extended sample of data from the data itself. And if the data covers a wide dynamic range, as the above examples clearly do, containing both large magnitude parallelograms and small magnitude rectangles, then the bias estimation process is rendered less accurate. The remaining presence of small biases after precalibration processing will not have a noticeable effect upon data at the upper end of the amplitude distribution, but will only have an observable effect at the lower, noise-dominated, end.

The problem of compensating for biases in the data is exacerbated by the fact that there is not just one bias for each of the I and Q channels, but rather eight independent biases for each channel, arising from an every eighth range cell dependent correlation. In other words, the I channel bias and the Q channel bias for range cells numbered 1, 9, 17, etc, are different from the I channel bias and the Q channel bias for range cells numbered 2, 10, 18, etc, which are, in turn, different from the I channel bias and the Q channel bias for range cells numbered 3, 11, 19, etc, and so on, and each must therefore be estimated separately.

Examination of various HH/CR and VV/CR events, occurring over intermediate time scales and partial range swaths, yields much the same general results as were presented in this section for HH/UP and VV/UP events, occurring over intermediate time scales and partial range swaths, but the specific illustrations will be omitted for the sake of brevity.

5   Intermediate Time Scales and Single Range Cells

In this section, we will consider examples of backscatter data whose extents in time are 5 seconds, and whose extents in range are over a single range cell of 0.3 meters. To get to the scale of these examples, we have zoomed by a factor on the order of 100 in range from the examples of intermediate time scale and partial range swath data discussed in the previous section. Figures 15, 16, and 17 illustrate, in two complementary ways, the evolution over this intermediate time scale of the clutter occurring within a single range cell. For two of the examples, in Figures 15 and 16, the data are HH/UP, and for the third example, in Figure 17, the data are VV/UP.

The variation with time of the RCS is plotted at the tops of Figures 15, 16, and 17. It should be remembered that, for the HH/UP data, values of the RCS on the order of 1.26 sm or above might very well have been subjected to clipping, as is the case with VV/UP data with values of the RCS on the order of 0.35 sm or above. At the bottoms of Figures 15, 16, and 17, the temporal variation of the spectral frequency content is displayed in the following manner. The individual spectra are generated by dividing the entire time interval into consecutive, nonoverlapping windows, and determining the PSD within each window. To suppress the uninteresting but visually-distracting PSDs associated with windows containing noise-dominated data, such PSDs of course containing significant high frequency components, each PSD is then multiplied by the mean RCS within its window. (See Hansen and Cavaleri [Hans 82].) Finally, the entire sequence of RCS-weighted power spectra that span the entire time interval are displayed in a three-dimensional plot.

Because the PRF of the radar is 2000 Hz, the extent of the frequency axis in the PSD plots is from 0 to 1000 Hz. For a window containing N pulses, the power spectrum is estimated at $(N/2) + 1$ different, equally spaced points when N is even, and $(N+1)/2$ such points when N is odd. Thus, for a 50 millisecond window with 100 pulses, the spectrum is estimated at 51 different points evenly spread over the 1000 Hz frequency axis, while for a 25 millisecond window with 50 pulses, the spectrum is estimated at 26 such points.

For HH/UP example one, which appears in Figure 15, the individual power spectra are determined with a 50 millisecond, 100 pulse window. For HH/UP example two, which appears in Figure 16, the individual power spectra are determined with a 25 millisecond, 50 pulse window. For VV/UP example one, which appears in Figure 17, the individual power spectra are determined with a 50 millisecond, 100 pulse window. Since all three examples consist of 5 seconds of data, with 10000 pulses, there are 100 individual RCS-weighted power spectra in Figures 15 and 17, and 200 individual RCS-weighted power spectra in Figure 16.

For HH/UP example one, the PSD plot at the bottom of Figure 15 calls attention, with its conspicuous high frequency spectral content, to the regions of very strong returns near 1.5 and 2.5 seconds, while ignoring, because of the RCS-weighting effect, the smaller returns, such as those near 0.5 seconds, along with the noise, that can be found in the

horizontally polarized, upwind sea clutter: example one
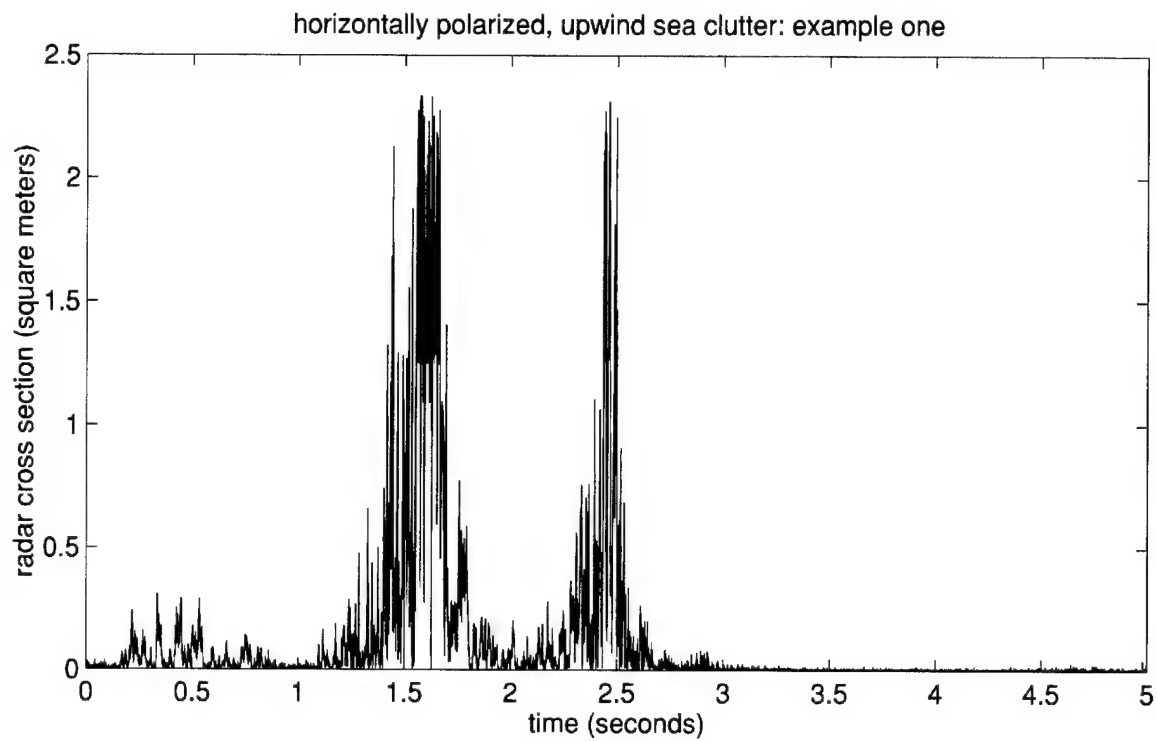
horizontally polarized, upwind sea clutter: example one, observed with 50 millisecond window
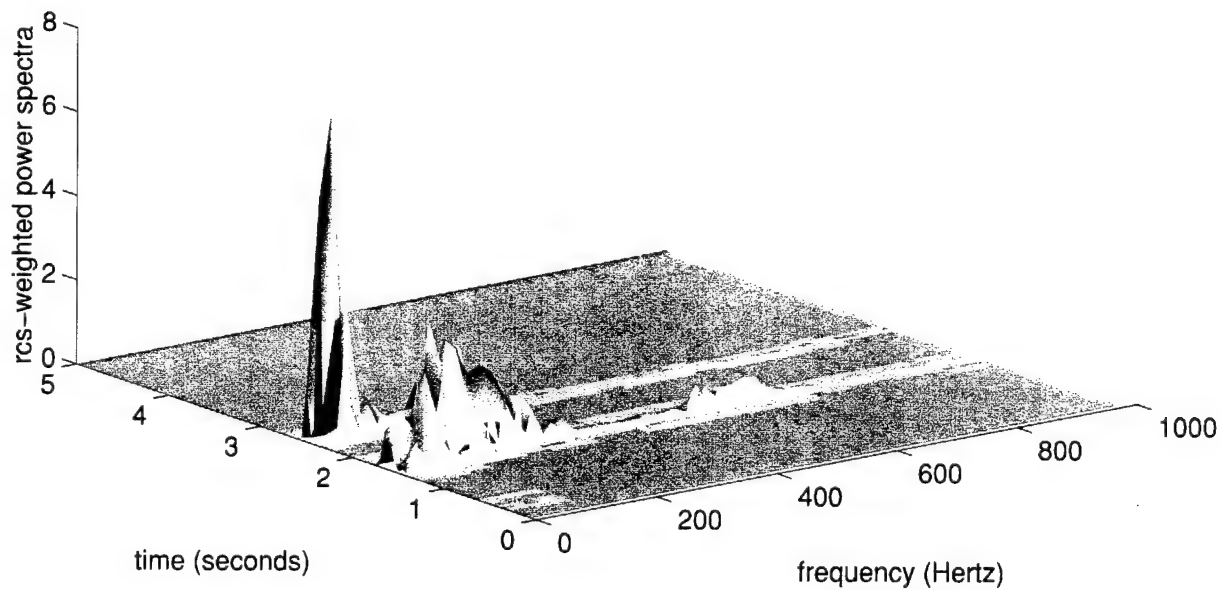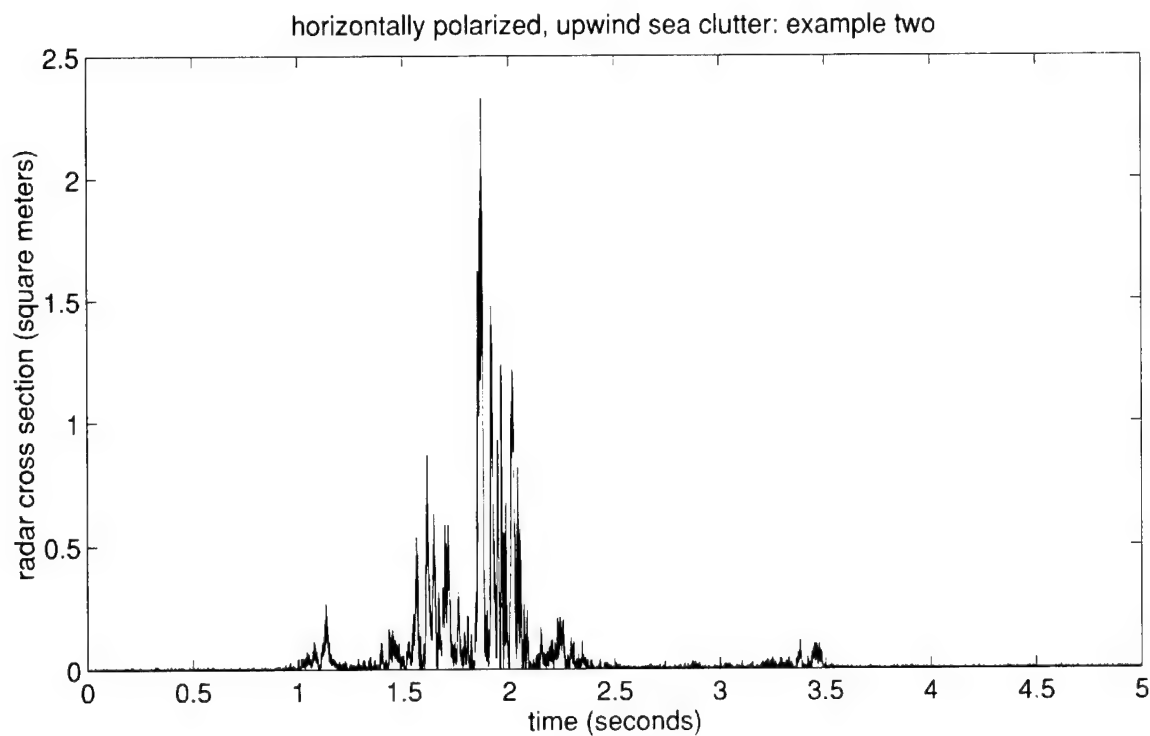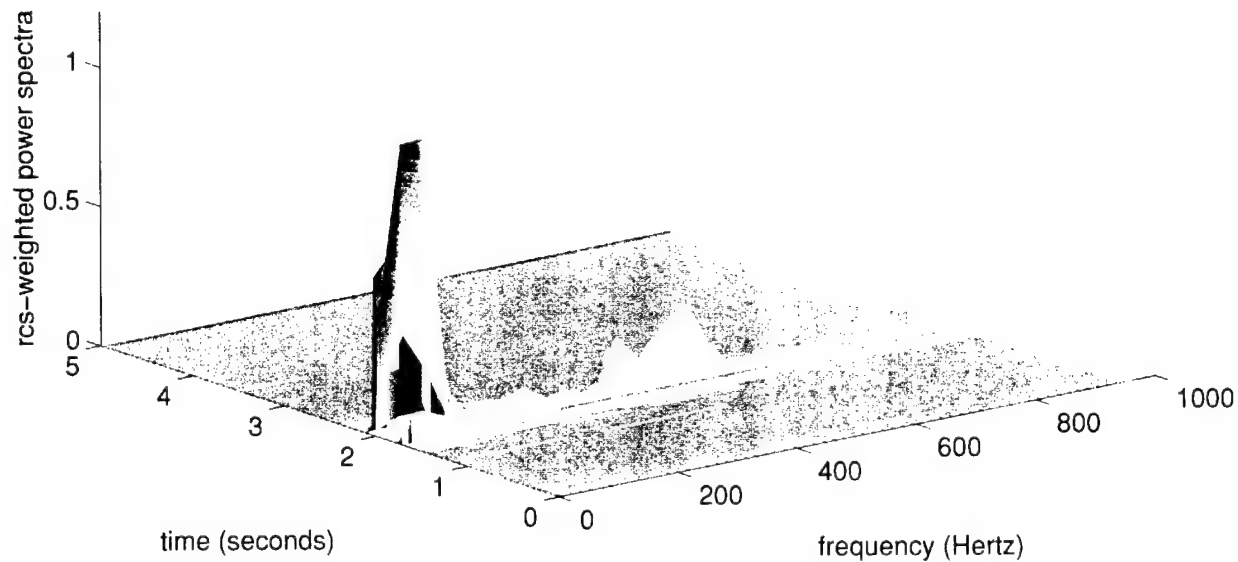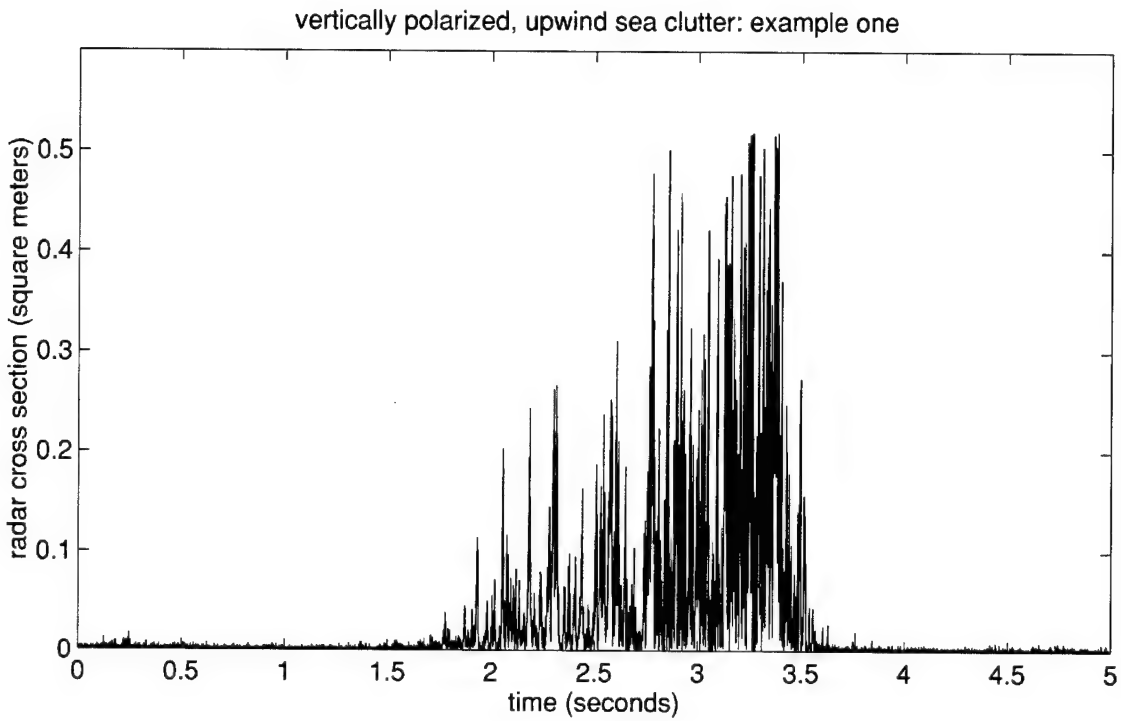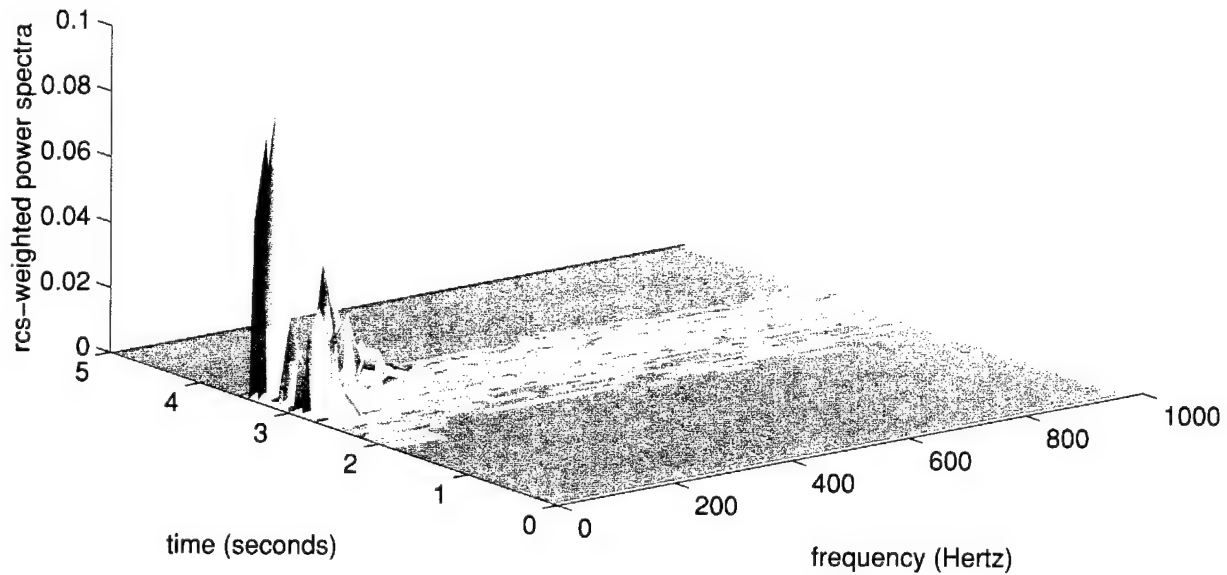

Figure 15: RCS (above), in sm, and weighted, by mean RCS over observation window, power spectra (below), for example one, illustrating HH/UP sea clutter.

horizontally polarized, upwind sea clutter: example two

horizontally polarized, upwind sea clutter: example two, observed with 25 millisecond window

Figure 16: RCS (above), in sm, and weighted, by mean RCS over observation window, power spectra (below), for example two, illustrating HH/UP sea clutter.

Figure 17: RCS (above), in sm, and weighted, by mean RCS over observation window, power spectra (below), for example one, illustrating VV/UP sea clutter.

RCS plot at the top of Figure 15. For HH/UP example two, the PSD plot at the bottom of Figure 16 calls attention, with its conspicuous high frequency spectral content, to the regions of very strong returns near 1.5 and 2 seconds, while ignoring, because of the RCS-weighting effect, the smaller returns, such as those near 1 second, along with the noise, that can be found in the RCS plot at the top of Figure 16.

For VV/UP example one, the PSD plot at the bottom of Figure 17 calls attention, with its rather less conspicuous high frequency spectral content, to the regions of very strong returns between 2 and 3.5 seconds, while ignoring the smaller returns, along with the noise, that can be found in the RCS plot at the top of Figure 17. Although the PSD plot for VV/UP example one, at the bottom of Figure 17, is one of the most striking examples that can be found amongst such plots for VV data, it is still rather undramatic in comparison with corresponding plots for HH data, such as the PSD plots for HH/UP examples one and two, at the tops of Figures 15 and 16. And consistently with what was observed in the two previous sections, one observes here, on comparison of the RCS plots at the tops of Figures 15, 16, and 17, that the HH clutter is spikier and more intermittent than the VV clutter.

Since the spectral estimation process is fairly sensitive to both the size and the placement of the data window, and since the RCS-weighting can suppress real but weaker events, it is clear that these three-dimensional PSD plots are to be used by the analyst as useful, but by no means complete, indicators of where, in an overwhelming amount of data, to look for interesting clutter phenomenology. From HH/UP example one, at the bottom of Figure 15, the major outcropping of high frequency spectral content above 500 Hz, near 1.5 seconds, and from HH/UP example two, at the bottom of Figure 16, the major outcropping of high frequency spectral content above 300 Hz, near 2 seconds, as well as the isolated high frequency spectral peak at 500 Hz, near 1.5 seconds, we have three specific instances of HH/UP short time scale clutter that will be investigated at the beginning of the next section. In addition, from VV/UP example one, at the bottom of Figure 17, the low-lying spectral ridges, between 2 and 3.5 seconds, will guide us to a specific instance of VV/UP short time scale clutter that will be investigated later on in the next section.

6 Short Time Scales and Single Range Cells

In this section, beginning with the three examples of HH/UP short time scale clutter discussed at the end of the previous section, we will consider examples of backscatter data whose extents in time are mostly either 50, or in a few cases, 25 milliseconds, and whose extents in range are over a single range cell of 0.3 meters. To get to the scale of these examples, we have zoomed by a factor on the order of 100 in time from the examples of intermediate time scale and single range cell data discussed in the previous section. Figures 18, 19, and 20 give snapshots of the clutter within an individual range cell, with the RCS above and normalized PSD below.

The significant high frequency spectral content above 500 Hz, near 1.5 seconds, at the bottom of Figure 15, is due to the 100 pulses in the 32nd 50 millisecond window of HH/UP example one. The RCS of this data, which we will designate HH/UP example one (a), appears at the top of Figure 18, and its normalized PSD appears at the bottom of Figure 18.

34

The significant high frequency spectral content above 300 Hz, near 2 seconds, at the bottom of Figure 16, is due to the 50 pulses in the 75th 25 millisecond window of HH/UP example two. The RCS of this data, which we will designate HH/UP example two (a), appears at the top of Figure 19, and its normalized PSD appears at the bottom of Figure 19. The isolated peak at 500 Hz, near 1.5 seconds, at the bottom of Figure 16, is due to the 50 pulses in the 63rd 25 millisecond window of HH/UP example two. The RCS of this data, which we will designate HH/UP example two (b), appears at the top of Figure 20, and its normalized PSD appears at the bottom of Figure 20.

Clipping of the largest returns is a serious inconvenience for the analyst, and is an obstacle which must be gotten around, usually by analyzing samples of the data which contain fewer returns from the very upper part of the distribution. It is easy to be on the alert for clipping after examining the PDFs of events with very large magnitudes, such as those at the tops of Figures 9 and 10. On the other hand, the fact that one may not notice the clipping in the PDFs of smaller magnitude events, such as those at the bottoms of Figures 9 and 10, certainly does not guarantee that none of the data has been clipped. Indeed, the CDFs at the tops of Figures 12 and 14 do confirm that there is clipping present in these smaller magnitude events.

From earlier discussions of clipping, for these HH/UP data, values of the RCS on the order of 1.26 sm or above are suspect. With regard to HH/UP example one (a) and its snapshots in Figure 18, there certainly has been clipping of the RCS data, which, in turn, corrupts the PSD, although one can probably safely assume the presence of a significant high frequency component in the underlying data. With regard to HH/UP example two (a) and its snapshots in Figure 19, there may have been some clipping of the RCS data, and thus, there may be some corruption of the PSD, although one is inclined to credit the very powerful high frequency component in the underlying data. With regard to HH/UP example two (b) and its snapshots in Figure 20, there has been no clipping of the relatively much smaller magnitude RCS data, the PSD is uncorrupted, and one can believe the conspicuous high frequency spectral components in the data. It is not hard to see the harmonic modulation of the RCS data that gives rise to the high frequency spectral components.

The next two examples are of data that has not suffered any clipping. All of the HH/UP RCS data is safely below 1.26 sm, and all of the VV/UP RCS data is safely below 0.35 sm. Figures 21 and 22 give 50 millisecond, 100 pulse snapshots of these examples of the short time scale clutter within an individual range cell, with the RCS above and the normalized PSD below. The polarization is HH in Figure 21, and the data will be designated HH/UP example three. The polarization is VV in Figure 22, and the data, which was selected from the intermediate time scale, single range cell clutter that was analyzed in Figure 17, will be designated VV/UP example one (a).

For HH/UP example three, several modes of harmonic modulation are clearly visible in the RCS data, at the top of Figure 21, and these give rise to a PSD, at the bottom of Figure 21, with many conspicuous high frequency spectral components. For VV/UP example one (a), there are also clearly visible modulations in the RCS data, at the top of Figure 22, although these modulations differ from those in the HH/UP clutter by regularly bringing the RCS amplitude almost all the way down into the noise. Although the modulations in the VV/UP clutter do give rise to a PSD, at the bottom of Figure 22, with discernible high frequency components, these are not nearly as striking as those in the PSD of the HH/UP
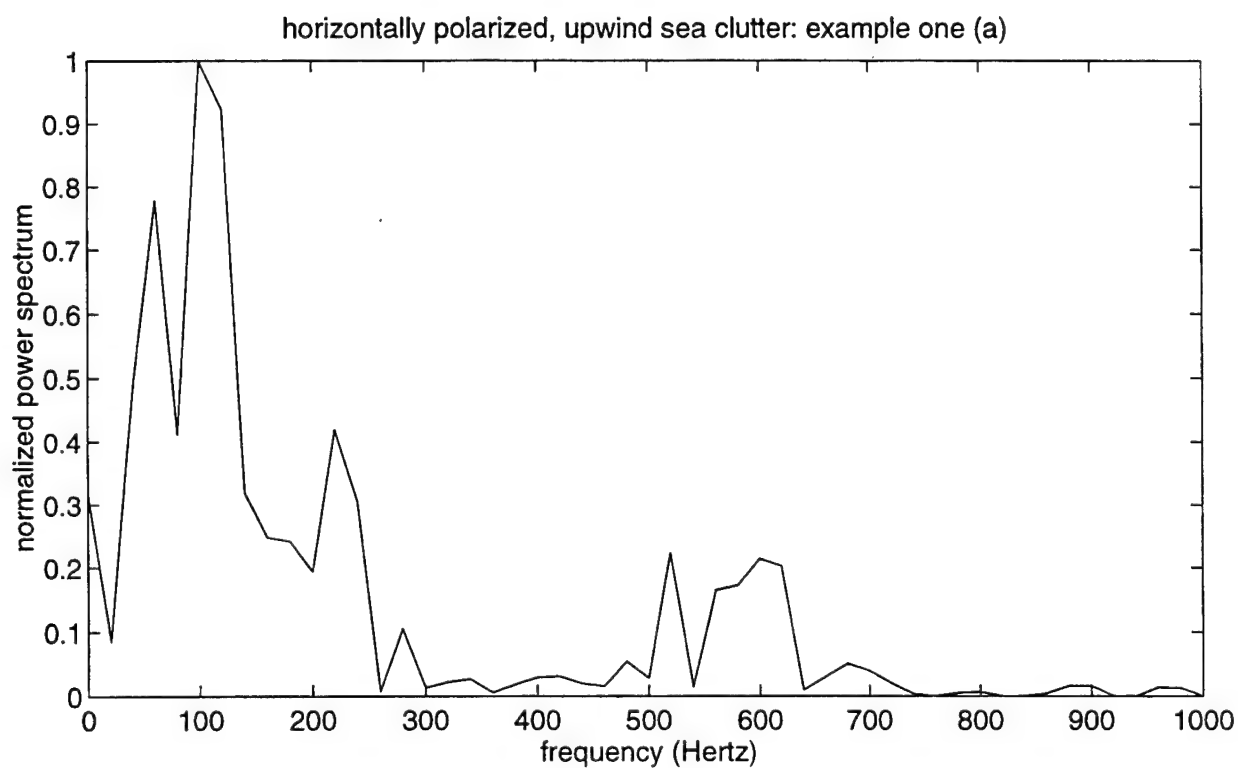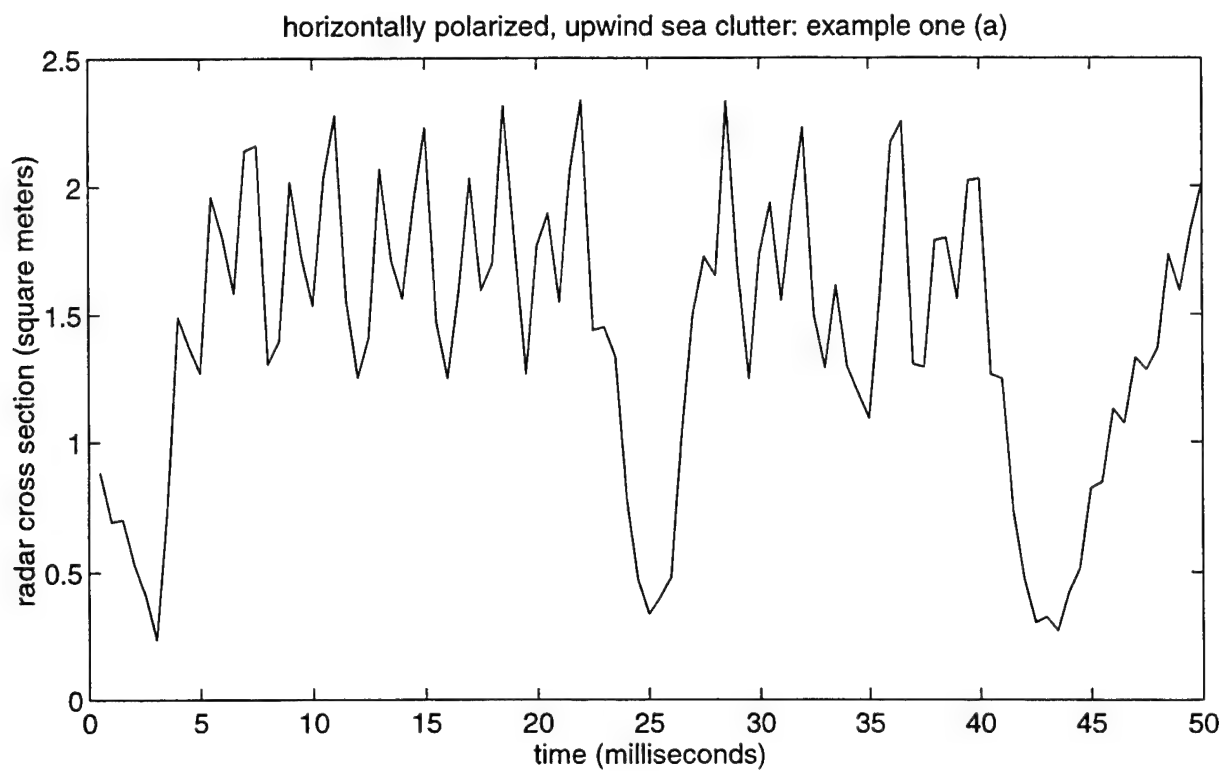
35

Figure 18: RCS (above), in sm, and normalized power spectrum (below), for example one (a), illustrating HH/UP sea clutter.
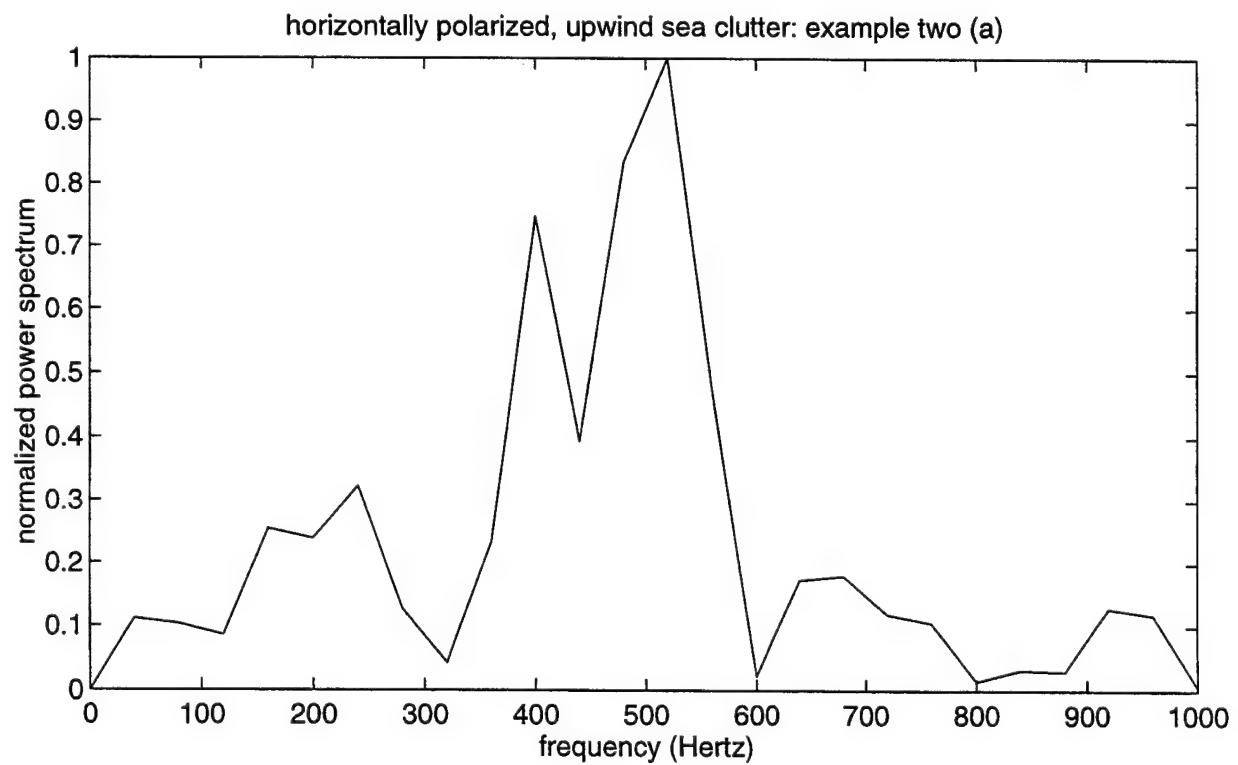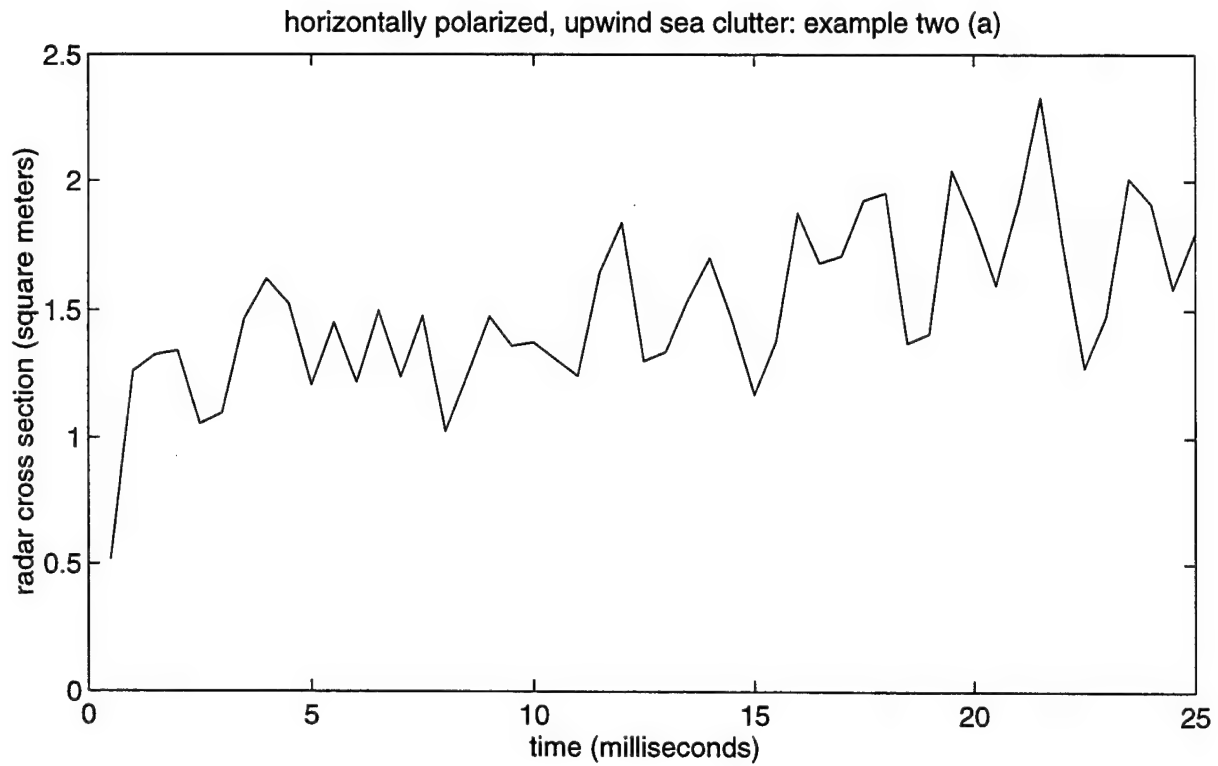
Figure 19: RCS (above), in sm, and normalized power spectrum (below), for example two (a), illustrating HH/UP sea clutter.
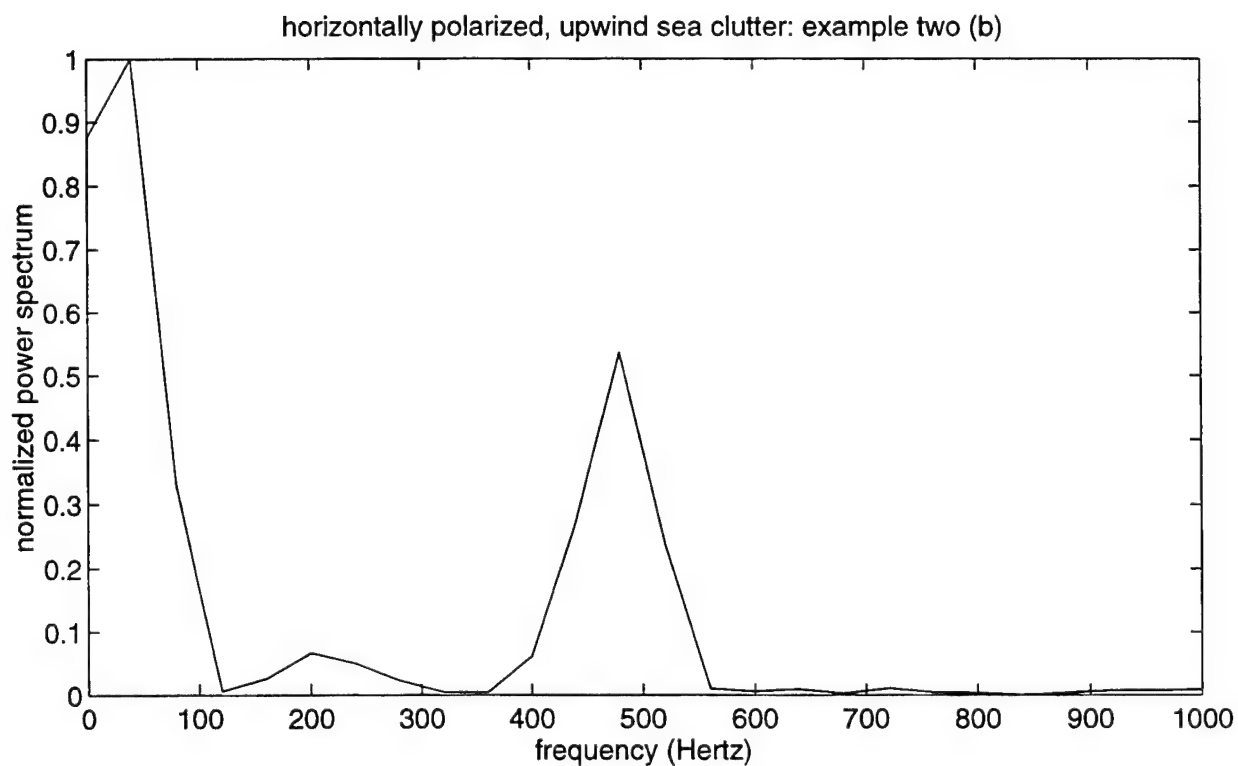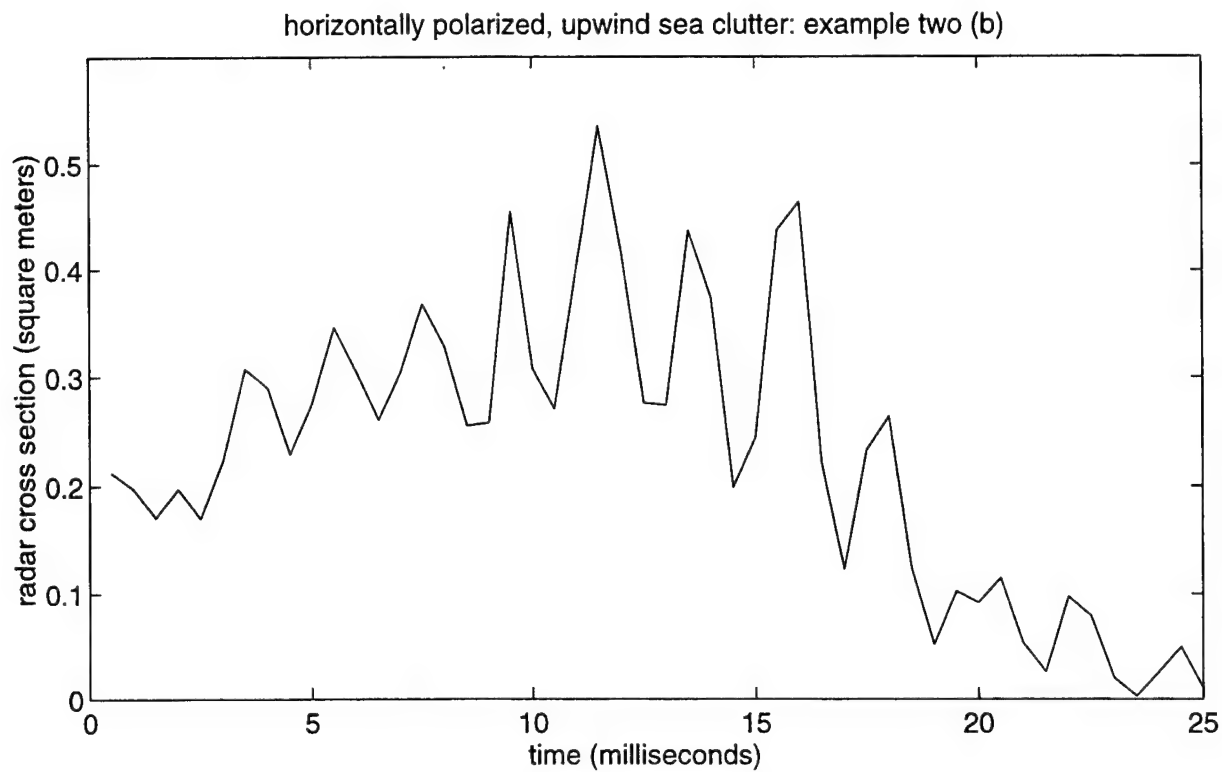
Figure 20: RCS (above), in sm, and normalized power spectrum (below), for example two (b), illustrating HH/UP sea clutter.

clutter. At this point, one should also make the observation that, on the basis of the analysis of many specific examples, there does seem to be a definite correlation between the overall magnitude of a spatially and temporally extended spiking event, and how high in frequency one will find the significant high frequency spectral components that are present in specific examples of spiky sea clutter excerpted from the event itself.

Using the same clutter data that were analyzed in Figures 21 and 22, the normalized autocorrelation function (ACF) of HH/UP example three is plotted at the top of Figure 23, and the normalized ACF of VV/UP example one (a) is plotted at the bottom of Figure 23. The HH/UP sequence decorrelates relatively slowly, its ACF only falling to a value of 0.5 after more than 20 milliseconds, while the VV/UP sequence decorrelates more rapidly, its ACF falling to a value of 0.5 after only a little more than 10 milliseconds. The decay of the HH/UP ACF is characterized by sections of lesser and greater slope, while the decay of the VV/UP ACF is distinctly less smooth and less gradual, with the sections of lesser and greater slope being replaced by actual upward and downward oscillations. This behavior, of the two ACFs in Figure 23, is caused by the meshing and unmeshing of the various segments of the original sequences of RCS data, which, in turn, were themselves dominated by the various underlying harmonic modulations indicated by the spectral components in the PSDs. This all follows from the fact that the spectral density and the autocovariance function of a stochastic process are a Fourier transform pair, and that a spectral peak at a particular frequency corresponds to an oscillation in the autocovariance function whose period is at the inverse frequency.

Examination of HH/CR RCS data reveals clearly visible harmonic modulations, which, in turn, give rise to HH/CR PSDs with significant high frequency components, and to HH/CR ACFs whose decay is relatively smooth and gradual. In other words, RCS, PSD, and ACF plots of HH/CR data exhibit the same major qualitative features that are seen in RCS, PSD, and ACF plots of HH/UP data. The main difference between these two types of HH data resides in the fact that, on the one hand, it was comparatively easy to find examples of HH/UP data which, upon analysis, clearly exhibited these features common to both types of HH data, features that other researchers, to be discussed in the next section, as well as the present author, have found to be characteristic of spiky sea clutter at low grazing angles and high range resolutions. On the other hand, it was considerably less easy to find examples of HH/CR data which, upon analysis, clearly exhibited these same features. One is forced to conclude that, whatever the underlying physical processes are which yield these analytical results that are typical of HH sea spikes at low grazing angles and high range resolutions, they are easier to observe when the transmit geometry of the radar is UP rather than CR.

Examination of VV/CR RCS data reveals clearly visible harmonic modulations, very similar to those seen with VV/UP RCS data, which regularly bring the amplitude almost all the way down into the noise, and thus clearly differ from those observed in both HH/UP and HH/CR RCS data. These modulations, in turn, give rise to significant high frequency components in the VV/CR PSDs, very similar to those seen in VV/UP PSDs, but which are nowhere near as striking as those observed in HH/UP and HH/CR PSDs. And these modulations also give rise to VV/CR ACFs, which are very similar to VV/UP ACFs, but whose decays are noticeably less smooth and less gradual than those of HH/UP and HH/CR ACFs.

Much as was the case with the two types, UP and CR, of HH data, RCS, PSD, and
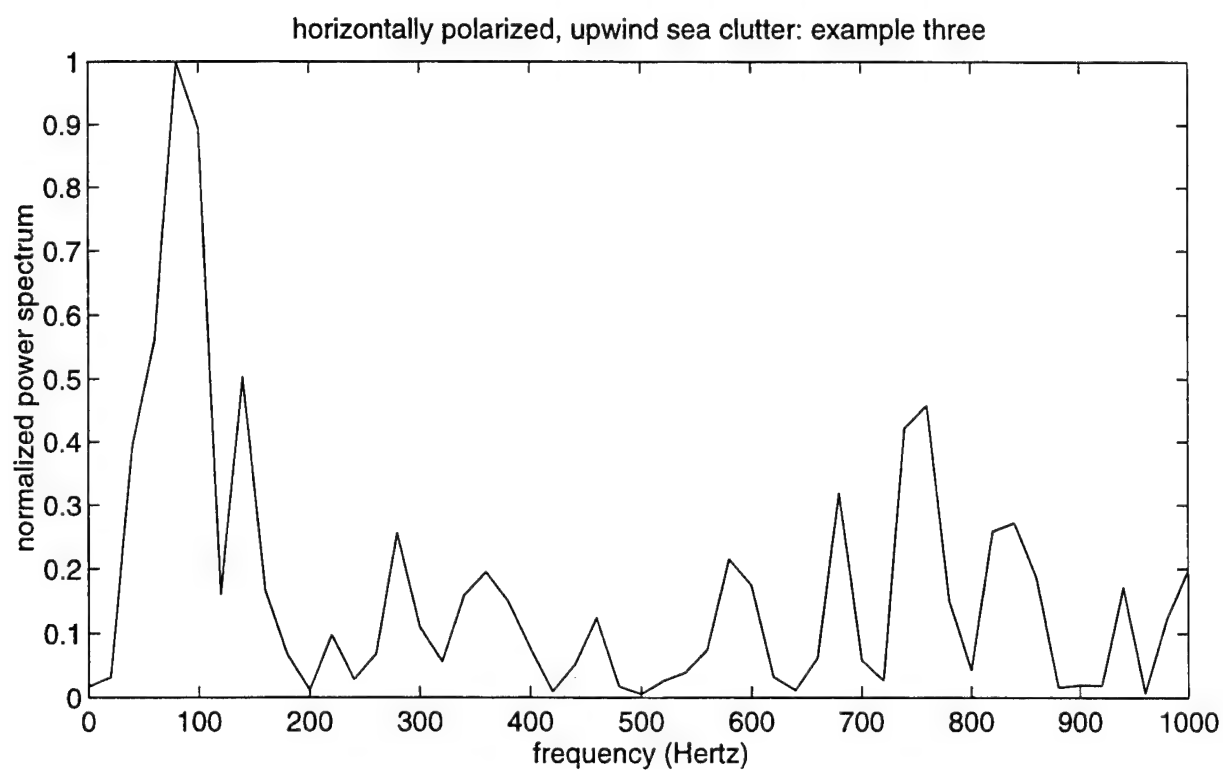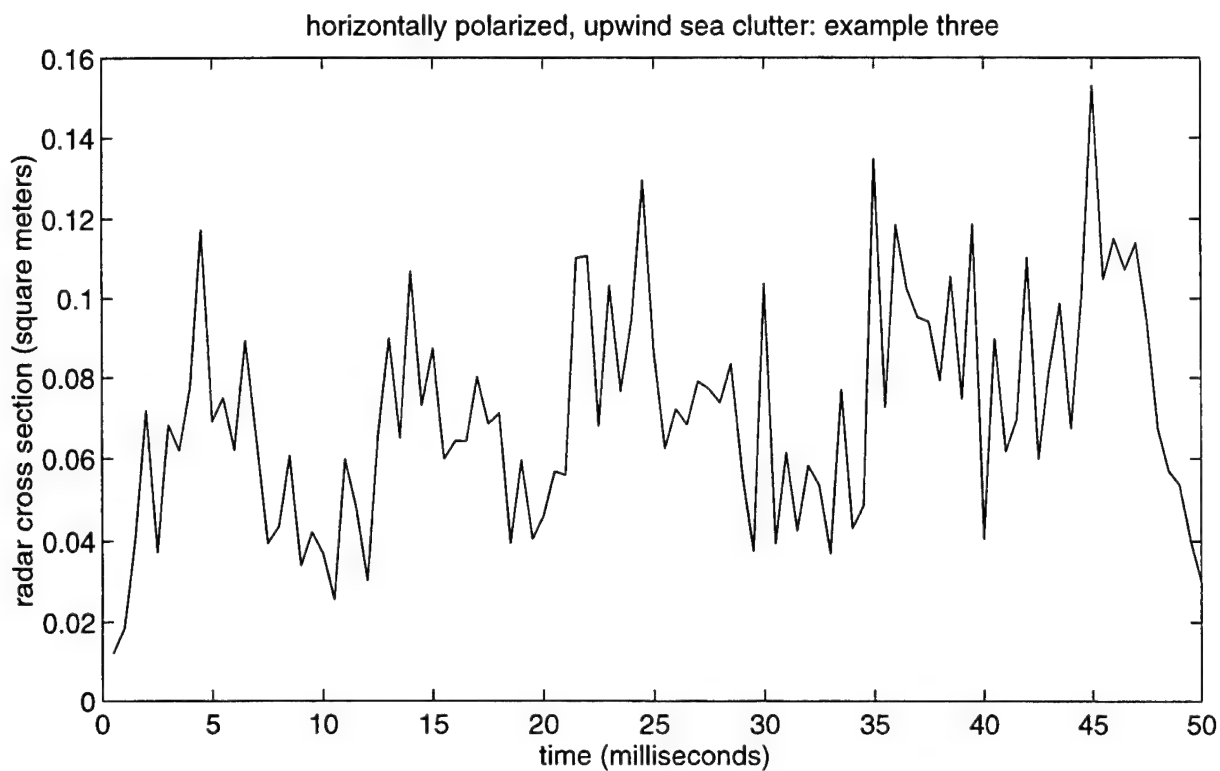
39

Figure 21: RCS (above), in sm, and normalized power spectrum (below), for example three, illustrating HH/UP sea clutter.
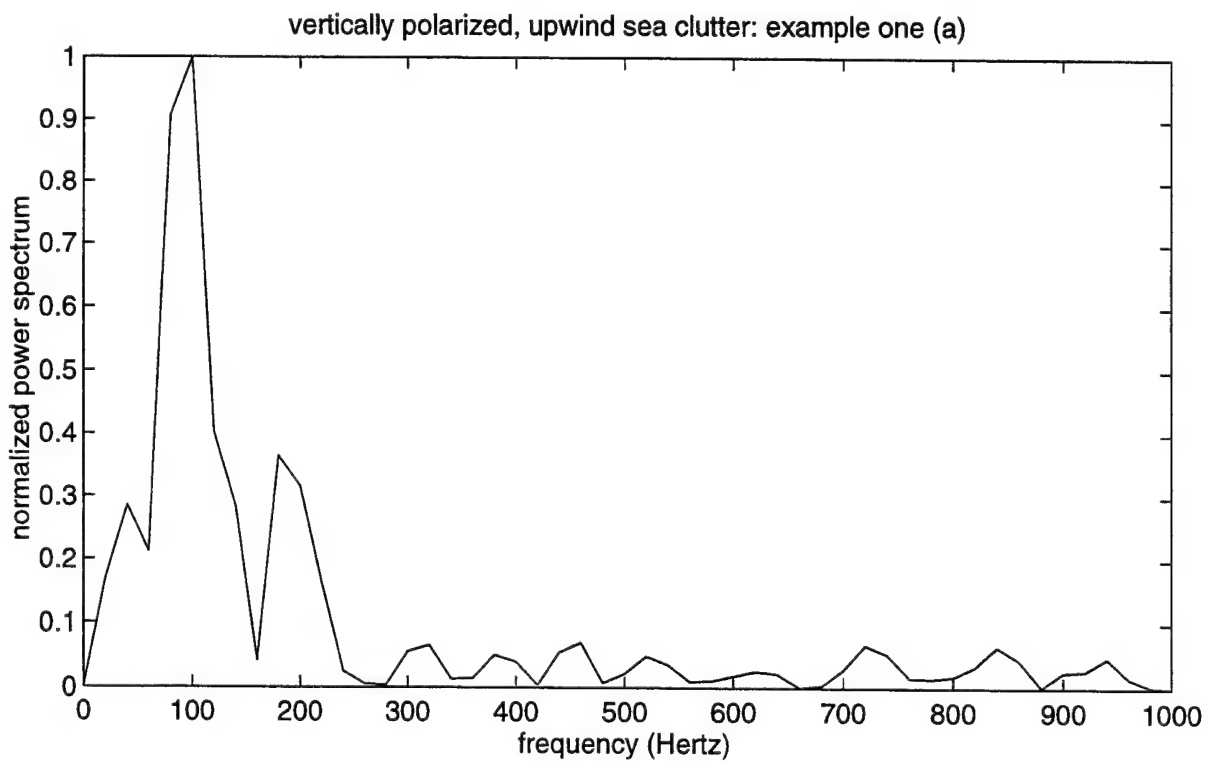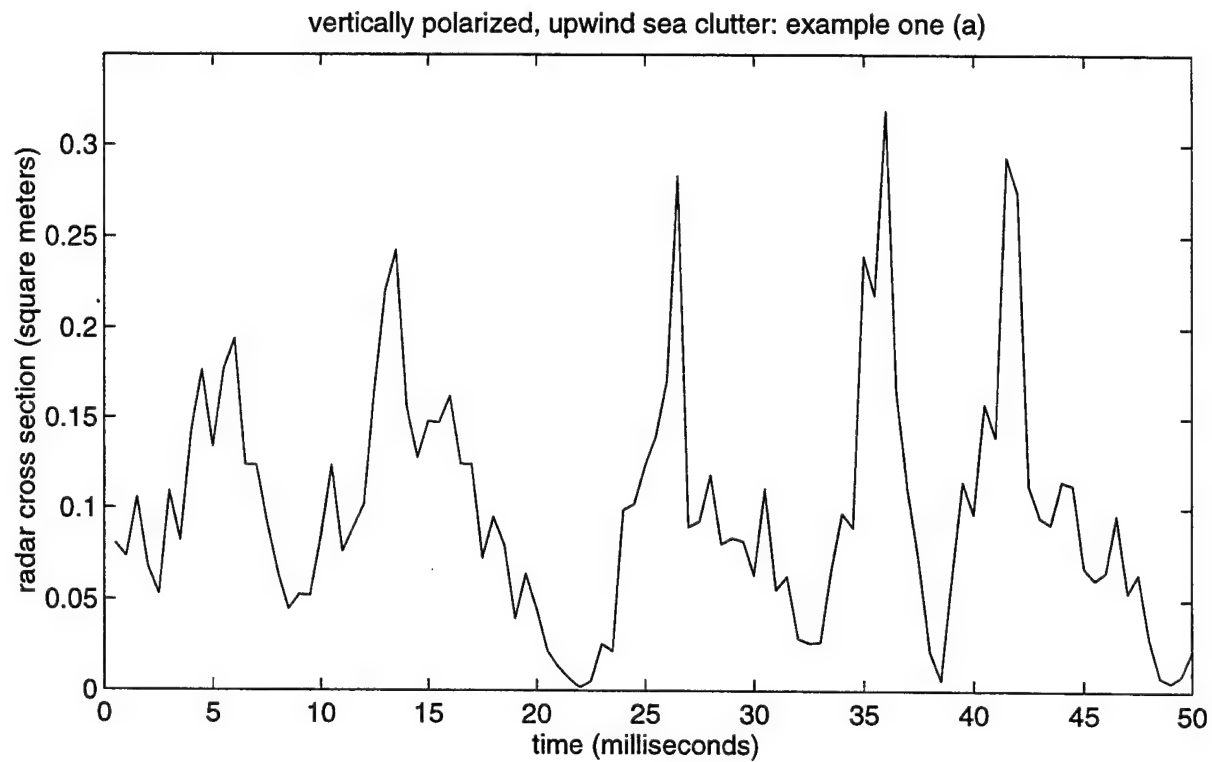
Figure 22: RCS (above), in sm, and normalized power spectrum (below), for example one (a), illustrating VV/UP sea clutter.
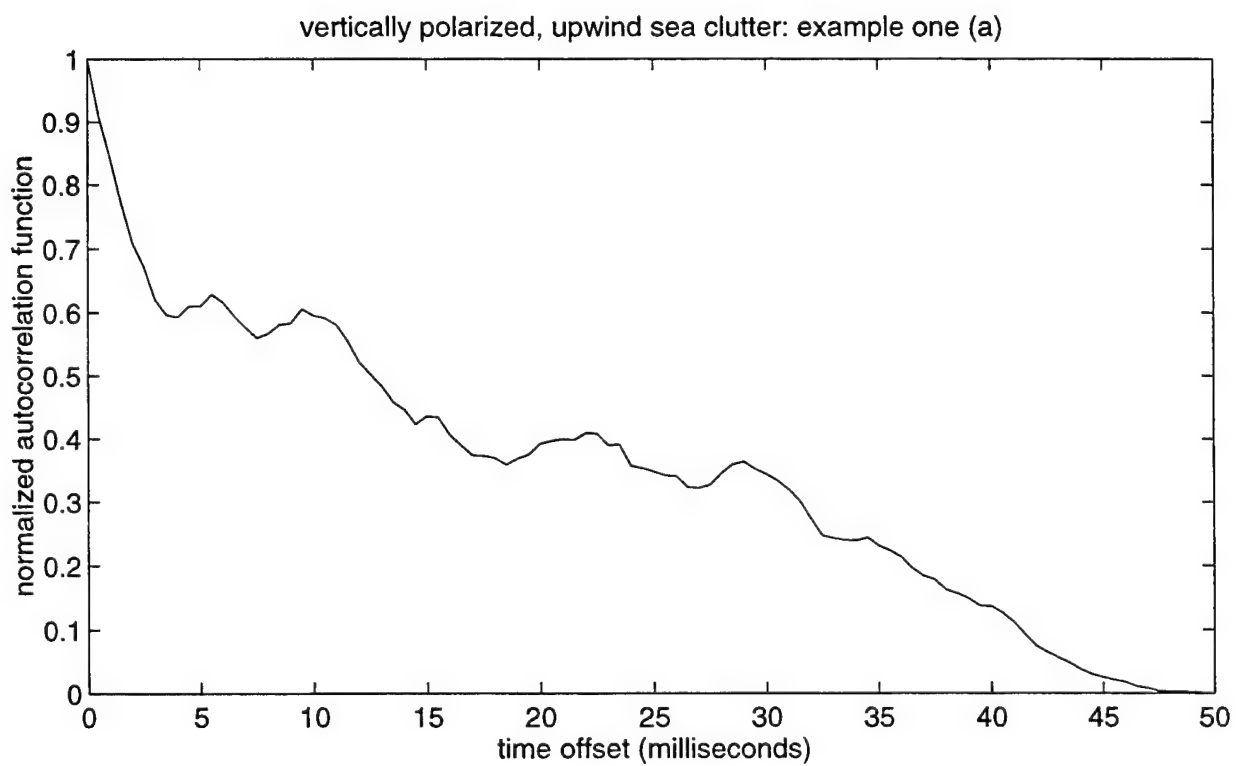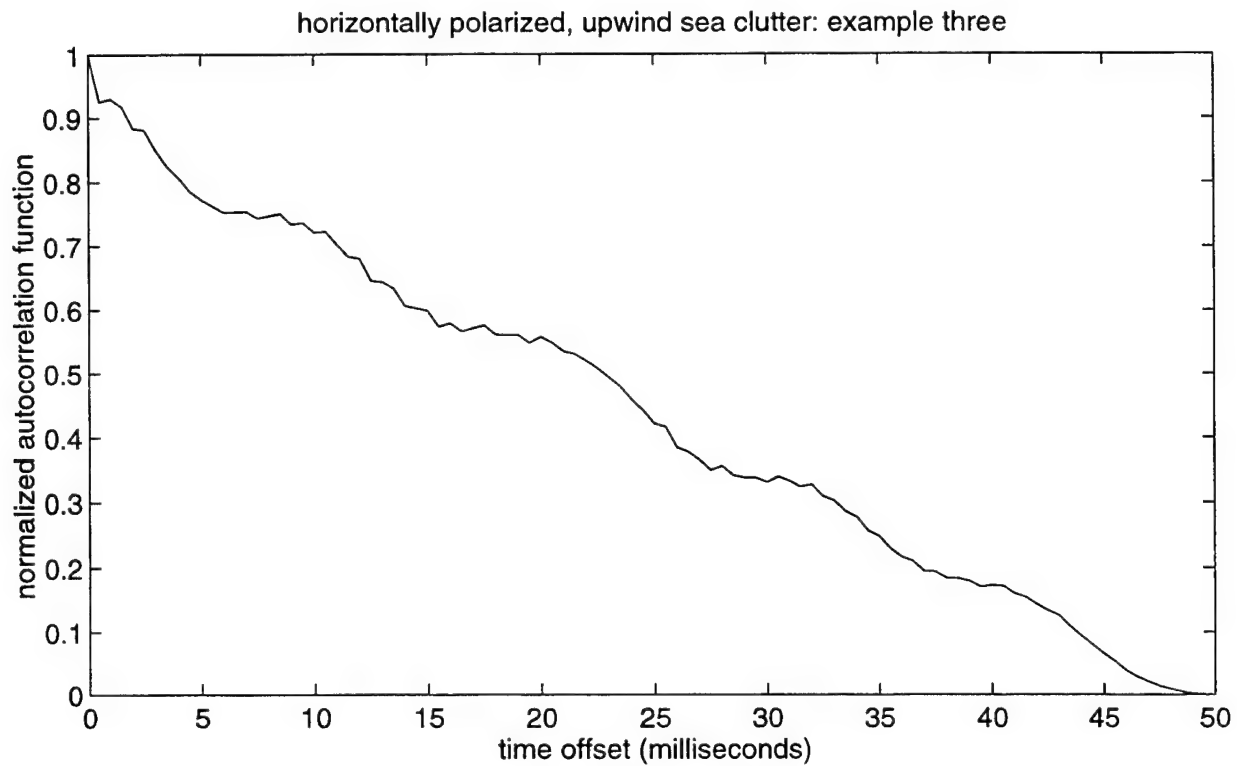
Figure 23: Normalized ACF for example three, illustrating HH/UP sea clutter (above), and example one (a), illustrating VV/UP sea clutter (below).

ACF plots of VV/CR data exhibit the same major qualitative features that are seen in RCS, PSD, and ACF plots of VV/UP data. However, RCS, PSD, and ACF plots of VV data, both UP and CR, exhibit marked qualitative differences from RCS, PSD, and ACF plots of HH data, both UP and CR. The main difference between data of different polarizations resides in the fact that, on the one hand, it was relatively easy to find examples of HH/UP data which, upon analysis, clearly exhibited these significant qualitative features, features that other researchers, to be discussed in the next section, as well as the present author, have found to be characteristic of spiky sea clutter at low grazing angles and high range resolutions, either HH or VV. On the other hand, it was distinctly less easy to find examples of VV data, either UP or CR, which, upon analysis, clearly exhibited these same features, at least to some degree. One is forced to conclude that, whatever the underlying physical processes are which yield these various qualitative and quantitative results that are typical of sea spikes at low grazing angles and high range resolutions, they are easiest to observe when the polarization of the radar is HH rather than VV.

After concentrating on analyses that pointed up the differences between HH and VV clutter, we will now present analyses that produce fairly similar results from HH and VV clutter. Using the same clutter data that were analyzed in Figures 21, 22, and 23, Figure 24 presents, at the top, the phase and, at the bottom, the change in phase of HH/UP example three, while Figure 25 presents, at the top, the phase and, at the bottom, the change in phase of VV/UP example one (a). For HH/UP example three, in Figure 24, there is a quite smooth decrease in phase over the observation window, with only small fluctuations about a mean pulse-to-pulse phase change of -0.256π radians. For VV/UP example one (a), in Figure 25, there is a somewhat less smooth decrease in phase over the observation window, with only small, for the most part, fluctuations about a mean pulse-to-pulse phase change of -0.143π radians.

For a 2000 Hz PRF radar, a constant pulse-to-pulse phase change of -0.256π radians, as with HH/UP example three, gives a Doppler frequency of -256 Hz. This, in turn, for a nominal radar operating frequency of 9.75 GHz, corresponds to a closing range rate of 3.9 meters per second. On the other hand, a constant pulse-to-pulse phase change of -0.143π radians, as with VV/UP example one (a), gives a Doppler frequency of -143 Hz, which, in turn, corresponds to a closing range rate of 2.2 meters per second.

With regard to these Doppler frequencies, it should be noted that, for HH/UP example three, in the PSD plot at the bottom of Figure 21, there are significant spectral components above 250 Hz, and for VV/UP example one (a), in the PSD plot at the bottom of Figure 22, there are significant spectral components above 150 Hz. Indeed, the average spectral frequency for HH/UP example three is 398 Hz, which, in turn, corresponds to a closing range rate of 6.1 meters per second, and the average spectral frequency for VV/UP example one (a) is 210 Hz, which, in turn, corresponds to a closing range rate of 3.2 meters per second.

With regard to the range rates associated with the Doppler frequencies determined above from observed changes in phase, it should be noted that both are somewhat smaller than the speeds of 4.8 meters per second, associated with the propagation of microwave-reflective phenomena, that were observed in the RTI plots in an earlier section. This might be an indication that the range rates derived from the phase plots in this section are associated with incoming waves, while the propagating large magnitude returns in the RTI plots are
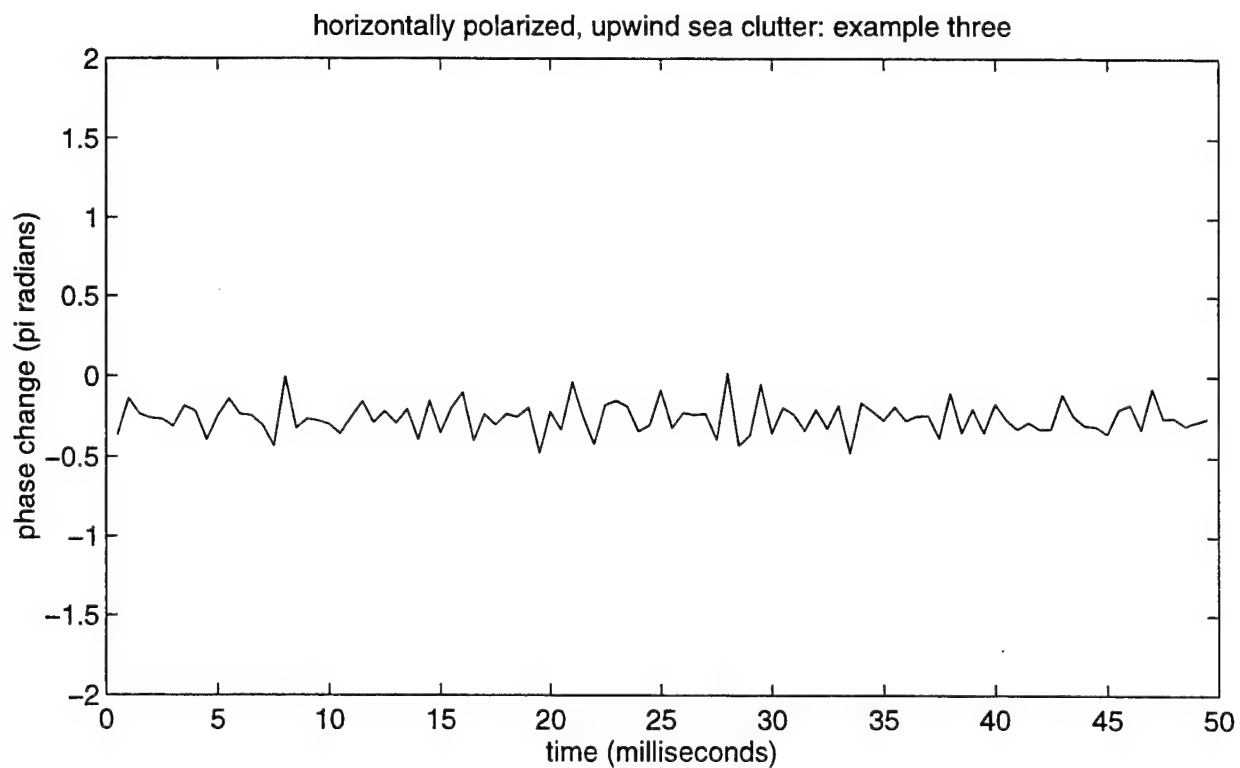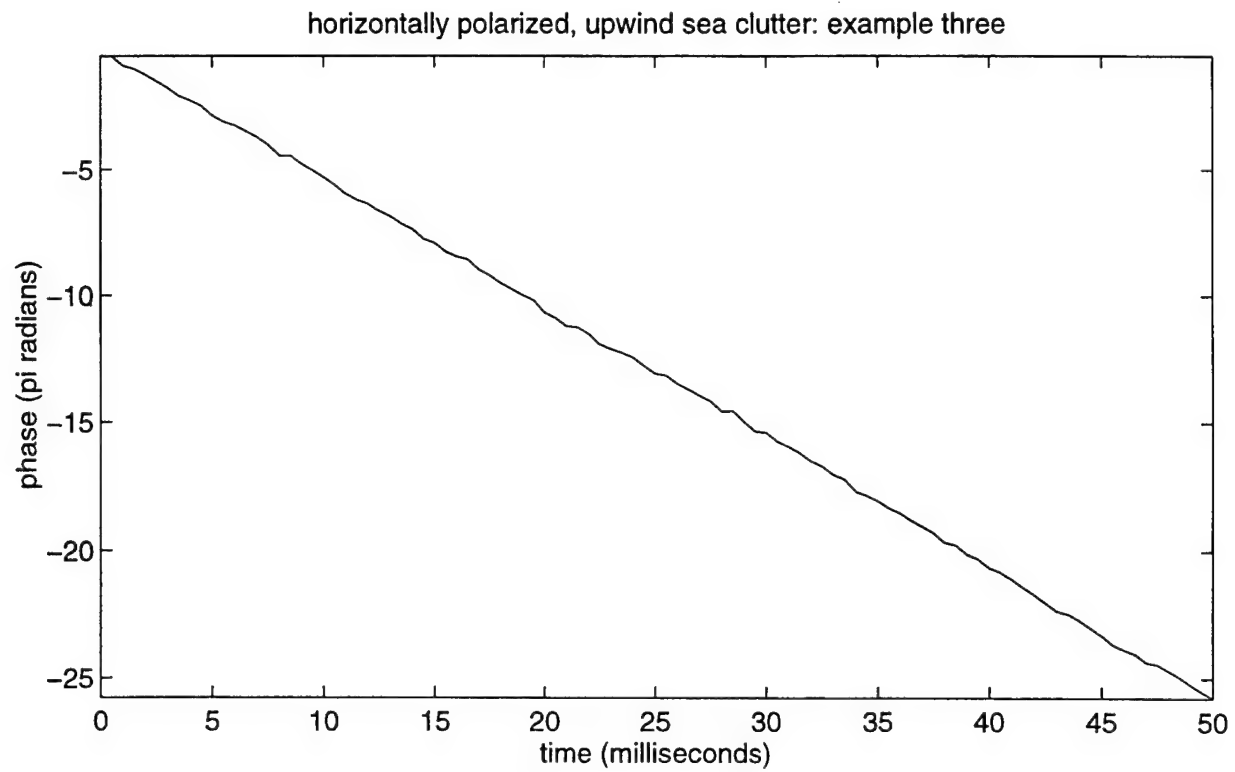
Figure 24: Phase (above), in π radians, and change in phase (below), in π radians, for example three, illustrating HH/UP sea clutter.
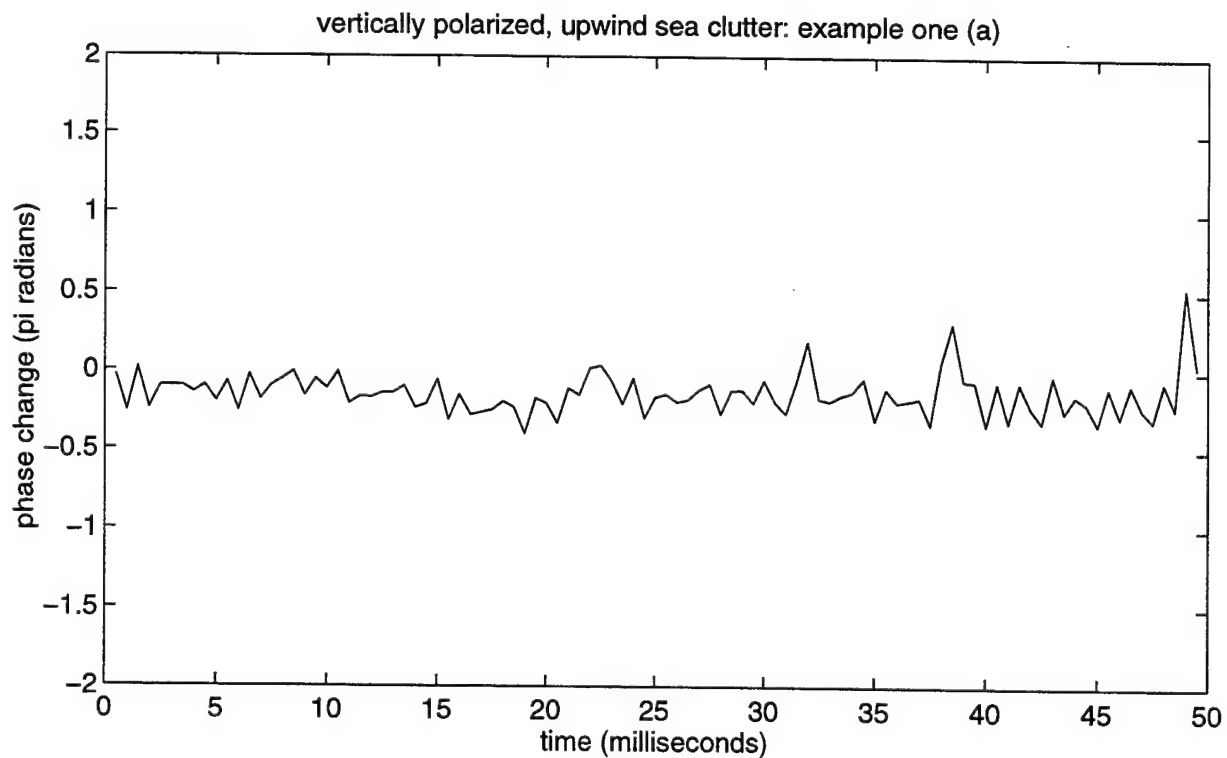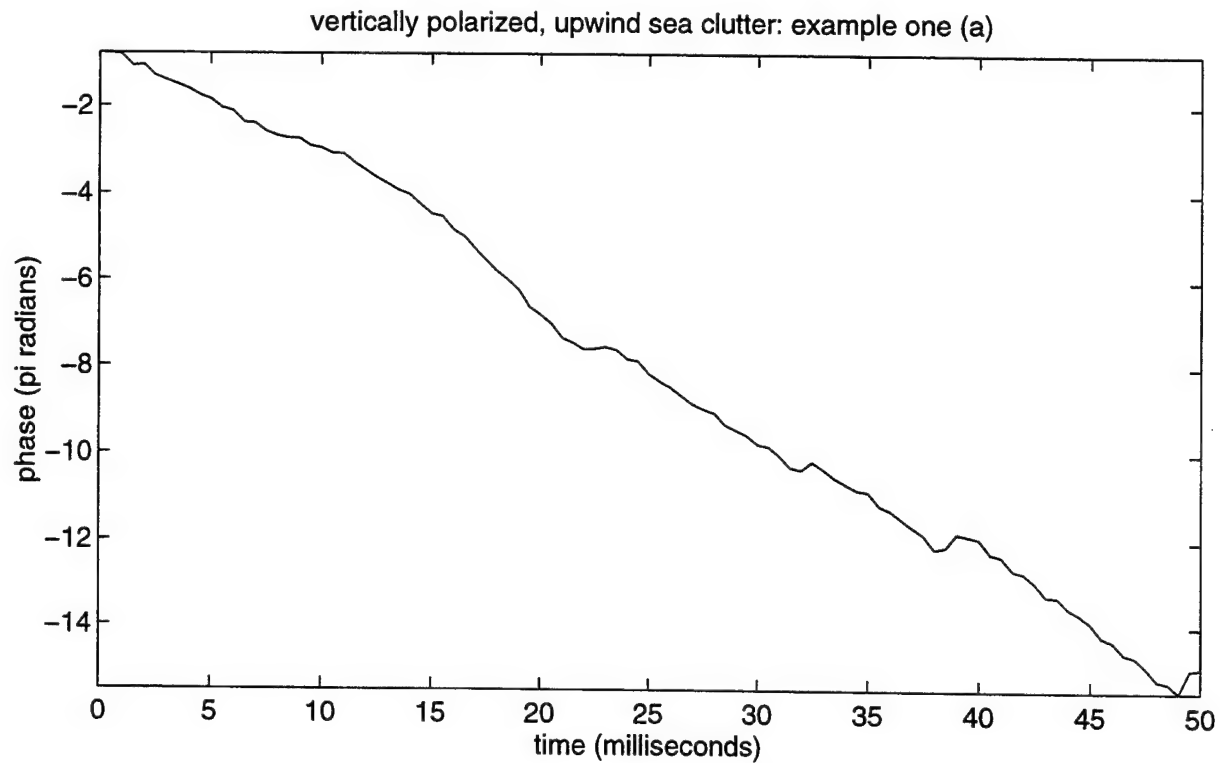
44

Figure 25: Phase (above), in π radians, and change in phase (below), in π radians, for example one (a), illustrating VV/UP sea clutter.

45

associated with incoming waves upon which are superimposed other phenomena, such as forward-breaking or tumbling crests, which increase the overall range rate.

Using the same clutter data that were analyzed in Figures 21, 22, 23, 24, and 25, Figure 26 presents, at the top, the change in RCS and, at the bottom, the zero-mean change in phase of HH/UP example three, while Figure 27 presents, at the top, the change in RCS and, at the bottom, the zero-mean change in phase of VV/UP example one (a). The pulse-to-pulse changes in RCS are relatively large, with a standard deviation of 1.84 dB for HH/UP example three and 2.59 dB for VV/UP example one (a). The zero-mean pulse-to-pulse changes in phase are relatively small, with a standard deviation of 17.47 degrees for HH/UP example three and 24.06 degrees for VV/UP example one (a). As you go from the HH/UP example to the VV/UP example, the percentage increases in standard deviation, for both the change in RCS and the zero-mean change in phase, are almost identical. Noting that the zero-mean changes in phase are relatively small, while the simultaneous changes in RCS are relatively large, leads to the conclusion that one is observing the relative oscillations of a few strong scatterers or, perhaps, the simple addition or subtraction of scattering zones observed in the formation and decay of a whitecap. (See Hansen and Cavaleri [Hans 82].)

7   Discussion of Related Research

Among the other researchers who have recently investigated the differences between HH and VV sea backscatter in the Doppler frequency domain are the following.

1. Lee et al. [Lee 94, Lee 95a, Lee 95b, Lee 96], using an X-band, 9–9.5 GHz, CW coherent scatterometer, with grazing angles only as low as 10 degrees, noted for the UP case that HH PSDs have spectral peaks at higher Doppler frequencies than VV PSDs, but their analyses never went above 300 Hz. They also examined other X-band, 10 GHz data, with grazing angles only as low as 5 and 6 degrees, and C-band, 5.7 GHz data, with grazing angles between 0.3 and 4 degrees, but not for Doppler frequencies above 200 Hz.

2. Rozenberg et al. [Roze 95, Roze 96], using a Ku-band, 14 GHz scatterometer, with grazing angles only as low as 6 degrees, noted an increase in Doppler frequency modulation in the UP case for HH compared to VV, but their analyses never went above 200 Hz.

3. Smith et al. [Smit 96], using an S-band, 3 GHz, Doppler radar with FMCW modulation, with a grazing angle only as low as 8 degrees, noted an increase in Doppler velocity in the UP case for HH compared to VV, but their final Doppler spectra were incoherent averages of 200 individual spectra spaced 1.5 seconds apart.

4. Werle [Werl 95], examining two different sets of X-band, 10 GHz data, with unspecified low grazing angles, extracted the peak intensity Doppler lines from each of many spectra, and plotted the resulting histograms, over a limited Doppler frequency axis of several hundred Hz, to show that HH tends to have higher Doppler frequencies than VV.
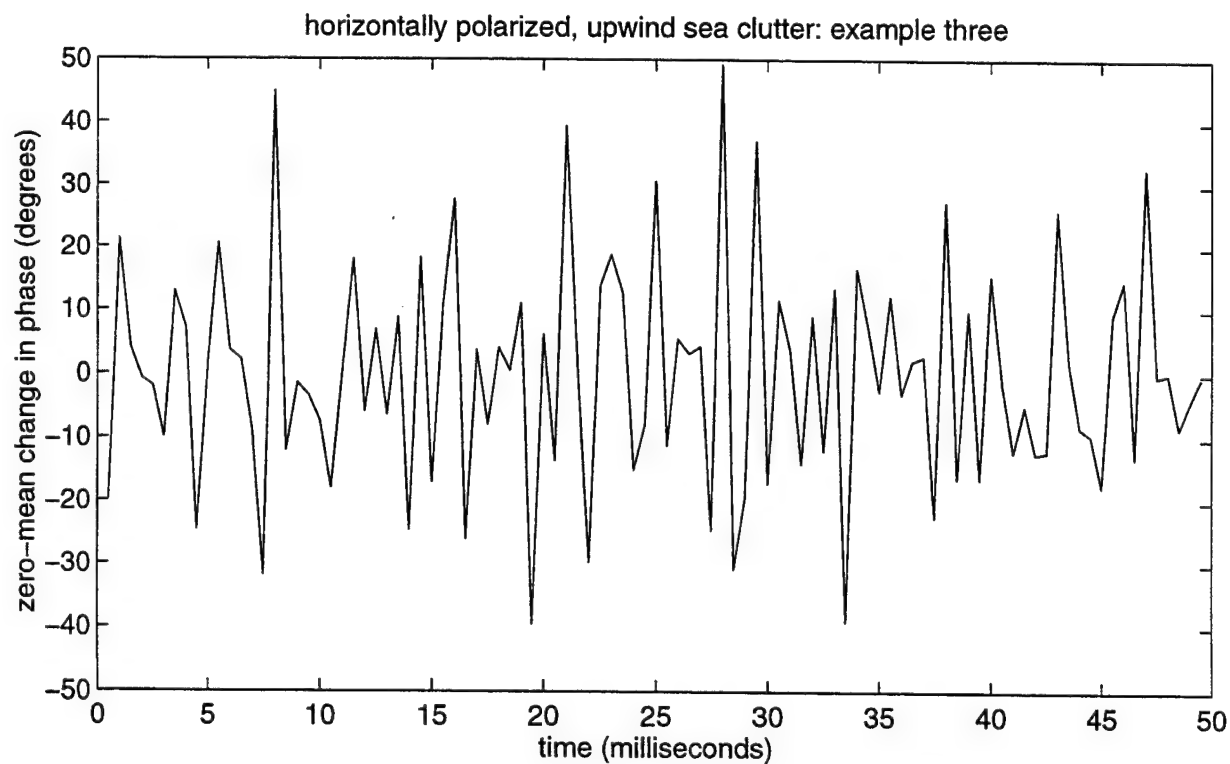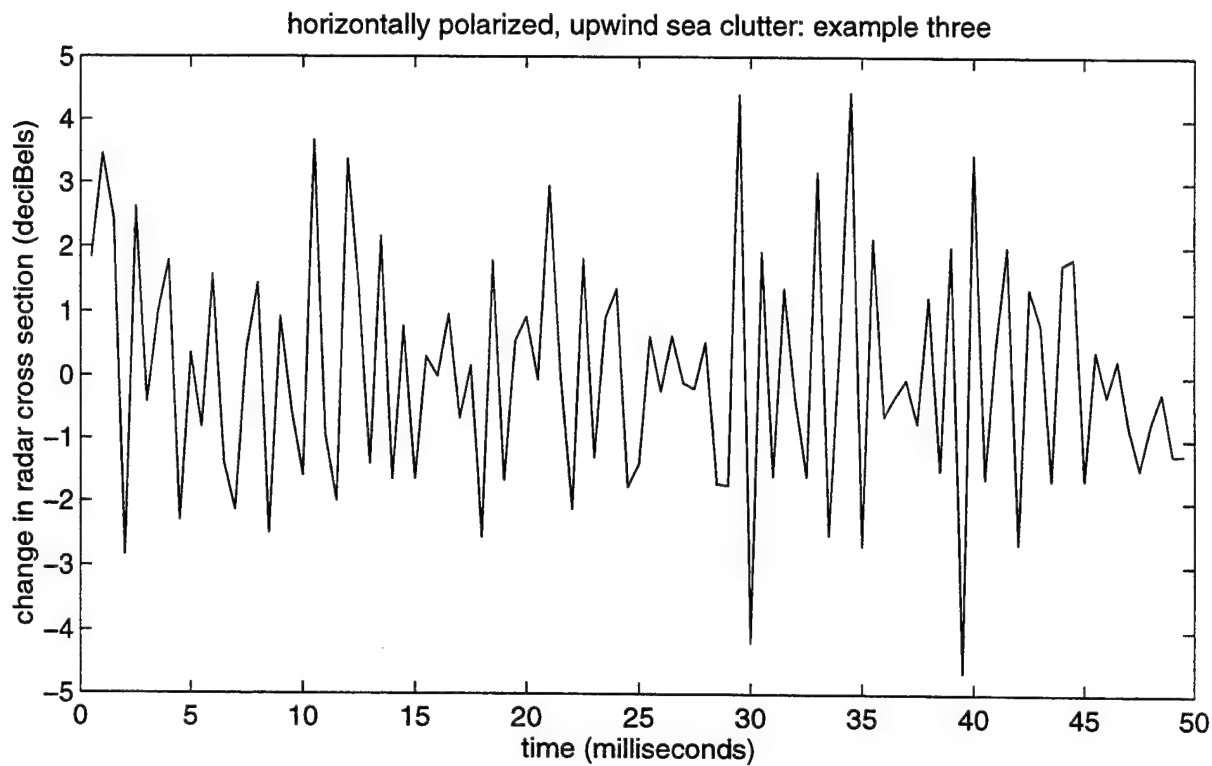
Figure 26: Change in RCS (above), in dB, and zero-mean change in phase (below), in degrees, for example three, illustrating HH/UP sea clutter.
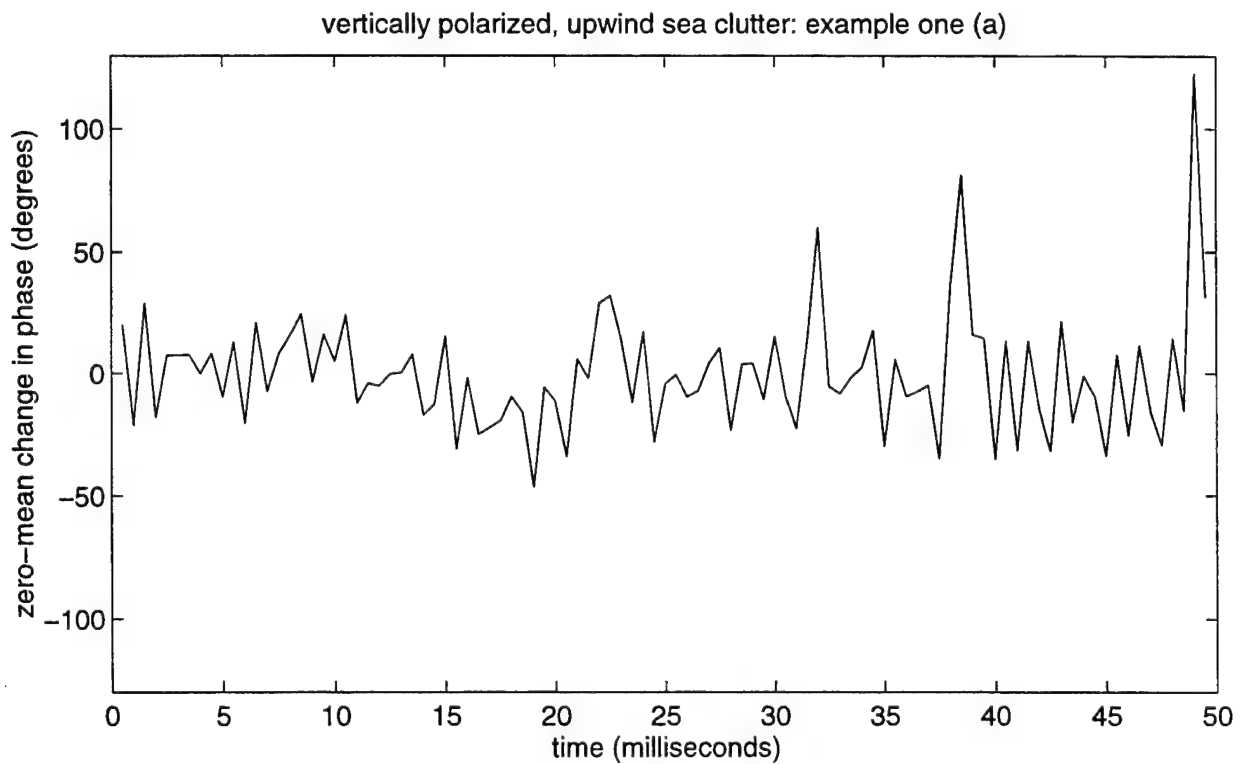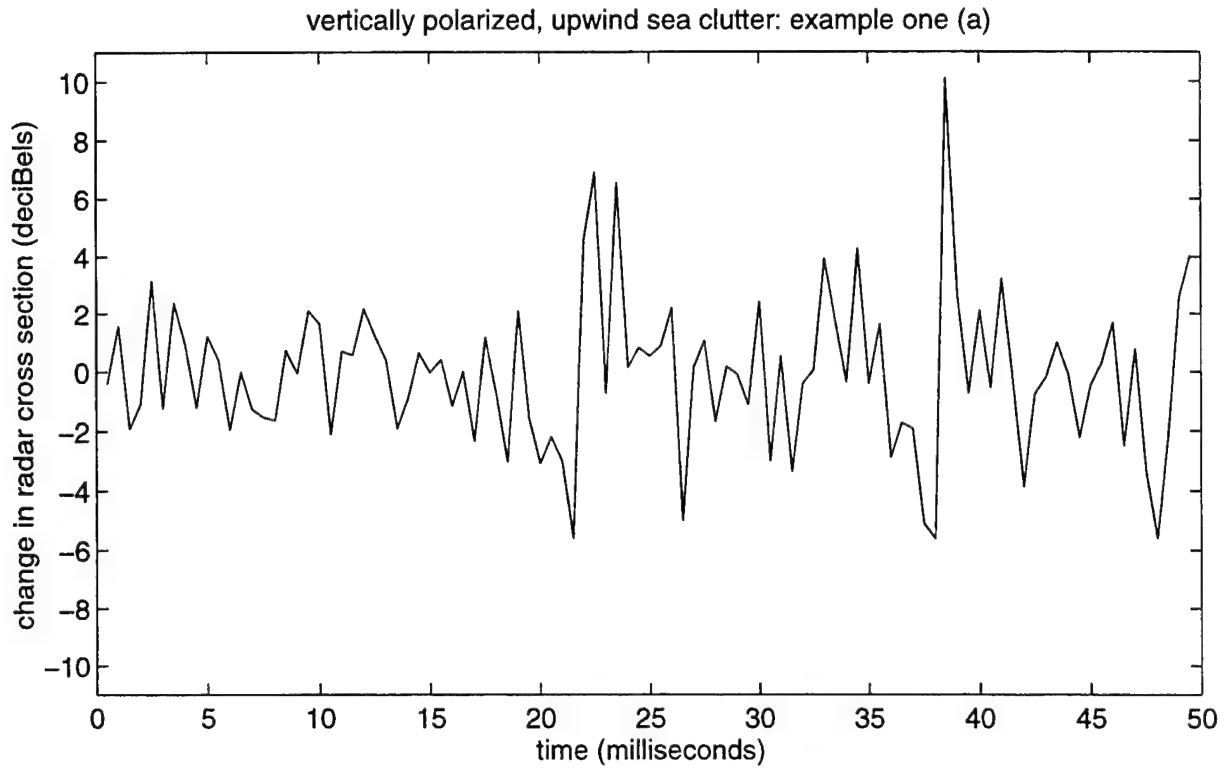
Figure 27: Change in RCS (above), in dB, and zero-mean change in phase (below), in degrees, for example one (a), illustrating VV/UP sea clutter.

48

5. Eckert et al. [Ecke 94], using an X-band, 9.75 GHz, synthetic pulse radar, with a grazing angle only as low as 1 and 2 degrees, noted an increase in the Doppler frequency corresponding to the peak in the PSD for HH compared to VV, but their analyses never went above 300 Hz.

6. Jessup et al [Jess 91a, Jess 91b], using a Ku-band, 14 GHz, CW Doppler scatterometer, with a medium grazing angle of 45 degrees, noted an occasional increase in Doppler frequency modulation for HH compared to VV, but their analyses never went above 500 Hz.

7. Atanassov et al. [Atan 90], using an X-band, 9.6 GHz, coherent CW radar, with a grazing angle only as low as 6 degrees, noted an increase in high frequency components in the PSD for HH compared to VV, but although their analyses did go to 1000 Hz, they chose to do spectral averaging over 31 multiple instantaneous sample spectra obtained from 31 overlapped time series.

8. Chan [Chan 90], using an X-band, 9.2 GHz, 500 Hz PRF radar, with a grazing angle below 5 degrees, noted an upward shift in the Doppler frequency content in the PSD for HH compared to VV, but his analyses never went above 250 Hz.

9. Ward et al. [Ward 90], using an X-band, 9.5–10 GHz radar, with an unspecified grazing angle which might have been as low as 1 degree, noted that the mean Doppler offset of the averaged PSD was higher for HH compared to VV, but their analyses never went above 500 Hz.

10. Hansen and Cavaleri [Hans 82], using an X-band, 8.6 and 9.2 GHz radar, with a grazing angle of 1.4 degrees, noted an increase in the higher Doppler frequency content in the PSD for HH compared to VV, but their analyses never went much above 250 Hz.

The present author believes that the observations presented in this report, either because of the very low grazing angles characteristic of the data, or because of the extended spectral frequency range to which it has been possible to take the analyses, or because of the individualistic, rather than averaged, nature of the events analyzed, or some combination of the above, do represent an addition to the body of knowledge about high range resolution microwave backscatter from the sea at very low grazing angles. It must be emphasized that the observations presented in this report provide an extension of the related research enumerated above, and that the conclusions drawn in this report are fully consistent with, rather than fundamentally different from, what has already been learned about spiky sea clutter at very low grazing angles and high range resolutions.

8   Conclusion

Extensive amounts of microwave sea backscatter data were examined, and numerous examples of sea clutter were found, which, when analyzed, exhibited the behavior found by other researchers to be characteristic of spiky sea clutter at low grazing angles and high range resolutions. In fact, the very criterion by which the clutter data in these examples

were carefully selected is that the data, when analyzed, exhibit this behavior which is widely accepted as defining the phenomena known as sea spikes. The specific subset of examples of spiky sea clutter presented in this report are typical of the larger set. Some of the conclusions that can be drawn from these analyses of spiky sea clutter at low grazing angles and high range resolutions are as follows.

1. Large-scale wave phenomena, traveling at speeds roughly on the order of the predicted phase speed, and smaller-scale wave phenomena, traveling at speeds roughly on the order of the predicted group speed, were observed in both vertical and horizontal polarizations with an upwind transmit geometry.

2. Sea clutter at low grazing angles and high range resolutions is sharper, spikier, and more intermittent in horizontal polarization than in vertical polarization.

3. Spiky behavior of microwave sea backscatter at low grazing angles and high range resolutions is more readily observed when the polarization of the radar is horizontal rather than vertical, and when the transmit geometry of the radar is upwind rather than crosswind.

4. Statistical comparisons of spatially and temporally extended spiking events indicate that these events are not to be considered essentially just the same event, differing only in some simple way, such as in average radar cross section, but are distinctly different events, differing between themselves in some complex manner. Individual spiking events are not Rayleigh-distributed, and in the critical spiking range at the tops of their amplitude distributions, individual spiking events exhibit subtle departures from being Weibull-distributed, as well as subtle differences between themselves.

5. During the periods of strong radar returns associated with spiky sea clutter at low grazing angles and high range resolutions, the power spectrum exhibits a characteristic significant high frequency content. The high frequency spectral components are more significant, in the senses of being higher in frequency and larger in amplitude, for horizontal polarization than vertical polarization. There appears to be a correlation between the overall magnitude of a spatially and temporally extended spiking event, and how high in frequency one will find the significant high frequency spectral components that are present in specific examples of spiky sea clutter excerpted from the event itself.

6. For typical spiky sea clutter at low grazing angles and high range resolutions, in both vertical and horizontal polarizations, the zero-mean changes in phase are relatively small, while the simultaneous changes in radar cross section are relatively large.

9 Acknowledgements

many insights about radar, in general, and sea clutter, in particular, that they have shared with me. I would also like to thank Dennis Baden for successfully getting the data to me in the first place.

References

[Atan 90]   V. B. Atanassov, M. G. Balan, S. J. Haimov, G. P. Kulemin, M. A. Michalev, L. Hr. Mladenov, Yu. A. Pedenko, V. B. Razskazovsky, A. K. Savchenko, V. L. Vasilev, "Experimental study on nonstationary X- and Q-band radar backscattering from the sea surface," *IEE Proceedings*, vol. 137, part F, no. 2, pp. 118–124, April 1990.

[Chan 90]   H. C. Chan, "Radar sea-clutter at low grazing angles," *IEE Proceedings*, vol. 137, part F, no. 2, pp. 102–112, April 1990.

[Ecke 94]   E. G. Eckert, C. L. Rino, A. Siegel, T. Webster, A. R. Ochadlick, J. P. Davis, W. C. Everett, J. J. Kraus, and M. B. Rankin, "Ocean Microwave Backscatter from the LOGAN Experiment," *Proceedings of the 1994 International Geoscience and Remote Sensing Symposium*, pp. 815–817, 1994.

[Fras 96]   S. J. Frasier and R. E. McIntosh, "Observed wavenumber-frequency properties of microwave backscatter from the ocean surface at near-grazing angles," *Journal of Geophysical Research*, vol. 101, no. C8, pp. 18391–18407, August 15, 1996.

[Hans 82]   J. P. Hansen and V. F. Cavaleri, "High-Resolution Radar Sea Scatter, Experimental Observations and Discriminants," *Naval Research Laboratory Report 8557*, March 1982.

[Jess 91a]   A. T. Jessup, W. K. Melville, and W. C. Keller, "Breaking Waves Affecting Microwave Backscatter — 1. Detection and Verification," *Journal of Geophysical Research*, vol. 96, no. C11, pp. 20547–20559, November 15, 1991.

[Jess 91b]   A. T. Jessup, W. K. Melville, and W. C. Keller, "Breaking Waves Affecting Microwave Backscatter — 2. Dependence on Wind and Wave Conditions," *Journal of Geophysical Research*, vol. 96, no. C11, pp. 20561–20569, November 15, 1991.

[Kerr 97]   D. W. Kerr, personal communication, July 1997.

[Lee 94]   P. H. Y. Lee, J. D. Barter, C. L. Hindman, B. M. Lake, and H. Rungaldier, "Angle and Polarization Dependent Microwave Backscatter from Ocean Waves," *Proceedings of the 1994 International Geoscience and Remote Sensing Symposium*, pp. 1272–1274, 1994.

[Lee 95a]   P. H. Y. Lee, J. D. Barter, K. L. Beach, C. L. Hindman, B. M. Lake, H. Rungaldier, J. C. Shelton, A. B. Williams, R. Yee, and H. C. Yuen, "X-band microwave backscattering from ocean waves," *Journal of Geophysical Research*, vol. 100, no. C2, pp. 2591–2611, February 15, 1995.

[Lee 95b]   P. H. Y. Lee, J. D. Barter, K. L. Beach, E. Caponi, C. L. Hindman, B. M. Lake, H. Rungaldier, and J. C. Shelton, "Power spectral lineshapes of microwave radiation backscattered from sea surfaces at small grazing angles," *IEE Proceedings — Radar, Sonar, Navigation*, vol. 142, no. 5, pp. 252–258, October 1995.

[Lee 96]   P. H. Y. Lee, J. D. Barter, E. Caponi, M. Caponi, C. L. Hindman, B. M. Lake, and H. Rungaldier, "Wind-Speed Dependence of Small-Grazing-Angle Microwave Backscatter from Sea Surfaces," *IEEE Transactions on Antennas and Propagation*, vol. 44, no. 3, pp. 333–340, March 1996.

[Mart 97]   L. U. Martin, personal communication, August 1997.

[Ocha 94]   A. Ochadlick, Jr., J. Davis, W. Everett, J. Kraus, M. Rankin, A. Siegel, T. Webster, J. Morrison, J. Lyden, C. Rino, and E. Mebus, "Results from the 1993 LOGAN (Low Grazing Angle) Radar Experiment," *Proceedings of the 1994 International Geoscience and Remote Sensing Symposium*, pp. 1266–1268, 1994.

[Olin 82]   I. D. Olin, "Amplitude and Temporal Statistics of Sea Spike Clutter," *Radar-82*, IEE Conference Publication Number 216, pp. 198–202, October 1982.

[Olin 84]   I. D. Olin, "Characterization of Spiky Sea Clutter for Target Detection," *Proceedings of the 1984 IEEE National Radar Conference*, pp. 27–31, August 1984.

[Posn 93]   F. L. Posner, "Texture and Speckle in High Resolution Synthetic Aperture Radar Clutter," *IEEE Transactions on Geoscience and Remote Sensing*, vol. 31, no. 1, pp. 192–203, January 1993.

[Posn 98a]   F. L. Posner, "Spiky Sea Clutter at Low Grazing Angles and High Range Resolutions," *Proceedings of the 1998 IEEE Radar Conference*, pp. 405–410, May 1998.

[Posn 98b]   F. L. Posner, "Spiky Sea Clutter at High Range Resolutions and Very Low Grazing Angles," submitted to the *IEEE Transactions on Geoscience and Remote Sensing*.

[Roze 95]   A. D. Rozenberg, D. C. Quigley, and W. K. Melville, "Laboratory Study of Polarized Scattering by Surface Waves at Grazing Incidence: Part 1 — Wind Waves," *IEEE Transactions on Geoscience and Remote Sensing*, vol. 33, no. 4, pp. 1037–1046, July 1995.

[Roze 96]   A. D. Rozenberg, D. C. Quigley, and W. K. Melville, "Laboratory Study of Polarized Microwave Scattering by Surface Waves at Grazing Incidence: The Influence of Long Waves," *IEEE Transactions on Geoscience and Remote Sensing*, vol. 34, no. 6, pp. 1331–1342, November 1996.

[Sieg 94]   A. Siegal, A. Ochadlick, Jr., J. Davis, W. Everett, J. Kraus, M. Rankin, and J. Lyden, "Spatial and Temporal Correlation of LOGAN-1 High-Resolution Radar Sea Clutter Data," *Proceedings of the 1994 International Geoscience and Remote Sensing Symposium*, pp. 818–821, 1994.

[Smit 96]   M. J. Smith, E. M. Poulter, and J. A. McGregor, "Doppler radar measurements of wave groups and breaking waves," *Journal of Geophysical Research*, vol. 101, no. C6, pp. 14269–14282, June 15, 1996.

[Ward 90]   K. D. Ward, C. J. Baker, and S. Watts, "Maritime surveillance radar — Part 1: Radar scattering from the ocean surface," *IEE Proceedings*, vol. 137, part F, no. 2, pp. 51–62, April 1990.

[Werl 95]   B. O. Werle, "Sea Backscatter, Spikes and Wave Group Observations at Low Grazing Angles," *Proceedings of the 1995 IEEE International Radar Conference*, pp. 187–195, 1995.